# European Semiconductor Laser Workshop

## September 17-18, 2021

# Programme and Abstracts

## Sponsors

# Conference Guidance

## ESLW2021 Programme and overview

This is the first time we have run ESLW online and we are using a few platforms to provide an interactive conference. We have provided some guidance on each of these below which you can refer to throughout the conference and we will also be on hand to provide support: eslw2021@telecom-paris.fr

## Zoom

ESLW2021 will be run as Zoom meeting to allow an interactive conference. We ask that you keep your microphones muted during all talks. Please save questions for the designated Q&A sections. When asking questions, please do this in the chat or by using the "Raise hand" function. If you're not able to ask a question following a talk, there will be an opportunity to meet with speakers and other delegates during break times and at the end of each day in the ESLW2021 Spatial space (see below).

## Spatial

All the breaktimes will take place in the ESLW2021 Spatial space:

https://spatial.chat/s/eslw2021

The space allows delegates to speak and see each other when stood next to each other in the virtual space and there are designated areas for the break times. You will find full guidance on this at the end of this programme and a facilitator will be on hand in the Spatial virtual foyer area to support you.

## Recording on YouTube

Unless delegates have requested that a session is not recorded, all sessions will be recorded and posted on our unlisted ESLW2021 YouTube playlist at the end of each session. The videos will remain accessible for two months from the last day of the conference and will then be deleted.

# Welcome Message

Welcome delegates!

I am very much happy to welcome you at the European Semiconductor Laser Workshop (ESLW). Following a long tradition established in 1978, our ESLW conference is organized in conjunction with the European Conference on Optical Communication. This is the second online ESLW conference and we made further efforts to replicate as much of a traditional conference as possible. To do so, although we have to go through live presentations, all delegates will be able to interact during breaks in the ESLW Spatial space.

The 2021 edition covers new research topics and state-of-the-art developments in the area of semiconductor lasers, nonlinear dynamics, ultrafast laser dynamics, and related photonic devices including quantum dot and dash semiconductor materials, vertical-cavity surface-emitting devices, mode-locking, frequency combs, nanolasers, and quantum cascade devices. Today, the rich physics behind the field of semiconductor lasers is of growing interests for plethora of applications including but not limited to optical communications, defense and security, optical computing, optics-based information security, and optical storage. The conference takes you through the trendiest topics of this exciting research field.

We start on Friday morning with our keynote speaker Professor Ursula Keller from ETH Zurich, Switzerland. She will give us an exceptional talk on "Do photons show gender bias?". During the workshop, we also welcome several prestigious invited speakers. I want to acknowledge them for their participation: Professor Mikhail Belkin (TU Munich, Germany), Dr. Stefan Bittner (CentraleSupelec, France), Professor David Burghoff (University of Notre Dame, United States), Dr. Kirsten E. Moselund (IBM Research Europe, Switzerland), Dr. Jennifer Hastie (University of Strathclyde, Scotland), and Dr. Alfredo de Rossi (Thales Research & Technology, France).

On Friday morning we begin with a session focused on high power semiconductor laser. This is followed in the afternoon by a session on vertical cavity surface-emitting devices and their applications. We finish Friday with a session where delegates can learn about frequency combs and semiconductor laser applications. On Saturday morning we begin with a session on nonlinear dynamics of semiconductor lasers, followed by a session on innovative light-emitting structures. In the afternoon, we finish the workshop by a session on mid infrared quantum devices. We conclude the conference with a closing session where we give the award for the best student paper.

Finally, I want to deeply thank all people involved in the scientific and organizing committees. I also want to acknowledge the support from Télécom Paris and the Institut Polytechnique de Paris. Last but not the least, special thanks to MDPI Applied Physics for sponsoring the best student paper award.

I wish you all a very nice ESLW conference!
Prof. Frédéric Grillot, Télécom Paris, France.

# Program

*Attention: The time schedule corresponds to UTC+02:00 (CEST).*

## Friday, September 17, 2021

09:15 -09:30    **Opening session**

**Do photons show gender bias? (Keynote talk)**
09:30 - 10:30    *Prof.Ursula Keller*
*ETH Zürich, Switzerland*

**III-V nanophotonic devices monolithically integrated on silicon (Invited talk)**
10:30 - 11:00    *Dr. Kirsten E. Moselund*
*IBM Research Europe Switzerland*

11:00 - 11:15    **Break (15min)**

**Session I – High Power Semiconductor Lasers**
***Chaired by Dr.Jennifer E. Hastie***

**Impact of vertical structure on thermal lensing and lateral beam quality in high-power broad-area diode lasers**
11:15 - 11:30    *Mohamed Elattar, Juliane Rieprich and Paul Crump*
*Ferdinand-Braun-Institut gGmbH, Leibniz-Institut für Höchstfrequenztechnik, Gustav-Kirchhoff-Straße 4, 12489 Berlin, Germany*

**Cascaded polarization-coupling of high-power broad-area semiconductor lasers**
11:30 - 11:45    *M. Radziunas*
*Weierstrass Institute (WIAS), Mohrenstrasse 39, 10117 Berlin, Germany*

**Changes of high-power laser diode characteristics with stress-induced reduction of the degree of polarization**
11:45 - 12:00    *A. Maina, C. Coriasso\*, S. Codato, R. Paoletti*
*Convergent Photonics – Via Schiaparelli, 12 -10148 Torino (Italy)*

**12:00 - 13:30**    **Lunch Break (1h30)**

**Session II - Vertical Cavity Surface-Emitting Devices & Applications**
***Chaired by Prof. Maria Ana Cataluna***

**Sub-kHz-linewidth visible VECSELs for cold-atom quantum technology (Invited talk)**
13:30 - 14:00    *Dr.Jennifer E. Hastie*
*University of Strathclyde, Scotland*

**Neural network computing with large-area VCSELs**
14:00 - 14:15    *X. Porte[1,\*], A. Skalli[1], N. Haghighi[2], S. Reitzenstein[2], J. A. Lott[2], D. Brunner[1]*

|  |  |
|---|---|
|  | *1) Institut FEMTO-ST, Université Bourgogne Franche-Comté CNRS UMR 6174, Besançon, France*<br>*2) Institut für Festkörperphysik, Technische Universität Berlin, Hardenbergstraße 36, 10623 Berlin, Germany* |
| 14:15 - 14:30 | **Weight Adjustable Photonic Synapse by Non-Linear Gain in a Vertical Cavity Semiconductor Optical Amplifier**<br>*Juan A. Alanis, Joshua Robertson, Matěj Hejda, and Antonio Hurtado*<br>*Institute of Photonics, Dept. of Physics, University of Strathclyde, Glasgow, UK* |
| 14:30 - 14:45 | **Oxide-Confined vs. Buried Tunnel Junction VCSELs**<br>*A. Gullino[*,1], S. Pecora[1], A. Tibaldi[1,2], F. Bertazzi[1,2], M. Goano[1,2], P. Debernardi[2]*<br>*1) Dipartimento di Elettronica e Telecomunicazioni, Politecnico di Torino, Corso Duca degli Abruzzi 24, 10129 Torino, Italy*<br>*2) CNR-IEIIT, Corso Duca degli Abruzzi 24, 10129 Torino, Italy* |
| 14:45 - 15:00 | **1.5 GHz VECSEL-based Laser System for Ultrafast Multicontrast Nonlinear Imaging**<br>*Thibault A.G Bondaz[1,2*], R. Jason Jones[1], Jerome V. Moloney[1] and John G. McInerney[2]*<br>*1) Wyant College of Optical Sciences, University of Arizona, 85721 Tucson, USA*<br>*2) Department of Physics and Tyndall Institute, University College Cork, Cork, Ireland* |
| 15:00 - 15:15 | **Break (15min)** |
| | <span style="color:red">**Session III - Frequency Combs & Semiconductor Laser Applications**</span><br>*Chaired by Prof. Mariangela Gioannini* |
| 15:15 - 15:45 | **Frequency-modulated combs in quantum cascade lasers: origins and opportunities (Invited talk)**<br>*Prof.David Burghoff*<br>*University of Notre Dame, USA* |
| 15:45 - 16:00 | **Measuring the Linewidth Enhancement Factor during Frequency Comb Operation**<br>*Nikola Opačak[1,*], Florian Pilat[1], Dmitry Kazakov[1,2], Sandro Dal Cin[1], Georg Ramer[3], Bernhard Lendl[3], Federico Capasso[2], Gottfried Strasser[1] and Benedikt Schwarz[1,2]*<br>*1) Institute of Solid State Electronics, TU Wien, Gusshausstrasse 25-25a, 1040 Vienna, Austria*<br>*2) John A. Paulson School of Engineering and Applied Sciences, Harvard University, Cambridge, Massachusetts*<br>*3) Institute of Chemical Technologies and Analytics, TU Wien, Getreidemarkt 9/164, A 1060 Vienna, Austria* |
| 16:00 - 16:15 | **Gain-switched Optical Frequency Combs with comb spacing down to 5 MHz** |

*C. Quevedo-Galán\*, P. López-Querol, A. Pérez-Serrano, J.M.G. Tijero and I. Esquivias*
*CEMDATIC - E.T.S.I. Telecomunicación, Universidad Politécnica de Madrid, 28040 Madrid, Spain*

| | |
|---|---|
| 16:15 - 16:30 | **Investigation of the wavelength tuning of an integrated laser system on InP for Optical Coherence Tomography**<br>*J. Hazan[1,\*] T. Couka[2], R. Pajkovic[1], K.A. Williams[1], E.A.J.M. Bente[1]*<br>*1) Photonic Integration Group, Department of Electrical Engineering, Eindhoven University of Technology, The Netherlands*<br>*2) Ecole Nationale Supérieure d'Ingénieurs de Caen, FRANCE* |
| 16:30 - 16:45 | **A Technique for Extracting the Carrier Lifetime of a Reversely Biased Semiconductor Optical Amplifier with Two Free Running Lasers**<br>*L. Nielsen[1,\*], M. Heck[1,2]*<br>*1) Department of Electrical and Computer Engineering, Aarhus University*<br>*2) Department of Electrical Engineering, Eindhoven University of Technology* |
| 16:45 - 17:00 | **Free-space video broadcasting with a packaged, air-cooled, mid-infrared quantum cascade laser**<br>*Pierre Didier[1,\*], Olivier Spitz[1], Frédéric Grillot[1,2]*<br>*1) LTCI Télécom Paris, Institut Polytechnique de Paris, 19 place Marguerite Perey, Palaiseau, 91120, France*<br>*2) Center for High Technology Materials, University of New-Mexico, Albuquerque, NM 87106, USA* |

# Saturday, September 18, 2021

| | |
|---|---|
| | <span style="color:red">**Session IV - Nonlinear Dynamics**</span><br>*Chaired by Dr.Alfredo De Rossi* |
| 09:00 - 09:30 | **Stable-cavity broad-area semiconductor laser for ultrafast parallel random bit generation (Invited talk)**<br>*Dr.Stefan Bittner*<br>*CentraleSupélec, France* |
| 09:30 - 09:45 | **Numerical training of a convolutional neural network for self-mixing interferometry displacement sensing**<br>*Robin Matha[1,2], François Gustave[1] and Stéphane Barland[2]*<br>*1) DOTA, ONERA, Université Paris-Saclay, F-91123, Palaiseau, France*<br>*2) Université Côte d'Azur – CNRS, Institut de Physique de Nice, 1361 route des Lucioles, F-06560, Valbonne, France* |
| 09:45 - 10:00 | **Dynamics and CW stability of a III-V/Si hybrid laser with a frequency selective mirror**<br>*C. Rimoldi[1,\*], L. L. Columbo[1], J. Bovington[2], S. R. García[3], M. Gioannini[1]* |

<table>
<tr><td></td><td>

*1) Department of Electronics and Telecommunications, Politecnico di Torino, Italy*

*2) CISCO Systems, San José, CA, USA*

*3) CISCO Systems, Nuremberg, Germany*

</td></tr>
</table>

| | |
|---|---|
| | **Effect of the filtered feedback on the memory capacity in a photonic reservoir computer** |
| | *G. O. Danilenko[1], A. V. Kovalev[1,*], A. Locquet[2,3], D. Rontani[4], and E. A. Viktorov[1]* |
| | *1) ITMO University, 199034 Saint Petersburg, Russia* |
| 10:00 - 10:15 | *2) Georgia Tech-CNRS IRL 2958, Georgia Tech Lorraine, F-57070 Metz, France* |
| | *3) School of Electrical and Computer Engineering, Georgia Institute of Technology, Atlanta, Georgia 30332, USA* |
| | *4) Chair in Photonics, LMOPS EA 4423 Laboratory, CentraleSupélec & Université de Lorraine, F-57070 Metz, France* |
| | **Dual-section passively mode-locked quantum-dot laser with continuous-wave optical injection** |
| 10:15 - 10:30 | *A. F. Ribeiro\*, A. F. Forrest, and M. A. Cataluna* |
| | *Institute of Photonics and Quantum Sciences, Heriot-Watt University, Edinburgh EH14 4AS, United Kingdom* |
| | **Bound Pulse States in a Multiple-Quantum-Well Laser Subject to Delayed Optoelectronic Feedback** |
| | *Md Shariful Islam[1, 2, *], A.V. Kovalev[3], E. A. Viktorov[3], A. Locquet[1, 2], and D. S. Citrin[1, 2]* |
| 10:30 - 10:45 | *1) Georgia Tech-CNRS UMI 2958, Georgia Tech Lorraine, 2 Rue Marconi, 57070 Metz, France* |
| | *2) School of Electrical and Computer Engineering, Georgia Institute of Technology, USA* |
| | *3) ITMO University, Birzhevaya Liniya 14, 199034 Saint Petersburg, Russia* |
| 10:45 - 11:00 | **Break (15min)** |
| | **Session V - Innovative Light Emitting Structures & Applications** |
| | ***Chaired by Dr.Stefan Bittner*** |
| | **Nanoscale Photonic Sources of Coherent Light (Invited talk)** |
| 11:00 - 11:30 | *Dr.Alfredo De Rossi* |
| | *Thales Research & Technology, France* |
| | **Narrow-linewidth semiconductor Fano laser** |
| | *Y. Yu[1,2,*], A. Sakanas[1,2], A. R. Zali[1,2], E. Semenova[1,2], K. Yvind[1,2], and J. Mørk[1,2,*]* |
| 11:30 - 11:45 | *1) DTU Fotonik, Technical University of Denmark, Lyngby, Denmark* |
| | *2) NanoPhoton – Center for Nanophotonics, Technical University of Denmark, Lyngby, Denmark* |

| | |
|---|---|
| 11:45 - 12:00 | **InP based quantum dot laser at 1.3 µm**<br>*V. Joshi\*, S. Bauer, V. Sichkovskyi, and J. P. Reithmaier*<br>*Technical Physics, Institute of Nanostructure Technologies and Analytics (INA), CINSaT, University of Kassel, Heinrich-Plett-Str. 40, 34132 Kassel, Germany* |
| 12:00 - 12:15 | **Time-symmetric and symmetry-broken pulse sequences in a spiking micropillar laser with optical delayed feedback**<br>*V. A. Pammi[1], S. Terrien[2], N. G. R. Broderick[2], R. Braive[1], G. Beaudoin[1], I. Sagnes[1], B. Krauskopf[2], S Barbay[1,\*]*<br>*1) Université Paris-Saclay, CNRS, Centre de Nanosciences et de Nanotechnologies, UMR9001, Palaiseau, France*<br>*2) The Dodd-Walls Centre for Photonic and Quantum Technologies, The University of Auckland, New Zealand* |
| 12:15 - 12:30 | （Cancelled）~~Ultra-Short Optical Pulse Generation in a Micro OLED~~<br>~~*Daan Lenstra[1], Alexis Fischer[2,3], Amani Ouirimi[2,3], Alex Chamberlain Chime[2,3,4], Nixson Loganathan[2,3], Mahmoud Chakaroun[2,3]*~~<br>~~*1) Institute of Photonics Integration, Eindhoven University of Technology, P.O. Box 513,*~~<br>~~*5600MB Eindhoven, The Netherlands*~~<br>~~*2) Universite Sorbonne Paris Nord, Laboratoire de Physique des Lasers, UMR CNRS 7538,*~~<br>~~*99 avenue JB Clement, 93430 Villetaneuse-F*~~<br>~~*3) Universite Sorbonne Paris Nord, Centrale de Proximite en Nanotechnologies de Paris*~~<br>~~*Nord, 99 avenue JB Clement, 93430 Villetaneuse-F*~~<br>~~*4) Universite de Dschang, IUT FV de Bandjoun, Cameroon*~~ |
| 12:30 - 12:45 | **Thermal Crosstalk Effects in Monolithically Integrated DBR Lasers**<br>*Jessica César Cuello[1,\*], Alberto Zarzuelo[2], Robinson C. Guzmán[1], Luis G. Guerrero[1], Guillermo Carpintero[1]*<br>*1) Universidad Carlos III de Madrid, Av. de la Universidad 30, 28911 Leganés, Madrid. Spain*<br>*2) SENER Aeroespacial, 28760 Tres Cantos, Madrid, Spain* |
| **12:45 - 14:00** | **Lunch Break (1h15)** |
| | <span style="color:red">**Session VI - Mid-infrared Quantum Devices**</span><br>***Chaired by Prof. David Burghoff*** |
| 14:00 - 14:30 | **Mid-infrared photonic integration on InP (Invited talk)**<br>*Prof.Mikhail Belkin*<br>*Walter Schottky Institute, TU Munich, Germany* |
| 14:30 - 14:45 | **Mid-Infrared saturable absorbers with ultra-low saturation intensities in the 10-kWcm-2 range**<br>*M. Jeannin[1,\*], J.-M. Manceau[1], M. Soubigou[1], S. Pirotta[1], M.* |

Malerba[1], L. Li[2], A. G. Davies[2], E. Linfield[2], G. Biasiol[3], and R. Colombelli[1]

1) Centre de Nanosciences et de Nanotechnologies (C2N), CNRS UMR 9001, Université Paris-Saclay, 91120 Palaiseau, France
2) School of Electronic and Electrical Engineering, University of Leeds, Woodhouse Lane, Leeds LS2 9JT, United Kingdom
3) Laboratorio TASC, CNR-IOM, Area Science Park, S.S. 14 km 163.5, Basovizza, I-34149 Trieste, Italy

|  |  |
|---|---|
| 14:45 - 15:00 | **Optical injection of mid-infrared extreme events in unilaterally coupled quantum cascade lasers**<br><br>*Olivier Spitz[1], Andreas Herdt[2], Wolfgang Elsässer[2], Frédéric Grillot[1,3]*<br>*1) LTCI Télécom Paris, Institut Polytechnique de Paris, 19 place Marguerite Perey, Palaiseau, 91120, France*<br>*2) Technische Universität Darmstadt, Schlossgartenstrasse 7, D-64289 Darmstadt, Germany*<br>*3Center for High Technology Materials, University of New-Mexico, Albuquerque, NM 87106, USA* |
| 15:00 - 15:15 | **Improving the performance of interband cascade lasers: the influence of intersubband transitions in the valence band**<br><br>*H. Knötig[1,\*], R. Weih[2], N. Opacak[1], J. Koeth[2], G. Strasser[1], B. Schwarz[1]*<br>*1) Institute of Solid State Electronics and Center for Micro- and Nanostructures, TU Wien, Vienna, Austria*<br>*2) nanoplus Nanosystems and Technologies GmbH, Gerbrunn. Germany* |
| 15:15 - 15:30 | **Efficient double-side detection in the mid-IR, with a QWIP MIM architecture on a transparent substrate**<br><br>*Mario Malerba[1,\*], Mathieu Jeannin[1], Stefano Pirotta[1], Lianhe Li[2], Alexander Giles Davies[2], Edmund Linfield[2], Adel Bousseksou[1], Jean-Michel Manceau[1] and Raffaele Colombelli[2,\*]*<br>*1) Centre de Nanosciences et de Nanotechnologies (C2N), CNRS UMR 9001, Université Paris-Saclay, 91120 Palaiseau, France*<br>*2) School of Electronic and Electrical Engineering, University of Leeds, Woodhouse Lane, Leeds LS2 9JT, United Kingdom* |
| 15:30 - 15:45 | **InAs-based quantum cascade lasers for spectroscopy of methane**<br><br>*K. Kinjalk[1,\*], D. Andres Diaz-Thomas[1], Z. Loghmari[2], A. Meguekam[1], M. Bahriz[1], R. Teissier[2], and A.N. Baranov[1]*<br>*1) IES, University of Montpellier, CNRS, 34095 Montpellier, France*<br>*2) Mirsense, 91120 Palaiseau, France* |
| **15:45 - 16:00** | <span style="color:red">**Best Student Paper Award**</span> |

# Abstract

## Session I: High Power Semiconductor Lasers

# Impact of vertical structure on thermal lensing and lateral beam quality in high-power broad-area diode lasers

**Mohamed Elattar, Juliane Rieprich and Paul Crump** *(E-Mail: mohamed.elattar@fbh-berlin.de)*
*Ferdinand-Braun-Institut gGmbH, Leibniz-Institut für Höchstfrequenztechnik, Gustav-Kirchhoff-Straße 4, 12489 Berlin, Germany*

**Abstract:** Proper regulation of the lateral thermal profile (lens) in broad-area diode-lasers (BALs) is essential for improved beam quality. New finite-element thermal-simulation-based analysis of measured thermal lenses in BALs is therefore presented. We show how the interaction of the thermal barrier resistance $R_K$ at the semiconductor-to-metal interface with the vertical thermal conductivity profile of the epitaxial layers regulates the thermal lens. As $R_K$ tends to 0, variation in the epitaxy has little impact on thermal lensing. For high (measured) $R_k$, the variation in epitaxy causes 1.4× variation in the lens curvature and comparable degradation in lateral beam quality of the BAL.

## 1. Introduction

In broad-area diode lasers (BALs), lateral beam quality is quantified using the beam parameter product $BPP_{lat}$, calculated as ¼ of the product of the near-field width and far-field angle. With increasing optical power, and the subsequent active-zone temperature increase $\Delta T_{AZ}$ due to non-zero thermal resistance $R_{th}$, $BPP_{lat}$ has been shown to follow an empirical linear trend $BPP_{lat} = BPP_0 + S_{th} \cdot \Delta T_{AZ}$, as first proposed in [1]. The fit factors $BPP_0$ and $S_{th}$ represent a non-thermal ground level and a thermal slope, respectively. Recently in [2], a long series of experimental results has been summarized, exploring a wide range of mechanisms that regulate $BPP_0$ and $S_{th}$, thus directly impacting $BPP_{lat}$. One of the primary mechanisms regulating $S_{th}$ is thermal lensing, where refractive index locally increases with increasing temperature in the device center, thus establishing a strong lateral waveguide which allows the guiding of a large number of higher-order modes with high $BPP_{lat}$ (i.e. low beam quality). It has been experimentally demonstrated that one of the factors regulating the strength of the thermal lens is the epitaxial layer structure used to construct the BALs [3,4]. In this work, we expand on the thermal simulation results presented in [2], based on finite element analysis using ANSYS, aiming to gain a deeper understanding of how the vertical structure impacts the thermal lens, subsequently affecting $BPP_{lat}$.

## 2. Review of experimental studies

In previous studies [3,4], thermal camera imaging of the front facet of a BAL under continuous-wave (CW) operation was used to obtain the lateral thermal profile within the plane of the active zone. As shown in Fig. 1(a), a quadratic fit function $T(x) = B_2 \cdot x^2 + B_1 \cdot x + B_0$ was then applied to the thermal profile within ±60 µm of the center of the stripe, with the quadratic (bowing) term $B_2$ used as a measure of the strength of the thermal lens. These studies compared how $B_2$ and $BPP_{lat}$ develop with increasing $\Delta T_{AZ}$ in BALs with different epitaxial layer structures, namely asymmetric super-large optical cavity (ASLOC) and extreme-double-asymmetric (EDAS) designs [3], with identical dimensions and p-side down mounting. Figure 1(c) demonstrates that although overall thermal resistance is very similar, $S_{th}$ is roughly doubled using EDAS compared to ASLOC, and figure 1(b) shows a similar trend for the variation of $B_2$ with $\Delta T_{AZ}$, which is about 40% higher using EDAS, indicating that the bowing variation rate $m_b = \Delta B_2/\Delta T_{AZ}$ is proportional to $S_{th}$ and can therefore be used to estimate how different design changes would affect $BPP_{lat}$.
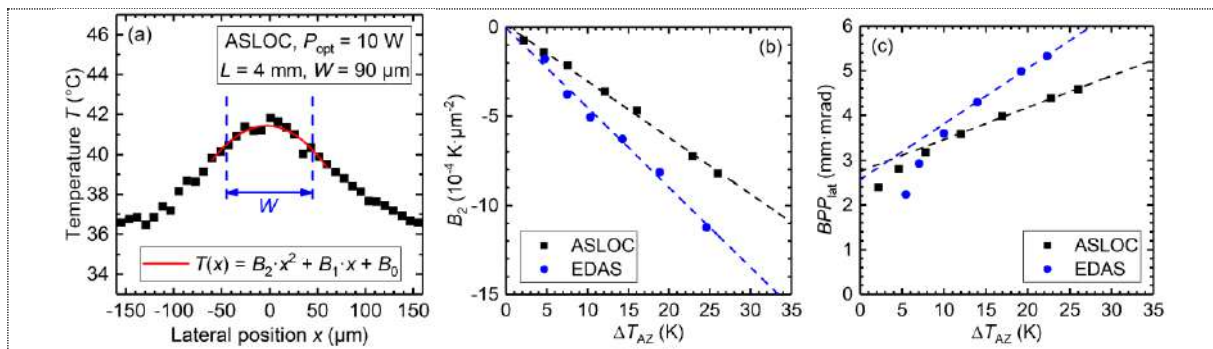


**Figure 1**: (a) Temperature as a function of lateral position, obtained from a thermal camera image of the front facet of an ASLOC BAL, mounted p-side down and operating at 10 W optical power (CW) and 25°C heat sink, with stripe and quadratic fit indicated. (b) Thermal lens bowing (quadratic fit term $B_2$) and (c) measured lateral beam parameter product as functions of change in active-zone temperature $\Delta T_{AZ}$ for two vertical structures ASLOC and EDAS (adapted from [2–4]).

## 3. Simulation model and results

As described in [5], the lateral thermal profile is simulated using ANSYS (finite element analysis tool), which is used to create a 2-D cross-sectional model of the BAL chip with all its epitaxial layers as well as the contact metallization, soldered p-side down onto the submount, with corresponding thermal conductivity values for each material, and a uniform longitudinal thermal profile assumed for simplicity. Heat generation within the chip is calculated at different operating points, and distributed appropriately depending on the amount of absorption, recombination, and Joule heat estimated from each layer. The lateral thermal profiles are vertically averaged over $\pm 5$ µm around the active zone, for better comparability with the thermal camera images with a limited resolution. It has been shown in previous work [5,6] that the p-side semiconductor-metal interface exhibits a large thermal boundary (Kapitza) resistance $R_K \approx 7 \times 10^{-6}$ m$^2 \cdot$K/W (inverse of thermal boundary conductance $h_K \approx 0.14$ MW/(m$^2 \cdot$K)), that increases the total thermal resistance and limits the transfer of heat out of the chip. We find that to reproduce measurement results in simulation, a thermal barrier (TB) layer with high $R_{th}$ (~0.7 K/W) must be introduced between the p-side GaAs contact layer and the contact metallization.

ANSYS simulations are carried out for ASLOC and EDAS BALs at different operating points, with and without the TB layer in each case. Figure 2(a) shows that EDAS only exhibits significantly higher $B_2$ variation (~8.5%) with $\Delta T_{AZ}$ (i.e. higher $m_b$) when the TB layer is included, as needed to agree with the measurement results. Figure 2(b) shows that with increasing $R_K$ at the interface (corresponds to increasing $R_{th}$ of TB layer), the difference in $m_b$ increases proportionally to the thermal resistance difference $\Delta R_{th}$ between the two structures. This indicates that the presence of the thermal barrier amplifies the thermal contrast between structures, thus increasing the impact of vertical design on $R_{th}$, $S_{th}$ and $BPP_{lat}$. Figure 2(c) shows no significant change in $m_b$ in case all the heat is generated inside the active zone, in comparison to the aforementioned realistic distribution of heat sources. This indicates that $\Delta R_{th}$ between ASLOC and EDAS is not due to a different spatial heat distribution, but rather due to the different thermal conductivity profiles of their epitaxial layer structures (c.f. [4]). These simulation results thus demonstrate that by altering the vertical structure and its thermal conductivity profile, the thermal lens could be weakened, thus reducing $S_{th}$ and $BPP_{lat}$.
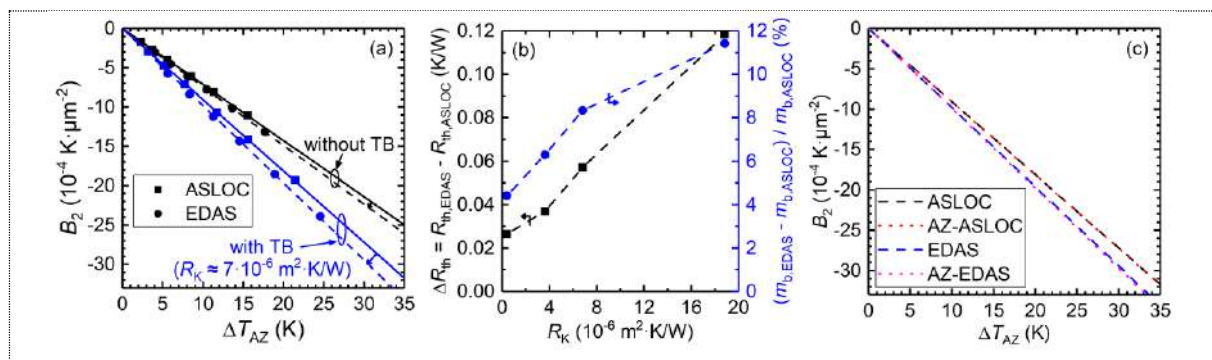


**Figure 2**: ANSYS simulation results for two vertical structures ASLOC and EDAS: (a) Thermal lens bowing (quadratic fit term $B_2$, c.f. Fig. 1) as a function of change in active-zone temperature $\Delta T_{AZ}$, with and without a thermal barrier (TB) layer at the p-side semiconductor-metal interface. (b) Thermal resistance difference $\Delta R_{th}$ and relative difference in bowing variation rate ($m_b$) as functions of thermal boundary (Kapitza) resistance $R_K$ (adapted from [2]). (c) $B_2$ as a function of $\Delta T_{AZ}$, in case of a realistic distribution of heat sources along the vertical structure (ASLOC, EDAS) and in case of a single heat source, where all the heat is generated inside the active zone (AZ-ASLOC, AZ-EDAS).

## 4. Conclusion

We use thermal simulations based on finite element analysis to gain insight into the impact of vertical structure variation on thermal lensing and lateral beam quality in BALs, by comparing the variation of thermal lens bowing with increasing active-zone temperature in different epitaxial layer designs. In agreement with previous studies, we show that to reproduce experimental results in simulation, a thermal barrier layer should be included at the p-side semiconductor-metal interface. We then demonstrate that the difference in thermal lens bowing (correlates with beam quality) between vertical structures is proportional to the difference in their thermal resistance, which is a result of the interaction of the different thermal conductivity profiles of their layer structures with the thermal barrier.

## 5. References and acknowledgement

[1] M. Winterfeldt *et al.*, *J. Appl. Phys.* 116, 063103 (2014).
[2] P. Crump *et al.*, *IEEE J. Sel. Top. Quantum Electron.*, Early Access (2021).
[3] M. Winterfeldt *et al.*, *Proc. SPIE* 9733, 97330O (2016).
[4] P. Crump *et al.*, *Proc. SPIE* 9767, 97671L (2016).
[5] J. Rieprich *et al.*, *J. Appl. Phys.* 123, 125703 (2018).
[6] J. Rieprich *et al.*, *Proc. IEEE High Power Diode Lasers Syst. Conf.* (Coventry, UK), pp. 35-36 (2019).

# Cascaded polarization-coupling of high-power broad-area semiconductor lasers

**M. Radziunas[1]\***

[1]*Weierstrass Institute (WIAS), Mohrenstrasse 39, 10117 Berlin, Germany*
*\*Mindaugas.Radziunas@wias-berlin.de*

**Abstract:** We present a brightness- and power-scalable polarization beam combining scheme for edge-emitting high-power broad-area semiconductor lasers. To achieve the beam combining, we employ Lyot-filtered optical feedback from an external cavity, which forces lasing of the individual diodes on interleaved frequency combs with overlapping envelopes and enables a high optical coupling efficiency. We demonstrate how repeatedly introduced new stages of the external cavity allow efficient coupling of $2^n$ emitters. We simulate the operation of two-four-eight-sixteen coupled emitters, analyze beam coupling efficiency, and discuss possible limiting factors of this coupling scheme.

## 1 Experimental setup and model description

High-power broad-area edge-emitting semiconductor lasers (BALs) are key devices in many modern applications. Using laser diode arrays and suitable beam combining techniques, one can generate kW-beams needed for material processing, for example. Here we analyze a cascadable polarization and spectral beam combining technique that can be employed for coupling BALs with a similar emission wavelength and produces a combined output beam with a well-defined polarization state [1,2].
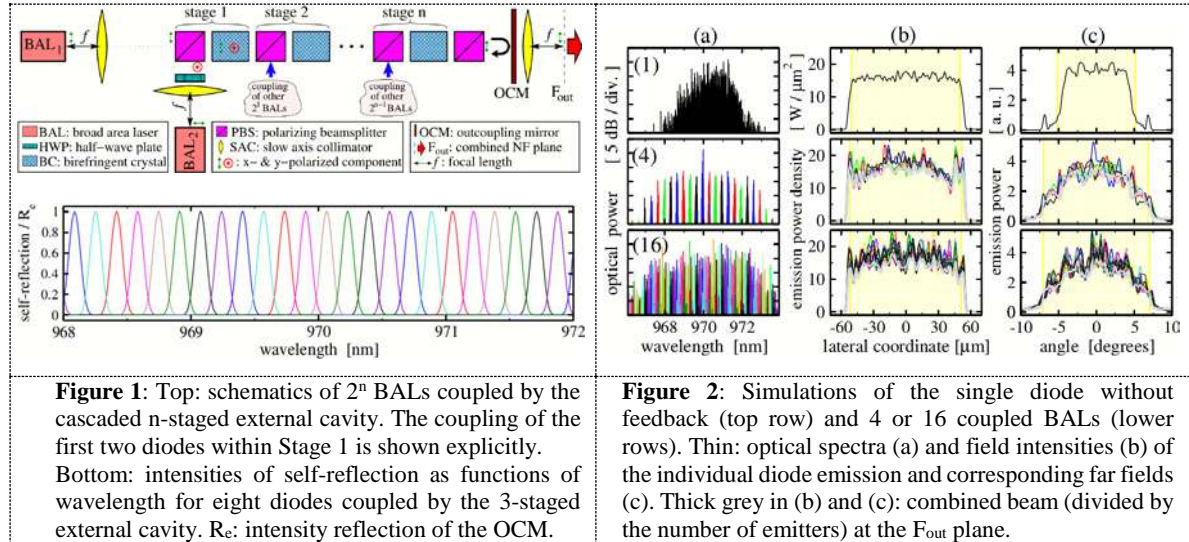
A considered system consists of $2^n$ high-power broad-area semiconductor lasers coupled via a cascaded external cavity (EC). The EC contains different properly located optical elements such as (slow-axis) collimating (SAC) lenses, birefringent crystals (BCs), polarization beam splitters (PBSs), wave-plates (WPs), and a partially reflecting outcoupling mirror (OCM), see the top part of Fig. 1 where a schematic representation of this system is given. For simplicity, this scheme ignores the vertical (fast axis) dimension, assuming ideal fast axis collimation by the adequately located lenses (not shown in the scheme). We also assume that the SAC lenses are perfectly perpendicular to the optical axes of each BAL and are located at the focal distance $f$ from the facets of the lasers. One more SAC lens outside the OCM transforms the $k_x$-space (or angular) representation of the optical fields back to the standard space. The superposition of the emitted fields at the focal distance $f$ behind this outer lens (focal plane $F_{out}$ in Fig. 1) composes a combined near-field of all BALs.

For modeling nonlinear dynamics in BALs, we use a 2(space) + 1(time) dimensional traveling wave (TW) model [3] and our solver BALaser [4]. The model is based on the TW equations for the slowly varying complex amplitudes of the counter-propagating TE-polarized fields within the active zone of each diode, defined in individual longitudinal/lateral ($z/x$) domains. The field equations are extended by couples of linear *polarization* equations allowing to model the frequency-dependence of the material gain dispersion and are nonlinearly coupled to the diffusive rate equations for the excess carrier density. To determine carrier diffusion and laterally distributed bias currents, we simultaneously solve the carrier spreading problem in the BALs' lateral/vertical ($x/y$) cross-sections [5]. Moreover, we alternate ~5 ns transient simulations of the TW model described above with the solution of the static heat-flow models for 3-dimensional time-averaged temperature distributions in the diodes, which determine the heating-induced corrections to the refractive index and some other TW model parameters [6].

The diodes are coupled by the optical feedback induced by the emission of *all* BALs and an individual frequency (wavelength) filtering within the mutual multi-staged EC. A special algorithm for the location of BCs, PBSs, and WPs allows achieving an optimal nicely interleaving self-feedback spectra for all $2^n$ emitters, see, e.g., the lower part of Fig. 1. To construct efficient models of self- and cross-feedback, we used $x$- and $y$-polarized components of the optical field and a paraxial approximation of the wave equations. Moreover, we neglected differences of optical pathlengths and backscattering from all (antireflection coated) elements of the EC, used an idealized thin lens model, and assumed perfect polarization splitting in PBSs. The resulting translation of the emitted fields from the laser facets to the output plane $F_{out}$ behind the OCM or back to the output facets of all lasers are given by local in time and space operators. They are sums of several telescope-type operators, which induce different time delays, phase shifts, and swap of the lateral coordinate $x$. These operators for two coupled diodes are defined in Ref. [2]. In this work, we will discuss an algorithm allowing the construction of the cascaded EC for optimal coupling of $2^n$ (*n<5* in simulations) emitters.

## 2. Results and discussion

We have simulated spatiotemporal dynamics of one or 2/4/8/16 coupled diodes, each operating at 970 nm and emitting about 12 W. All identically driven diodes were 4 mm long, had 100 μm-broad contacts, and 5 μm-wide refractive index trenches nearby. The 4 mm-long BCs (calcite) within the first stage of the EC defines ~1.3 nm wavelength-periodicity of the Lyot filters; see lower panel of Fig. 1 and Fig. 2(a). For more details on the laser and EC parameters, see Ref. [2] and references therein. Next, we assume that all elements within the EC are lossless and perfectly positioned, s.t. all field losses in the EC are only due to imperfect filtering-induced optical mode selection in individual BALs. Part of the emitted modes with the wavelengths deviating from the maximal spectral filtering positions (see lower panel of Fig. 1) generate different polarization components at the end of BCs and are not entirely bypassing the following PBS on their way to the OCM.



**Figure 1**: Top: schematics of $2^n$ BALs coupled by the cascaded n-staged external cavity. The coupling of the first two diodes within Stage 1 is shown explicitly. Bottom: intensities of self-reflection as functions of wavelength for eight diodes coupled by the 3-staged external cavity. $R_e$: intensity reflection of the OCM.

**Figure 2**: Simulations of the single diode without feedback (top row) and 4 or 16 coupled BALs (lower rows). Thin: optical spectra (a) and field intensities (b) of the individual diode emission and corresponding far fields (c). Thick grey in (b) and (c): combined beam (divided by the number of emitters) at the $F_{out}$ plane.

Individual interleaving optical spectra, near- and far-fields, and scaled coupled beams of different laser configurations are shown in Fig. 2. The coupling scheme induces only a slight broadening of the combined beam's spectral, spatial, and angular characteristics, comparing them to those characteristics of the single BAL (upper diagrams in Fig. 2). The combined beam power scales with the number of diodes and can be characterized by the coupling efficiency factor η, which is the ratio of the combined field power behind the OCM and the cumulative power of the emitted fields at the front facets of all $2^n$ diodes. In our simulations, we had η=92.7, 89.34, 88.79, and 86% for 2, 4, 8, and 16 coupled diodes, respectively. The calculated >90% efficiencies for idealized EC are well above those of <80% efficiencies reported for two coupled laser *bars* in the experimental system [2]. Repeated simulations assuming an imperfect EC with 4% intensity loss within each coupling stage have shown an efficiency reduction to 89% and 72% in two- and sixteen-coupled-diode cases, respectively. Thus, one of the biggest challenges when constructing the above-discussed beam combining systems is minimizing the field losses in the EC.

## 3. References

[1]    V. Raab and C. Raab, "Mehrstufige Polarisationskopplung," Zeitschrift Photonik, vol. 5, no. 5, pp. 46-49 (2004).

[2]    C. Bree et al. "Beam-combining scheme of high-power broad-area semiconductor lasers with Lyot-filtered reinjection: modeling, simulations, and experiments," J. Opt. Soc. Am. B, vol. 36, no. 7, pp. 1721-1730 (2019).

[3]    M. Radziunas, "Modeling and simulations of broad-area edge-emitting semiconductor devices," The Int. J. of High Perf. Comp. Appl., vol. 32, pp. 512-522 (2018).

[4]    "BALaser: a software tool for simulation of dynamics in Broad Area semiconductor Lasers," http://www.wias-berlin.de/software/BALaser.

[5]    M. Radziunas et al., "Efficient coupling of the inhomogeneous current spreading model to the dynamic electro-optical solver for broad-area edge-emitting semiconductor devices," Optical and Quantum Electronics, vol. 49, pp. 332 (2017).

[6]    M. Radziunas et al., "Efficient coupling of dynamic electro-optical and heat-transport models for high-power broad-area semiconductor lasers," Optical and Quantum Electronics, vol. 51, pp. 69 (2019).

# Changes of high-power laser diode characteristics with stress-induced reduction of the degree of polarization

**A. Maina, C. Coriasso\*, S. Codato, R. Paoletti**

*Convergent Photonics – Via Schiaparelli, 12 -10148 Torino (Italy)*
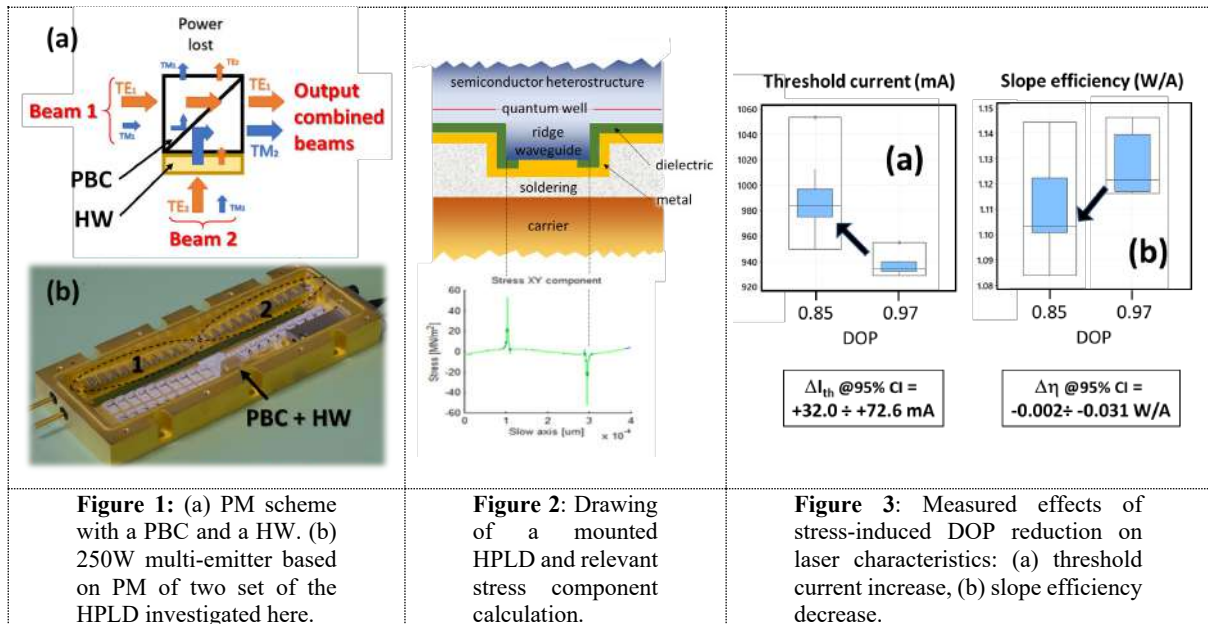*\*claudio.coriasso@convergent-photonics.com*

**Abstract:** A detailed statistical investigation of the threshold current, slope efficiency, far field and near field changes associated with degree-of-polarization reduction of high-power laser diodes is reported. These changes can be a useful metric for laser device optimization aimed to polarization multiplexing applications, well beyond the simple degree-of-polarization measurements.

## 1 Introduction

The Degree of Polarization (DOP) of optical beams emitted by High-Power Lasers Diodes (HPLD) is of utmost importance for multi-emitters exploiting the high brightness Polarization Multiplexing (PM) technique with Polarization Beam Combiners (PBC) and Half Wave (HW) rotators [1], see Fig.1. For mainly TE-polarized laser diodes the DOP is defined as:

$$DOP = \frac{P_{TE}}{P_{TE} + P_{TM}}$$

where $P_{TE}$ and $P_{TM}$ are respectively the TE-polarized and TM-polarized optical power.



| | | |
|---|---|---|
| **Figure 1:** (a) PM scheme with a PBC and a HW. (b) 250W multi-emitter based on PM of two set of the HPLD investigated here. | **Figure 2**: Drawing of a mounted HPLD and relevant stress component calculation. | **Figure 3**: Measured effects of stress-induced DOP reduction on laser characteristics: (a) threshold current increase, (b) slope efficiency decrease. |

The intrinsic DOP of a HPLD can be very high, due to proper active material design by maximizing the TE/TM gain ratio, however, the DOP of mounted HPLD can be significantly reduced by unavoidable mechanical stresses [1, 2]. Beyond the straightforward detrimental effect on the multi-emitter total power, being the DOP a main factor of the overall yield, see Fig. 1(a), the DOP reduction implies less evident but important effects on the overall laser characteristics, which are the focus of this paper. Both the L-I characteristic (threshold current and slope efficiency) and the beam properties (near-, far-field) are indeed significantly affected by DOP reduction and the analysis of the relevant changes could be of general interest for investigation of stress-induced photo-elastic effect on laser diodes.

## 2. Results and discussion

The HPLD addressed in this paper are broad area semiconductor lasers with epitaxial structure similar to that reported in [3]. A compressively strained InGaAs single quantum well active layer, embedded between a

AlGaAs graded-index heterostructure, produces a laser beam at 976nm with a DOP nearly 1. This high intrinsic DOP can be however reduced by mechanical stresses induced by chip fabrication (dielectrics, metals) and chip mounting on carriers, through the photo-elastic effect [2]. Mechanical stresses are enhanced by chip morphology and can be particularly high on waveguide edges, see Fig. 2 in which the result of a COMSOL Multiphysics® simulation for the $xy$ stress component is shown. The mechanical stress translates in an anisotropic refractive index change, through the photo-elastic tensor, which in turn determines the polarization change of the optical field within the active cavity, causing a DOP reduction [4]. This polarization change of the optical field is equivalent to an internal loss producing an increase of the laser threshold current and a decrease of the slope efficiency, see Fig. 3. The laser beam shape is also significantly affected by DOP reduction. Fig 4(a) shows the slow axis far field ($FF_{SA}$) increase by about 13% for similar devices with different DOP (0.85, 0.97). Fig. 4(b) shows the polarization-resolved slow axis near field ($NF_{SA}$) changes for many devices with different DOP, ranging from 0.86 to 0.98. In particular, the TM-polarized $NF_{SA}$, on the left, shows sharp peaks at the waveguide edges when the DOP is high and spreads to the whole waveguide, about 200μm wide, when the DOP is decreasing; while the TE-polarized $NF_{SA}$, on the right, shows an increase of optical filamentation with DOP decreasing. These effects, due to different mode excitation of the multimode lateral waveguide, are highlighted in the top contour plots with the dashed white lines, as a guide for the eye. The bottom images refer to single $NF_{SA}$ acquired for high DOP (H) and low DOP (L) devices and clarify the $NF_{SA}$. shape discussed above. The TM-polarized $NF_{SA}$ represents a map of the mechanical stress on the device and can be very useful in the development of high-DOP HPDL, by optimizing chip dielectrics, metals, shape, mounting process and carrier structure. It is worth underlying that, being the mechanical stress a random effect, all the images shown here refer to statistical measurements of ideally equivalent devices and the result significance was demonstrated by using statistical inference tests.
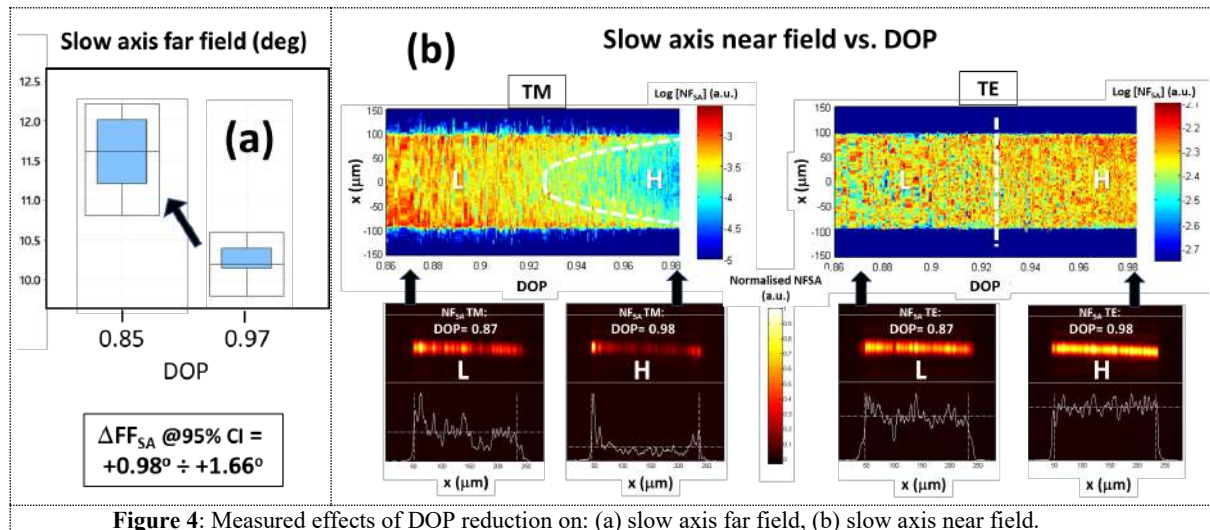


**Figure 4**: Measured effects of DOP reduction on: (a) slow axis far field, (b) slow axis near field.

## 3. Conclusion

DOP reduction effects on electro-optic and laser beam properties of HPLD have been extensively investigated using a statistical approach on many hundreds of devices. Measured results have been validated by statistical inference tests and can be very useful in the high-DOP device optimization, by identifying and reducing residual mechanical stresses.

## 4. References

[1] R. Morohashi et al., "High polarization purity operation of 99% in 9xx-nm broad stripe laser diodes", *Proc. SPIE*, vol. 10514, *High-Power Diode Laser Technology XVI*, 10514B (2018)

[2] M. A. Fritz and D. T. Cassidy, "Photoelastic effect from die bonding of diode lasers", *Appl. Optics*, vol. 43, no. 1, pp. 160-166 (2004)

[3] R. Paoletti et al., "Wavelength-stabilized DBR high-power diode laser", *J. Phys. Photonics*, vol. 2, 014010 (2020)

[4] M. Huang, "Stress Effects on the Performance of Optical Waveguides", *International J. of Solids and Structures*, vol. 40, p. 1615–1632 (2003)

# Abstract

## Session II: Vertical Cavity Surface-Emitting Devices & Applications

# Neural network computing with large-area VCSELs

**X. Porte, [1]\* A. Skalli,[1] N. Haghighi,[2] S. Reitzenstein,[2] J. A. Lott,[2] D. Brunner[1]**

[1] *Institut FEMTO-ST, Université Bourgogne Franche-Comté CNRS UMR 6174, Besançon, France*
[2] *Institut für Festkörperphysik, Technische Universität Berlin, Hardenbergstraße 36, 10623 Berlin, Germany*
*\*Email: javier.porte@femto-st.fr*

**Abstract:** We implement a fully parallel photonic neural network based on the spatially distributed modes of a large-area vertical-cavity surface-emitting laser. All photonic connections are realized in hardware and the system is capable of autonomous operation.

## 1. Introduction

Over the past decade, artificial Neural Networks (NNs) have revolutionized both computing and the demand for high-performance computing hardware. In consequence, a large variety of physical substrates have been proposed to perform neuromorphic computing in recent years [1]. Among them, photonics excels in terms of parallelism and information processing speed. However, until now the majority of large scale and parallel photonic NN demonstrations are neither standalone nor autonomous [2], usually lacking fundamental NN constituents or requiring substantial interaction with a classical electronic computer. Here, we implement a fully parallel photonic reservoir computer based on the spatially distributed modes of an efficient and fast semiconductor laser [3]. Crucially, all neural network connections are realized in hardware, and our laser-based and fully parallel NN comprising ~ 100 neurons produces results without pre- or post-processing.

## 2. Results and discussion

As photonic neuron substrate we use the complex multimode field of an injection locked large-area vertical-cavity surface-emitting laser (LA-VCSEL) of ~20 µm diameter emitting around 920 nm. Figure 1(a) depicts the device we use and its free-running emission profile at a bias current of 1.3 times its lasing threshold. This LA-VCSEL follows a minimalistic design principle that optimizes operation efficiency and bandwidth and were fabricated via standard commercial technology. A detailed description of the device characteristics can be found in [4].
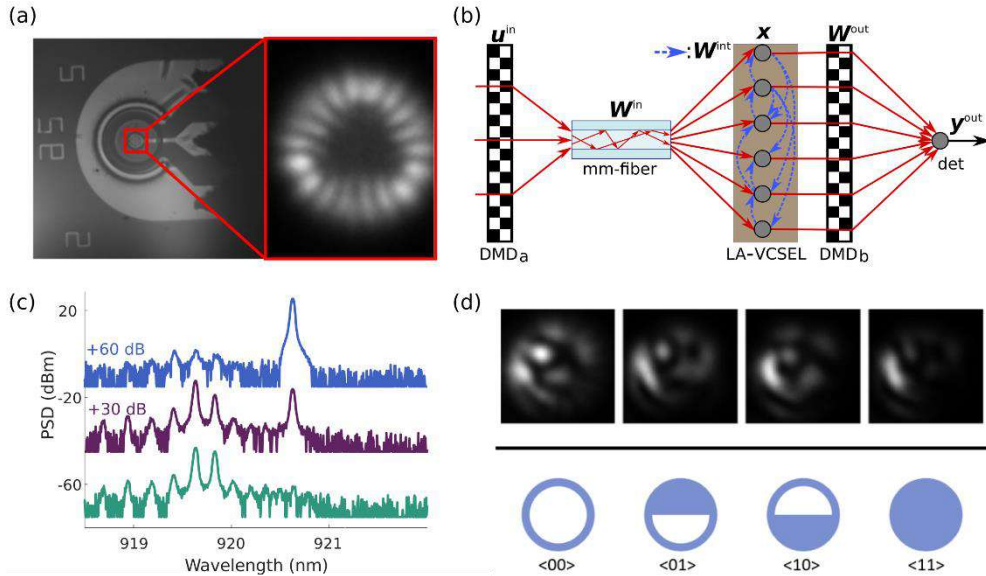


**Fig. 1**. (a) Left: White light image of the LA-VCSEL (~20 µm in diameter); Right: Magnified multimode free lasing emission for a bias current of 1.3 the LA-VCSEL threshold. (b) Schematic illustration of the photonic NN's sections linked to their corresponding physical devices. A digital micromirror device (DMD$_a$) encodes input information $u^{in}$, which is mixed through the complex transfer matrix of a multimode fiber (mm-fiber). The LA-VCSEL acts as recurrent reservoir with state **x**, providing device-inherent internal coupling $W^{int}$. DMD$_b$ implements programmable Boolean readout weights $W^{out}$, and a detector records computational result y$^{out}$. (c) Optical spectra under DC optical injection at increasing power injection ratios. For clarity, offsets of 30dB and 60dB have been respectively added to the middle and top spectra. (d) Perturbed mode profiles (upper panels) under different injection patterns (lower panels) showing the highly nonlinear nature of the LA-VCSEL response.

Our reservoir computing scheme is illustrated in Fig. 1(b). All the photonic NN connections are implemented in hardware: the complex transfer matrix of a multimode (mm) fiber ($W^{in}$) couples the LA-VCSEL to the injected information ($u^{in}$), which is Boolean encoded on a digital micro-mirror device (DMD$_a$). The VCSEL then transforms the injected information non-linearly yielding mode profiles such as those shown in upper panels of

Fig. 1(d). This transformation is comparable to the action of a neural network: similar inputs result in vastly different VCSEL responses, and we can use the laser for pattern recognition. Intra-cavity fields and carrier diffusion intrinsic to LA-VCSELs recurrently couple the photonic neurons ($W^{int}$), and trainable readout weights ($W^{out}$) are encoded on the $DMD_b$ and photo-detected to directly provide the computational result ($y^{out}$). We operate our recurrent photonic NN in its steady state, and its bandwidth is limited by the input DMD's frame rate to around 100 inferences per second.

Although optical injection into multimode LA-VCSELs was extensively studied in the past [5], here we report injection-lock of such device to a complex optical input field for the first time. Figure 1(b) depicts the device's optical response under DC injection of ring-like optical pattern of different thicknesses generated with $DMD_a$. Lower spectrum (in green) corresponds to the free-running laser when biased at $1.28I_{th}$, meanwhile the middle and upper spectra respectively correspond to power injection ratios of $P_{inj}/P_{VCSEL}=0.03$ and $P_{inj}/P_{VCSEL}=0.4$ for identical bias condition and DC injection thicker rings. These latter spectra have been shifted upwards +30 dB and +60 dB for clarity reasons. We observe the gradual depletion of the original emission modes of the LA-VCSEL when the thickness of the DC injection ring is increased. Figure 1(d) shows the resulting photonic ANN state for the example of injecting the four possible configurations of 2-bit symbols. The first binary digit is <00> and corresponds to the DC injection ring. Noteworthy, individual responses significantly differ for each case, which is a prerequisite to differentiate individual digits.

The system learns the best configuration of output mirrors to differentiate between different input patterns. The $DMD_b$ output mirrors each have two possible positions, implementing Boolean weights. We explore different Boolean learning strategies. The first, already described in [6], is a Markovian process where at each epoch a single mirror is flipped, the change is kept if it had a positive impact on the performance metric (NMSE error), otherwise the change is reversed, and another mirror is flipped. Following this learning strategy, we trained the readout weights to perform 2-bit header recognition, 2-bit XOR and 2-bit digital-analog conversion tasks. The error rates achieved by our system for the different tasks are down to: $0.9 \times 10^{-3}$ for the 2-bit header recognition; $2.9 \times 10^{-2}$ for the 2-bit XOR task; and $5.4 \times 10^{-2}$ for the 2-bit digital-to-analog conversion. Moreover, we present a second learning strategy that takes inspiration from the widely used stochastic gradient descent algorithm to enhance the previously introduced Markovian process. In our adaption, at each epoch the number of flipped mirrors ($n_{mirrors}$) depends on the error via a constant learning rate $\alpha$, which is a hyperparameter that we tuned as: $n_{mirrors}=\text{ceil}(\alpha*\text{NMSE})$. The mirrors are still chosen randomly, but such improved strategy allows us to take big steps in the parameter space when the error is high, and progressively reduce the size of these steps as we start converging towards lower errors (note that if $\alpha=0$, $n_{mirrors}$ is always 1). We find a clear dependence between learning rate ($\alpha$), learning speed and NMSE performance. Thanks to this learning strategy, we successfully improve both the speed of convergence during learning as well as the final computational performance.

## 3. Conclusion

We demonstrate a fully analog spatially-extended photonic reservoir computer where each of the system's constituents implemented in hardware in readily available and cost-effective telecommunications components. Furthermore, our present system is scalable in size to much larger networks in excess of 1000 neurons per layer and to bandwidths in excess of 20 GHz, establishing a clear road map for future high-performance photonic hardware for NNs.

## 4. References

[1]     D. Marković, A. Mizrahi, D. Querlioz and J. Grollier. Physics for neuromorphic computing. Nature Reviews Physics, 2(9), 499–510 (2020).

[2]     G. Van Der Sande, D. Brunner and M. C. Soriano. "Advances in photonic reservoir computing," *Nanophotonics* **6**(3), 561-576 (2017).

[3]     X. Porte, A. Skalli, N. Haghighi, S. Reitzenstein, J. A. Lott and D. Brunner, "A complete, parallel and autonomous photonic neural network in a semiconductor multimode laser," J. Phys. Photonics 3, 024017 (2021).

[4]      N. Haghighi, P. Moser and J. A. Lott. "Power, bandwidth, and effciency of single VCSELs and small VCSEL Arrays". *IEEE JSTQE* **25**(6), 1-15 (2019).

[5]     T. Ackemann, S. Barland, M. Giudici *et al*. "Patterns in broad-area microcavities". *Phys. Status Solidi b* **221**, 133–6 (2000).

[6]     L. Andreoli, X. Porte, S. Chrétien *et al*. "Boolean learning under noise-perturbations in hardware neural networks". *Nanophotonics* **9**(13), 4139-4147 (2020).

# Weight Adjustable Photonic Synapse by Non-Linear Gain in a Vertical Cavity Semiconductor Optical Amplifier

**Juan A. Alanis, Joshua Robertson, Matěj Hejda, and Antonio Hurtado**

*Institute of Photonics, Dept. of Physics, University of Strathclyde, Glasgow, UK*
*\*antonio.hurtado@strath.ac.uk*

**Abstract:** Vertical Cavity Semiconductor Optical Amplifiers (VCSOAs) are proposed as high-speed and tunable photonic synaptic elements. By exploiting the nonlinear gain properties of VCSOAs, our system permits full weight tuneability of sub-ns input light pulses. Not only is the VCSOA-based synapse able to adjust the strength of incoming optical pulses, but it can also provide gain (applied weight factors >1). Moreover, we show that this simple approach permits dynamical weight tuning at high-speed (ns rates). This VCSOA-based system therefore offers a hardware friendly, low-energy and high-speed solution for photonic synaptic links, with high potential for use in future neuromorphic photonic hardware.

## 1 Introduction

In recent years, the widespread use of machine learning (ML) approaches has contributed to the development of Artificial Intelligence (AI) to perform complex human-like information processing tasks, such as: learning, computer vision, natural language processing, and complex pattern recognition, etc. Current state-of-the-art neuromorphic (brain-like) computing systems require power-intensive on-chip electronic neural networks, which rely on CMOS technology. In addition, with the size of transistors reaching its physical limit, more complex neural networks come at the expense of a larger device footprint. As an alternative to the CMOS-based paradigm, photonic systems have been raising interest in recent years. In particular, new semiconductor laser systems are appearing under the guise of neuromorphic photonic devices as candidates for neural network nodes. Vertical-cavity surface-emitting lasers (VCSELs) are one of the devices that have shown the ability to reproduce many of the key neuronal characteristics required for artificial neural networks (e.g. interconnectivity, fast sub-ns operation, thresholding).[1] One key aspect of neuromorphic systems is the ability to perform synaptic weighting operations when propagating signals between nodes (Figure 1a). In recent years, photonic synapses have been experimentally demonstrated either photoelectrically, with the use of memristive devices, or in photonic integrated circuits via phase change materials.[2] Very recently, the use of VCSELs for synaptic control via spike timing dependent plasticity (STDP) has been theorized;[3] however to date no experimental demonstration of VCSEL-based photonic synaptic elements has been reported.

In this work we demonstrate the experimental realization of a photonic synaptic element by exploiting the nonlinear gain intrinsic to VCSELs when operated below their lasing threshold as vertical-cavity semiconductor optical amplifiers (VCSOAs).[4] Using these devices, we provide the first experimental demonstration of a VCSOA photonic synaptic system by using the device bias current (below lasing threshold) as a weighting mechanism for short (150ps-long) optical pulses emulating biological neuronal spikes. This system permits full and controllable dynamical strength tuning of the incoming pulses as well as providing signal amplification.

## 2. Experimental setup

An all-fiber-optic system was used to inject light from a tunable laser (TL) into a VCSOA (see Figure 1b). The VCSOA is a commercial 1300nm-VCSEL biased below its lasing threshold current ($I_{th}$ = 2.389mA at 293K). The device had a dominant resonant (parallel polarized) mode at a wavelength $\lambda_{VCSOA} \cong 1306$nm at threshold. The VCSOA was biased with currents $< 95\%\ I_{th}$, to ensure operation below threshold at the non-linear gain region. The TL's light was injected into the parallel resonant peak (Figure 2a, left-most panel) and modulated with a Mach-Zehnder (MZ) modulator to generate 150ps-long input pulses with a repetition rate of 31MHz (generated by Channel 1, CH1, of an Arbitrary Waveform Generator, AWG) and peak amplitude of 44.5$\mu$W (Figure 2a-c, center panel).
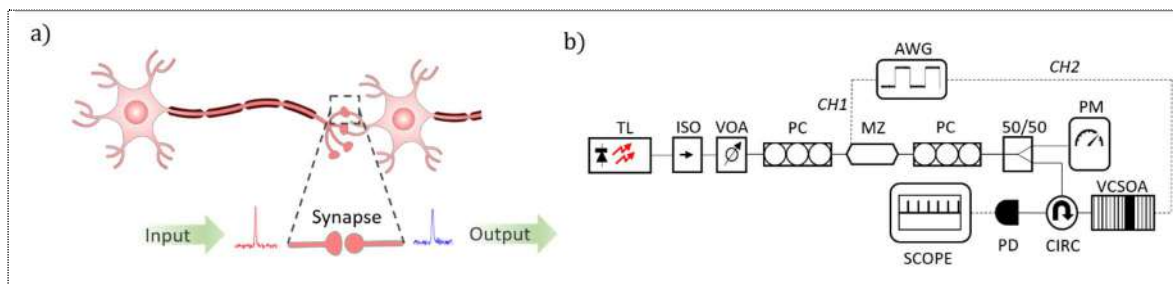


**Figure 1**: a) Illustration depicting the synaptic connection between two biological neurons b) Experimental setup used to demonstrate the photonic VCSOA synaptic element. TL-tuneable laser, ISO-optical isolator, VOA-variable optical attenuator, PC-polarization controller, MZ-Mach-Zehnder modulator, AWG-arbitrary waveform generator PM-power meter, CIRC-circulator, PD-photodetector, SCOPE-oscilloscope.

## 3. Results and discussion

Figures 2a-c show the VCSOA's response to incoming light pulses for different values of applied bias currents. At $I$ =2.179mA the relatively large wavelength detuning between $\lambda_{TL}$ and the $\lambda_{VCSOA}$ (-9.32GHz), as shown in the left-most panel of Figure 2c, results in a low optical amplitude response (shown in Figure 2c right-most panel). As the VCSOA's bias current is increased to 2.210mA, $\lambda_{VCSOA}$ approaches $\lambda_{TL}$ (-5.62GHz) and the resulting output signal is weighted by a factor of 0.77 (Figure 2b). When the applied current is increased further to 2.245mA, the frequency separation between the TL and VCSOA's peaks decreases (-2.81GHz), and the amplified optical pulse reaches a peak intensity of 75.9$\mu$W (Figure 2a). A plot of output optical pulse peak power dependence on bias current $I$ is shown in Figure 2d, which follows a non-linear trajectory as shown by the Gaussian fit. Figure 2d clearly shows the system's ability to perform synaptic behavior, enabling full and controllable tuning of the output strength of incoming fast optical pulses (150ps-long) emulating neuronal spikes simply by using the VCSOA's applied bias current $I$ as weighting mechanism. Moreover, we demonstrate the system's ability for high-speed weight tuneability. For this experiment, we used a commercial 1300 nm-VCSEL ($I_{th} = 0.77$mA at $T$ =293K) with a dominant parallel mode at $\lambda_{VCSOA} \approx$ 1290nm at threshold. The VCSOA current was directly modulated (via channel 2 (CH2) of the AWG) with a 500MHz square-wave signal alternating the current between a low (0.70mA) and a high (0.73mA; 95%$I_{th}$) value every 2ns (figure 2e). In parallel, the TL was modulated (via the MZ modulator and CH1 of the AWG) to produce an optical signal consisting of 150ps-long pulses separated by 2ns (figure 2f). This signal was optically-injected into the VCSOA, frequency matched to its main resonant peak. The direct current modulation allows the photonic synapse to dynamically adjust the weights of the incoming signal (at a fast rate of 0.5GHz) yielding low and high amplitude optical pulses on-demand at the VCSOA's output (figure 2g).
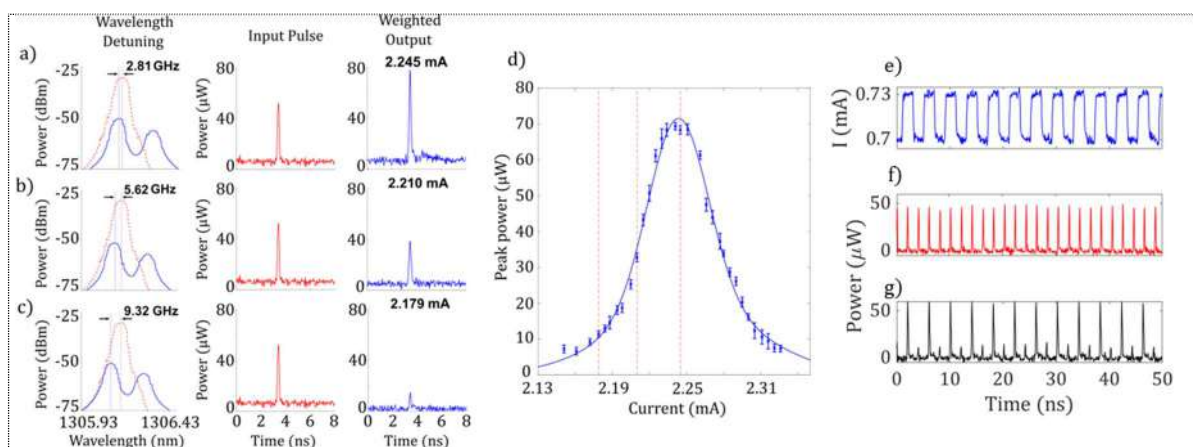


**Figure 2**: Photonic synapse with a VCSOA via wavelength detuning control. The spectra highlight the conditions for c) low (-9.32 GHz), b) moderate (-5.62 GHz) and a) high (-2.81 GHz) weighting of a 150ps-long optical pulse (shown in the middle panels). The right-most panels show the weighted optical outputs for VCSOA's bias currents of 2.245, 2.210, and 2.179mA. d) Output pulse peak power *vs.* bias current $I$. Values marked by red vertical lines are those used in plots a) to c). e) Modulation signal used to drive the VCSOA's bias current between a low (0.70 mA) and a high (0.73 mA) level. f) Injected optical signal. g) Recorded VCSOA output showing high-speed weight tuneability of input optical pulses.

## 4. Conclusion

We demonstrate controlled weighting of optical pulses (emulating neuronal spikes) with a telecom-wavelength VCSOA, functioning as a photonic synapse, using the device's bias current as the weight tuning mechanism. By utilizing the VCSOA's nonlinear gain below threshold, it is possible to apply controllable weights to fast (150ps-long) optical pulses and achieve output optical strengths ranging from values close to zero power to amplified signals. Additionally, the system permits high-speed dynamic weight control, by modulating the device bias current with user-defined signals. This result demonstrates the potential of VCSOAs as a hardware-friendly photonic synaptic element in neuromorphic spike-processing platforms for future light-based artificial intelligence systems.

## 5. References

[1] J. Robertson, E. Wade, Y. Kopp, J. Bueno, and A. Hurtado, "Toward Neuromorphic Photonic Networks of Ultrafast Spiking Laser Neurons," *IEEE J. Sel. Top. Quantum Electron.*, vol. 26, no. 1, pp. 1–15, Jan. 2020, doi: 10.1109/JSTQE.2019.2931215.

[2] X. Zhuge, J. Wang, and F. Zhuge, "Photonic Synapses for Ultrahigh-Speed Neuromorphic Computing," *Phys. status solidi – Rapid Res. Lett.*, vol. 13, no. 9, p. 1900082, Sep. 2019, doi: 10.1002/pssr.201900082.

[3] S. Xiang, Y. Zhang, J. Gong, X. Guo, L. Lin, and Y. Hao, "STDP-Based Unsupervised Spike Pattern Learning in a Photonic Spiking Neural Network With VCSELs and VCSOAs," *IEEE J. Sel. Top. Quantum Electron.*, vol. 25, no. 6, pp. 1–9, Nov. 2019, doi: 10.1109/JSTQE.2019.2911565.

[4] A. Hurtado, I. D. Henning, and M. J. Adams, "Bistability and nonlinear gain in 1.55µm vertical cavity semiconductor optical amplifiers: Theory and experiments," *Appl. Phys. Lett.*, vol. 91, no. 15, p. 151106, Oct. 2007, doi: 10.1063/1.2798053.

# Oxide-Confined vs. Buried Tunnel Junction VCSELs

**A. Gullino*,[1], S. Pecora[1], A. Tibaldi[1,2], F. Bertazzi[1,2], M. Goano[1,2], P. Debernardi[2]**

[1] *Dipartimento di Elettronica e Telecomunicazioni, Politecnico di Torino, Corso Duca degli Abruzzi 24, 10129 Torino, Italy*
[2] *CNR-IEIIT, Corso Duca degli Abruzzi 24, 10129 Torino, Italy*
*\*Email: alberto.gullino@polito.it*

**Abstract:** We present a theoretical comparison of the *LI* characteristics of 850 nm GaAs/AlGaAs oxide-confined VCSEL and an equivalent BTJ-VCSEL. The oxide-confined *pin* VCSEL model is calibrated on experiments and BTJ-VCSEL simulation is based on a NEGF-drift-diffusion approach. The comparison points to the improvements provided by BTJ-VCSELs, also considering thermal effects.

## 1. Introduction

All commercial vertical-cavity surface-emitting lasers (VCSELs) emitting in the near-IR (850–980 nm) are based on *pin* devices. In these VCSELs, optical and electrical confinement are achieved by an oxide aperture, realized by a wet oxidation of a thin AlAs layer, just above the cavity. An alternative approach could involve a buried tunnel junction (BTJ) [1], which would get rid of the hardly controllable wet oxidation process and of majority of *p*-doped layers, hence enabling low-resistance paths to a well-defined active region. With respect to long wavelength VCSELs, where carrier injection can be achieved only from BTJs, in 850 nm VCSELs this approach has never been demonstrated. This is in part due to the success of the oxide confinement technology, in part to the more difficult operation of BTJs in semiconductors with larger gaps. However, the poor conductivity of *p*-doped layers in GaN-based VCSELs has prompted the adoption of BTJs also at much wider energy gaps, with encouraging results [2]. The scope of this paper is to demonstrate the benefits of BTJ-VCSELs by presenting a comparative study with an equivalent oxide-confined (OC-) VCSEL.

## 2. Model description

This work is based on our in-house 1D drift-diffusion simulator D1ANA, self-consistently coupled with a nonequilibrium Green function (NEGF) formalism describing rigorously the quantum tunneling in the TJ region [3]. The coupling is obtained by extracting from NEGF a tunneling generation rate which is then introduced alongside Auger, SRH and radiative GR rates in the carrier continuity equations. Quantum wells (QWs) are modeled by adopting quantum corrections via 2D populations coupled to bulk ones through a capture time. Optical simulations are based on our in-house electromagnetic simulator VELM: the extracted optical data, such as modal losses, optical confinement factor and output power coupling coefficient, allow to describe the carriers-photon coupling. The gain model is based on Fermi's golden rule, where the electronic band structure is described with the Luttinger-Kohn Hamiltonian [4]. The steady-state thermal solver is based on a 1D FEM approach.

## 3. Results and discussion

The reference *pin* VCSEL is the same of [4,5] and features a 1λ-cavity embedding three 8 nm GaAs QWs, defined by composition- and doping-graded distributed Bragg reflector (DBRs). In the BTJ-VCSEL, the highly resistive and absorbing *p*-doped DBR is replaced with a *n*-doped DBR, in such a way to achieve a threshold gain as close as possible to that of the reference OC-VCSEL. The use of a *n*-doped DBR reduces free-carrier absorption losses and self-heating [4]: both effects are considered in our solver.

In Fig. 1, the blue curves show the refractive indices of the two VCSELs in the proximity of the cavity, whereas the red curves the corresponding standing waves. The geometry must be modified to replace the high Al content layer (where oxidation takes place in the outer region) with a BTJ. An electron-blocking layer (EBL) is also introduced to reduce carrier leakage from the TJ itself [3]. This results in a 5 nm shift with respect to the OC-VCSEL, required to place the highly doped TJ in a node of the optical field.

Fig. 2 shows the band diagrams of both devices at 2 V. From the electrical standpoint, the OC-VCSEL behaves as a *pin* junction in forward bias. The BTJ-VCSEL embeds a heavily doped TJ in counter-series with the cavity diode (*n-i-p-p+n+-n*): thus, the voltage drop across the TJ is significantly smaller than the applied bias [3].

Fig. 3 reports the *LI* characteristics and the wall-plug efficiencies (WPEs). The OC-VCSEL simulation is first compared with experimental results. Starting from the parameters used in our 3D VCSEL suite [4], a parameter fitting was performed for our 1D solver, reaching a very good agreement between model and experiment [5]. Optical threshold at 0.45 mA and thermal rollover are well reproduced.

The very same parameters are then exploited to investigate the BTJ-VCSEL. The removal of all the *p*-doped layers (except the short ones in the BTJ and in the EBL) leads to a reduction of the outcoupling losses, so that the slope of the corresponding *LI* curve is significantly higher. Furthermore, the curve shows linearity on a wider range of currents, yielding an improved WPE compared to the reference oxide-confined device. As imposed by the similar optical threshold gains, the threshold currents of the two VCSELs are almost equal.
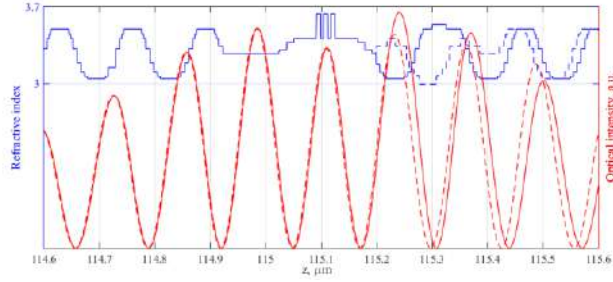
**Figure 1**: Refractive index (in blue) and standing wave (in red, from VELM) for the BTJ (continuous lines) and the OC (dashed) VCSELs. Ground contact is placed at $z = 0$ μm, output light is emitted at the right side (emission wavelength $\lambda = 847.04$ nm and threshold gain $G_{th} = 1480$ cm$^{-1}$ for the BTJ-VCSEL; $\lambda = 847.28$ nm, $G_{th} = 1410$ cm$^{-1}$ for the OC-VCSEL).
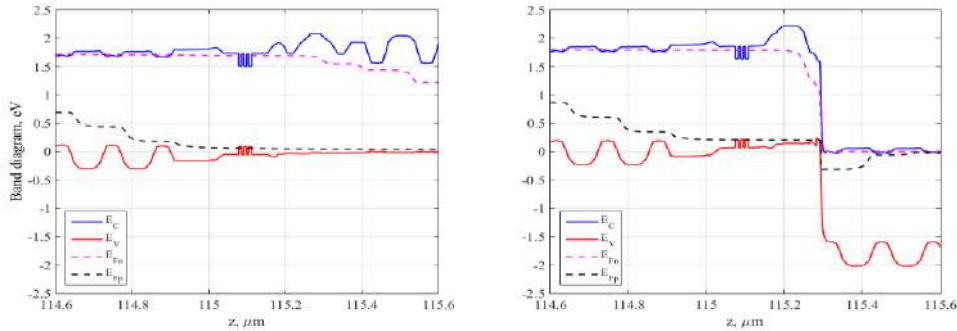


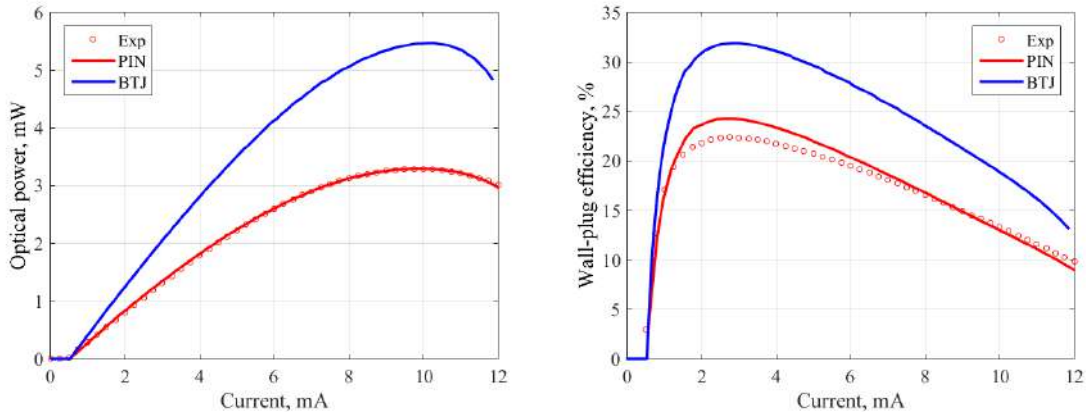**Figure 2**. Band diagram of OC-VCSEL (left) and BTJ-VCSEL (right), at 2 V.



**Figure 3**: Experimental and simulated *LI* characteristics and WPE of the OC-VCSEL (red dots and solid lines, respectively) and BTJ-VCSEL simulated curves (blue solid lines).

## 4. Conclusion

From the presented 1D analysis we can conclude that employing the BTJ-VCSEL results in a clear performance improvement: the increased slope in the linear region allows for higher output optical powers at equal current values, and thermal rollover impacts at much larger high optical powers; greater WPEs are yielded.

## 5. References

[1] P. Ortsiefer, *et al.*, "Low-resistance InGa(Al)As Tunnel Junctions for Long Wavelength Vertical-cavity Surface-emitting Lasers", *Jpn. J. Appl. Phys.*, vol. 39, pp. 1727-1729 (2000).

[2] J. T. Leonard, *et al.*, "Demonstration of a III-nitride vertical cavity surface-emitting laser with a III-nitride tunnel junction intracavity contact", *Appl. Phys. Lett.*, vol. 107, pp. 091105 (2015).

[3] A. Tibaldi, *et al.*, "Carrier transport analysis of tunnel junction VCSELs by a coupled NEGF-DD approach", *Phys. Rev. Appl.*, vol. 14, pp. 024037 (2020).

[4] P. Debernardi, *et al.*, "Probing Thermal Effects in VCSELs by Experiment-Driven Multiphysics Modeling", *IEEE J. Select. Topics Quantum Electron.*, vol. 25, pp. 1700914 (2019).

[5] A. Gullino, *et al.*, "Reduced Dimensionality Multiphysics Model for Efficient VCSEL Optimization", *Appl. Sci.*, vol. 11, pp. 6908 (2021).

# 1.5 GHz VECSEL-based Laser System for Ultrafast Multicontrast Nonlinear Imaging

**Thibault A.G Bondaz[1,2]\*, R. Jason Jones[1], Jerome V. Moloney[1] and John G. McInerney[2]**

[1]*Wyant College of Optical Sciences, University of Arizona, 85721 Tucson, USA*
[2]*Department of Physics and Tyndall Institute, University College Cork, Cork, Ireland*
*\*bondaz.thibault@gmail.com*

**Abstract:** We present a 1.5 GHz broadband laser system based on a vertical-external-cavity surface-emitting-laser (VECSEL). Its high repetition rate coupled with pulse shaping via Multiphoton Intrapulse Interference Phase Scan (MIIPS) makes our system an ideal source for ultrafast multicontrast nonlinear imaging while mitigating the risks of photobleaching and photodamage.

## 1. Introduction

Photobleaching and photodamage are considerable concerns in the domain of nonlinear imaging, especially when measuring weak signals requiring long acquisition times. In such cases, often the solution of increasing the pulse energy is not an option as photoinduced damage tends to scale rapidly with intensity [1].

At constant pulse energy, the scanning speed can scale with the repetition rate, allowing for an improved signal to noise ratio by reducing the amount of integrated noise while mitigating the risk of photodamage when the pulse energy is reduced accordingly [2].

Consequently, there is a strong motivation in increasing the repetition rate of probe lasers used in such applications. We believe that the intrinsic high repetition rate, low noise and low timing jitter of the VECSEL platform make it an ideal source for nonlinear imaging and spectroscopy.

## 2. Model description, experimental setup

Our laser generates a supercontinuum ranging from 900nm to 1200nm via a photonic crystal fiber from which the spectral phase and amplitude are controlled with a Spatial Light Modulator (SLM) in the Fourier plane of the incident beam. The generation of the second harmonic is used as feedback in a MIIPS scheme to retrieve the original spectral phase of the supercontinuum.

The oscillator is a VECSEL passively modelocked with a semiconductor saturable absorber mirror (SESAM) with a 1.5 GHz pulse repetition rate and central wavelength of ~1030 nm. The gain chip consists of a distributed Bragg reflector (DBR) followed by an active region containing 10 quantum wells arranged in a resonant periodic gain (RPG) configuration. Its surface is coated with a bilayer of $Ta_2O_5$ and $SiO_2$ for dispersion control and reducing the filtering effect of the device micro-cavity.
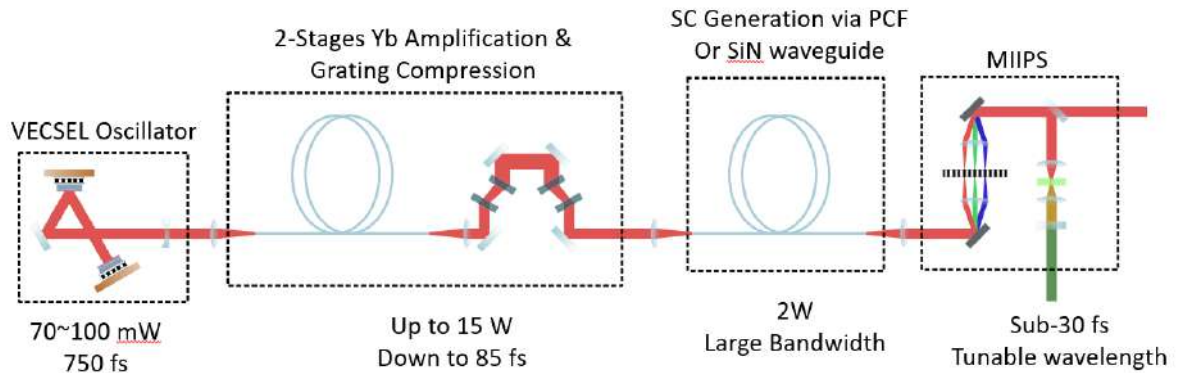


**Figure 1 : Experimental setup. The output of a VECSEL (750 fs, 1.5 GHz, 90 mW average) is amplified with a two stage YDFB (only one stage is presented on the schematic), compressed with gratings (100 fs, 5 W) and used as seed in a PCF (2 W, 300 nm bandwidth). The spectral phase/amplitude is controlled with an SLM while the second harmonic is used to retrieve the incident spectral phase.**

The output of the oscillator is amplified with a two-stage ytterbium doped fiber amplifier and compressed with two pairs of gratings before propagating through the PCF.

## 3. Results and discussion

We use a pulse shaper coupled with a MIIPS scheme, an iterative method to retrieve the spectral phase of an incident beam by applying a series of known spectral phase offsets to its spectrum and observing the resulting changes in its second harmonic generation, allows complete control of the spectral phase and amplitude of the incident beam., to generate ~30 fs transform-limited pulses across the whole supercontinuum (900-1200 nm), and to tailor the spectral phase to a specific application such as CARS.
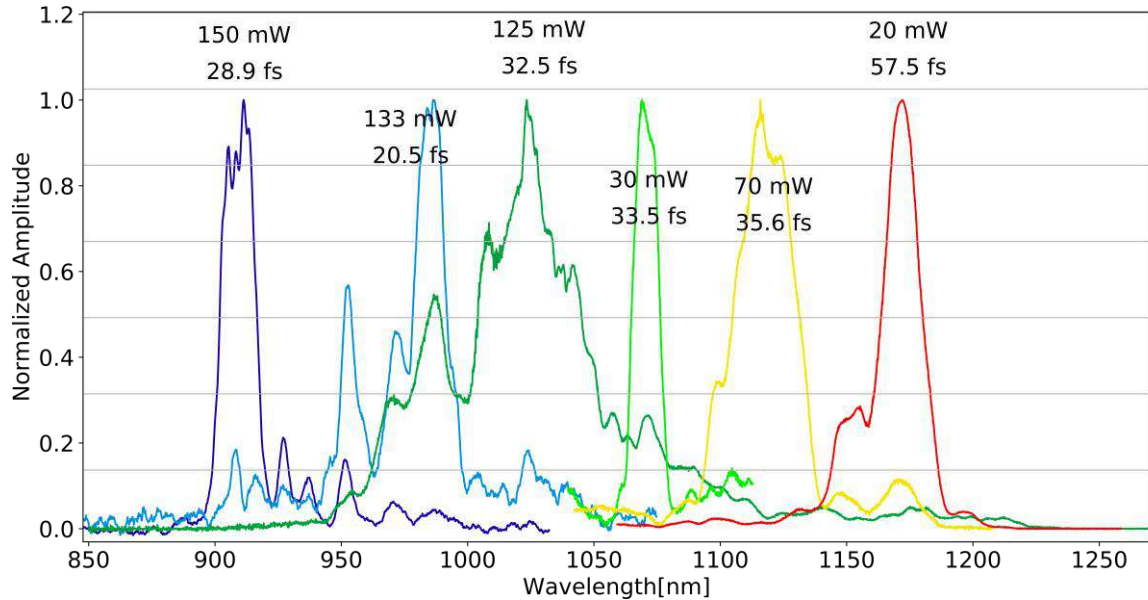


**Figure 2 : Spectral splicing with a spatial light modulator. The measured average power as well as pulse duration are displayed for each splice. The pulse durations have been confirmed independently with an autocorrelator.**

The result is a 1.5 GHz widely tunable laser producing transform limited pulses with up to 3 kW peak power.

## 4. Conclusion

We have presented a broadband laser system based on a VECSEL. We believe that its intrinsically high repetition rate could have beneficial applications in high-speed nonlinear imaging, especially in mitigating the risk of photoinduced damage. Furthermore, in some applications, matching the repetition rate to the fluorescence lifetime could significantly improve the signal strength. The use of a pulse shaper allows us to compress multiple channels to their transform limited time duration or to tailor the spectral phase to any arbitrary function.

## 5. References

[1]     Patterson, G.H. & Piston, D.W. Photobleaching in two-photon excitation microscopy. Biophys. J. 78, 2159–2162 (2000).
[2]     Ji, N., Magee, J. & Betzig, E. High-speed, low-photodamage nonlinear imaging using passive pulse splitters. Nat Methods 5, 197–202 (2008). https://doi.org/10.1038/nmeth.1175

# Abstract

## Session III: Frequency Combs & Semiconductor Laser Applications

# Measuring the Linewidth Enhancement Factor during Frequency Comb Operation

**Nikola Opačak[1*], Florian Pilat[1], Dmitry Kazakov[1, 2], Sandro Dal Cin[1], Georg Ramer[3], Bernhard Lendl[3], Federico Capasso[2], Gottfried Strasser[1] and Benedikt Schwarz[1, 2]**

*[1] Institute of Solid State Electronics, TU Wien, Gusshausstrasse 25-25a, 1040 Vienna, Austria*
*[2] John A. Paulson School of Engineering and Applied Sciences, Harvard University, Cambridge, Massachusetts*
*[3] Institute of Chemical Technologies and Analytics,TU Wien, Getreidemarkt 9/164, A 1060 Vienna, Austria*
*\*nikola.opacak@tuwien.ac.at*

**Abstract:** The linewidth enhancement factor (LEF) is known as an important property of semiconductor lasers. Recently, it is gaining more interest due to its key role in frequency comb operation. However, as of yet existing techniques to measure the LEF are limited to sub-threshold bias or single-mode operation. Here, we introduce a novel and universally applicable method to directly obtain the spectrally resolved LEF of a running laser frequency comb. The technique utilizes a phase-sensitive single shot measurement scheme. We derive a theoretical model, which is investigated by extensive Maxwell-Bloch simulations and demonstrated in an experiment on a quantum cascade laser.

## 1. Introduction

Semiconductor frequency comb lasers are compact, electrically pumped sources of coherent light that find application in areas such as high-precision spectroscopy for medical and chemical sensing. The linewidth enhancement factor (LEF) is well-established in the theoretical description of such lasers and plays a key role in understanding dynamic processes like laser linewidth broadening, modulation response and comb dynamics and even soliton formation [1,2]. Therefore, the knowledge of its value is of utmost importance. Previously experimental investigation was limited to measurements below the lasing threshold or single-mode operation.

## 2. Model description, experimental setup

Here we present a novel modulation technique which enables the measurement of the LEF of an arbitrary, running laser source [3]. In the case of a frequency comb we can infer the LEF over the whole laser spectrum in a single-shot measurement. This is enabled by a phase-sensitive measurement scheme called "Shifted Wave Interference Fourier Transform Spectroscopy" (SWIFTS) [4] and the modulation of the driving current. This modulation leads to small sidebands at each of the comb modes. A sketch of the experimental setup can be seen in Fig. 1a. An RF-optimized quantum well infrared photodetector (QWIP) is used to record the beatings of the laser modes with their modulation sidebands. The theoretical model is investigated vastly using numerical simulations of a spatio-temporal model based on Maxwell-Bloch formalism [5]. Then the method is demonstrated experimentally on a quantum cascade laser frequency comb.
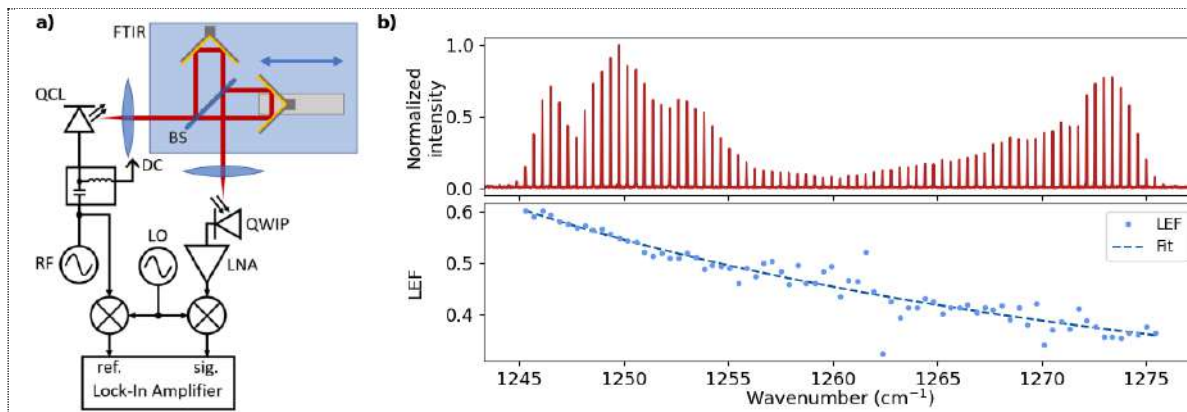


**Figure 1**: a) Experimental Setup, b) Laser comb spectrum (top), Spectrally-resolved LEF with fit (bottom)

## 3. Results and discussion

The LEF values obtained from numerical simulations show an excellent agreement with analytical expressions for both, single-mode and also frequency comb laser operation. The results of the experiment on a quantum cascade laser are depicted in Fig. 1b). At the top the frequency comb emission spectrum of the laser can be seen. For each of these modes a LEF value is calculated and shown in the graph below (markers). The results follow the shape of the analytic model, that has been fitted to the data.

## 4. Conclusion

We developed a measurement technique for the linewidth enhancement factor for an arbitrary type of laser, working over the whole bias range. It was studied first with elaborate numerical simulations and then demonstrated on a frequency comb laser. Both compare well to the analytic description.

## 5. References

[1]     M. Osinski et al, "Linewidth broadening factor in semiconductor lasers: An overview", IEEE J. Quant. Electron., (1987)

[2]     N. Opačak et al, "Frequency comb generation by Bloch gain induced giant Kerr nonlinearity", arXiv:2102.08167 [physics.optics], (2021)

[3]     N. Opačak et al, "Spectrally resolved linewidth enhancement factor of a semiconductor frequency comb", arXiv:2104.05747 [physics.optics], (2021)

[4]     D. Burghoff et al, "Terahertz laser frequencycombs," Nat. Photonics, (2014)

[5]     N. Opačak et al, "Theory of Frequency-Modulated Combs in Lasers with Spatial Hole Burning, Dispersion, and Kerr Nonlinearity", Phys. Rev. Lett., (2019)

# Gain-switched Optical Frequency Combs with comb spacing down to 5 MHz

**C. Quevedo-Galán\*, P. López-Querol, A. Pérez-Serrano, J.M.G. Tijero and I. Esquivias**

*CEMDATIC - E.T.S.I. Telecomunicación, Universidad Politécnica de Madrid, 28040 Madrid, Spain*
*\*clara.quevedo.galan@upm.es*

**Abstract:** We report flat and wide low-frequency Optical Frequency Combs generated by pulsed gain-switching of optically injected semiconductor lasers. Combs as wide as 133 GHz at 100 MHz repetition rate and good quality combs at a record low frequency of 5 MHz were obtained.

## 1. Introduction

Semiconductor lasers are gaining increasing relevance for the generation of Optical Frequency Combs (OFCs) due to their well-known advantages in terms of high efficiency, low cost, small footprint, and suitability for photonic integration. Gain-switching (GS) is a convenient technique for generating OFCs due to its easy implementation, and especially to its controllable repetition rate [1]. High repetition rate OFCs (> 1 GHz) find applications in optical communications and subterahertz generation, while low repetition rate OFCs (< 1 GHz) are well suited for spectroscopy and ranging applications.

We have previously reported low frequency OFCs generated from semiconductor lasers by using pulsed GS together with optical injection [2]. These OFCs at 100 MHz were later applied to Dual Comb Spectroscopy (DCS) with excellent results [3]. In this work we report OFCs with a 10 dB width of 133 GHz at 100 MHz and demonstrate the generation of broad OFCs at low repetition rates down to 5 MHz.

## 2. Experimental setup
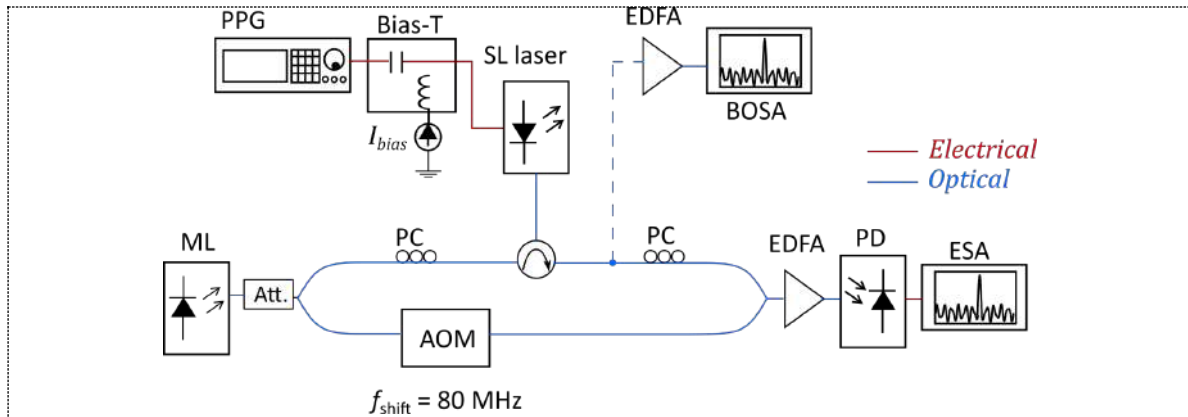


**Figure 1**: (a) Experimental setup to generate the OFCs by gain switching with optical injection (upper part) and to characterize the OFCs using the heterodyne technique (lower part). ML: master laser. SL: slave laser. PPG: pulse pattern generator. Att: attenuator. PC: polarization controller. AOM: acousto-optic modulator. EDFA: erbium doped fiber amplifier. PD: photodetector. BOSA: Brillouin optical spectrum analyzer. ESA: electrical spectrum analyzer.
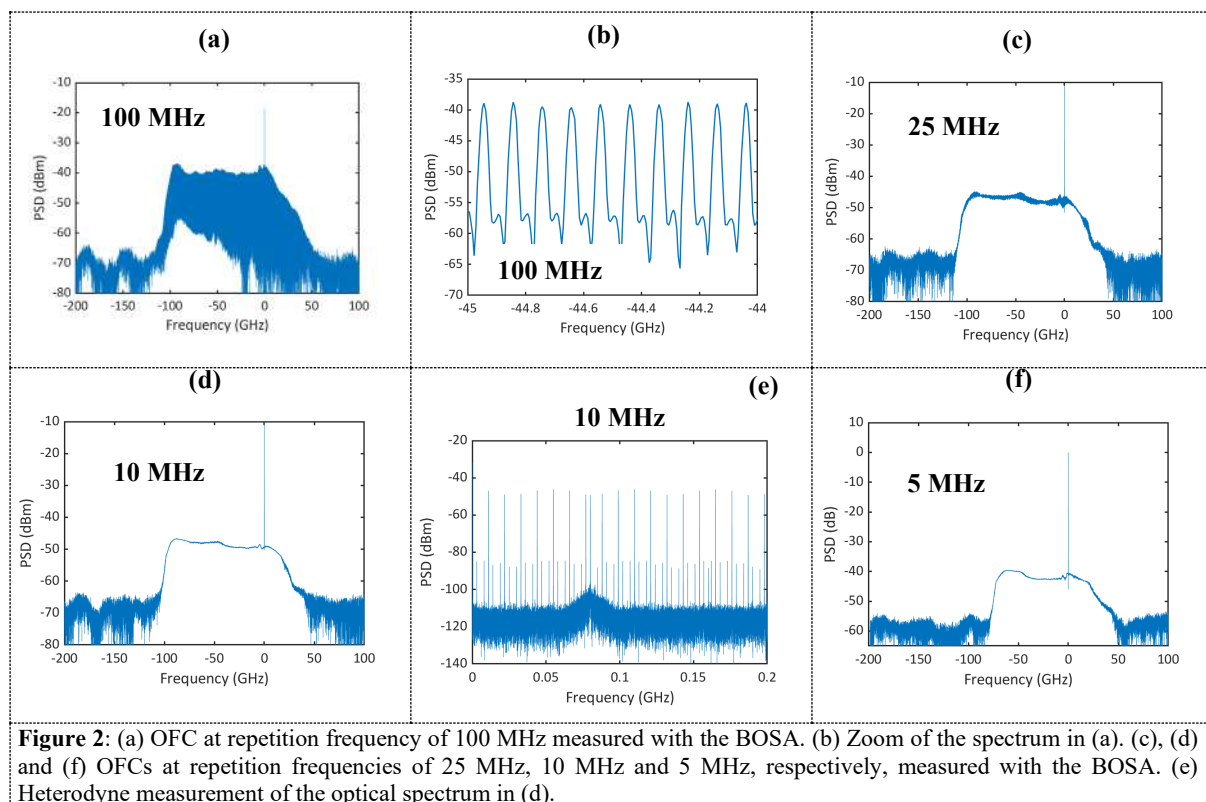
Fig. 1 shows the experimental setup used for the generation and characterization of the OFCs. A high speed distributed feedback laser was used as slave laser (SL) and a low-noise tunable laser was used as the master laser (ML) which was set at an injection wavelength $\lambda_{inj}$ = 1549.57 nm and at an injection power of -3 dBm. The detuning between the master and the slave laser was controlled by slightly changing the operating temperature of the slave laser. The gain-switching operation of the slave laser was achieved by driving it with two electrical signals combined using a bias-tee: a bias current ($I_{bias}$) and a train of pulses provided by a pulse pattern generator, at a repetition frequency $f_r$ between 5 and 100 MHz. For reaching high pulse amplitudes, a wide-bandwidth RF amplifier was used.

The optical spectra of the OFC were measured using a high resolution (10 MHz) Brillouin Optical Spectrum Analyzer (BOSA). In the case of the low repetition rate combs (< 25 MHz), the individual comb lines could not be clearly resolved with the BOSA, and a heterodyne technique was used to measure the optical spectrum. In this case, the OFC was beaten with the ML, whose frequency was shifted 80 MHz by means of an Acousto-Optic Modulator (AOM), and the RF spectra were measured with an electrical spectrum analyzer. A detailed analysis of the RF spectra provided a reconstruction of the original optical spectra.

## 3. Results

Fig. 2(a) shows the best OFC obtained at 100 MHz after optimizing the pulse amplitude (8 $V_{pp}$), pulse duration (200 ps) and bias current (0.5 mA). It features a 10 dB bandwidth of 133.2 GHz, i.e., 1332 lines, which is a record for a gain-switched semiconductor laser at low frequency. The carrier-to-noise ratio is around 15 dB, limited by the background noise, as it can be observed in the zoom shown in Fig. 2b, where the individual harmonics are clearly resolved.

High quality OFCs with similar widths were obtained al lower frequencies down to 5 MHz. Fig. 2(c) shows an OFC obtained at a repetition frequency of 25 MHz, where the individual lines appear as tiny ripples due to the limited resolution of the BOSA. At 10 MHz (Fig. 2(d)), the ripples are not any more apparent, but the OFC tones are still present, as it can be seen in the RF heterodyne spectrum shown in Fig. 2(e). The down-converted spectrum is centered at the AOM shift frequency (80 MHz). We used 11 MHz instead of 10 MHz to avoid overlapping of the harmonics. Clearly resolved harmonics around 20 dB above the background can be observed. The high intensity peaks in this figure correspond to the direct modulation terms. The OFC at 5 MHz, which is the lowest reported frequency for a gain switched semiconductor laser, as far as we know, is shown in Fig. 2 (f).



**Figure 2**: (a) OFC at repetition frequency of 100 MHz measured with the BOSA. (b) Zoom of the spectrum in (a). (c), (d) and (f) OFCs at repetition frequencies of 25 MHz, 10 MHz and 5 MHz, respectively, measured with the BOSA. (e) Heterodyne measurement of the optical spectrum in (d).

## 4. Conclusion

These results demonstrate that low repetition rate OFCs generated by pulsed GS of optically injected semiconductor lasers are a promising tool for DCS and ranging systems requiring high frequency resolution. The achieved resolution of 5 MHz is a first stage towards the sub-MHz resolution required by sub-Doppler spectroscopy.

## 5. References

[1]     P. M. Anandarajah, R. Maher, Y. Q. Xu, S. Latkowski, J. O'Carroll, S. G. Murdoch, R. Phelan, J. O'Gorman, and L. P. Barry, "Generation of Coherent Multicarrier Signals by Gain Switching of Discrete Mode Lasers," IEEE Photonics J. vol. 3, pp. 112–122 (2011).

[2]     A. Rosado, A. Pérez-Serrano, J. M. G. Tijero, Á. Valle, L. Pesquera, and I. Esquivias, "Enhanced optical frequency comb generation by pulsed gain-switching of optically injected semiconductor lasers," Opt. Express vol. 27, pp. 9155–9163 (2019).

[3]     C. Quevedo-Galán, V. Durán, A. Rosado, A. Pérez-Serrano, J. M. G. Tijero, and I. Esquivias, "Gain-switched semiconductor lasers with pulsed excitation and optical injection for dual-comb spectroscopy," *Opt. Express*, vol. 28, no. 22, p. 33307, (2020).

# Investigation of the wavelength tuning of an integrated laser system system on InP for Optical Coherence Tomography.

**J. Hazan,[1]\* T. Couka[2], R. Pajkovic[1], K.A. Williams[1], E.A.J.M. Bente[1]**

[1]*Photonic Integration Group, Department of Electrical Engineering, Eindhoven University of Technology, PO Box 513,5600MB Eindhoven The Netherlands*
[2]*Ecole Nationale Supérieure d'Ingénieurs de Caen (ENSICAEN) CS 45053 - 14050 CAEN Cedex 4 - FRANCE*
*\*E-Mail: j.hazan@tue.nl*

**Abstract:** We present results of two ways of calibrating an InP monolithically integrated widely tunable laser system for optical coherence tomography (OCT) applications. To tune the laser over 90 nm between 1480 and 1570 nm, applying 8 reversely bias voltage control settings on electro-refractive modulators which are responsible for the laser wavelength selection, with low thermal dissipation. The OCT requirements of a 1 GHz resolution and stable calibration are addressed, and a strategy to select the lasing wavelengths, over its tuning range, is discussed.

## 1 Introduction

Widely tunable laser systems are widely used for sensing and biomedical imaging applications [1]. In biomedical imaging with optical coherence tomography, frequency swept lasers have enabled imaging speed of several thousands of scans per second [2]. In this way is possible to perform a more accurate representation of the tissue topology due to the minimization of motion artifacts [3]. In this paper we report a study of the stepwise tuning with 90 pm steps of an over 90 nm widely tunable laser system. The filters are firstly studied separately and then an experimental control strategy to obtain a laser wavelength calibration, suitable for an OCT measurement, is described.

## 2. Laser Tuning and Wavelength selection mechanism

In this work, we investigated a tunable laser design [3], which presents 3 cascaded asymmetric Mach-Zehnder Interferometers (AMZI) in series as filters and a balanced Mach-Zehnder modulator, used as variable out-coupler. The three filters from coarse to fine have a free spectral range (FSR) of 102.6, 9.7 and 0.9 nm, while the FSR of the cavity is 90pm (10GHz). Figure 1a depicts the lasing spectra from this laser as function of the three filters and the out-coupler tuning. From the measurements it is possible to conclude that this laser can tune over 90 nm, with 90 pm steps, with single mode lasing and side mode suppression ratio (SMSR) between 20 and 45 dB. Figure 1b shows the photocurrent generated on the laser amplifier (SOA) from the injection of external laser light at 1550 nm, measured for different reverse bias voltages on one arm of the variable out-coupler. These results allow estimating the outcoupling fraction, the increase in cavity losses and the widening of the tuning range, as function of reverse bias voltage on the out-coupler.
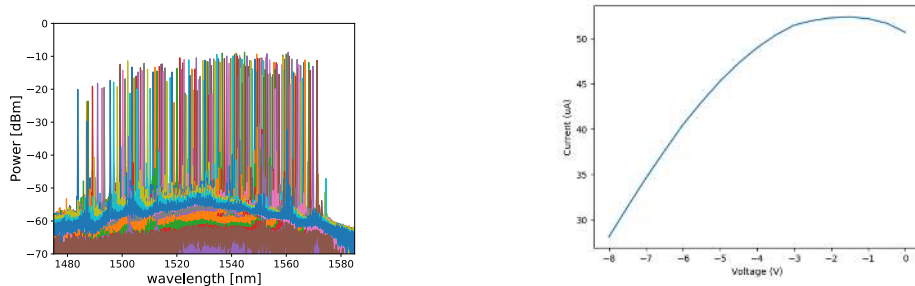


*Figure 1: a) Spectra measurements to show the max tuning range. b) SOA detected photocurrent as function of the out-coupler voltage.*

To make this laser suitable as a source for OCT measurements, a wide tuning range is essential but not sufficient. The laser needs to scan between single mode lasing wavelengths with equal wavelength spacing over the full range. To gain better knowledge on the laser operation we first perform filter sweeps to investigate their individual behavior. During the measurements, 120 mA of constant current were injected into the SOA and the variable out-coupler was constantly biased at -2V, where we expect to have highest threshold current. For the first step a wavelength map is obtained, shown in Figure 2a, with the coarse and the medium filters as already done on previous laser designs [5]. Figures 2b shows the behavior of a single point in Figure 2a as function of the fine filter for both the lasing wavelength and the side mode suppression ratio (SMSR). The fine filter tuning appears to behave as a set of discrete wavelengths, where the SMSR varies. Keeping fixed the coarse, the medium filter and the cavity modes, the tuning of the fine filter acts as a longitudinal mode filter as can be extracted from the

parabolic behavior of the SMSR with respect to the arm voltage difference. To achieve higher resolution on the tuning, the last step is to tune the longitudinal cavity modes trough the tuning of both arms of every filter stage. The lasing spectra in Figure 2c) reveal how this finest calibration step helps to find 10 pm (1.1 GHz) spaced lasing points, which is the resolution of the optical spectrum analyzer (OSA) used to measure the spectra. Unfortunately, the tuning cannot cover the full cavity mode FSR (90 pm), due to the 1 mm length of the phase modulators inside the filters, which reduces the phase change efficiency.
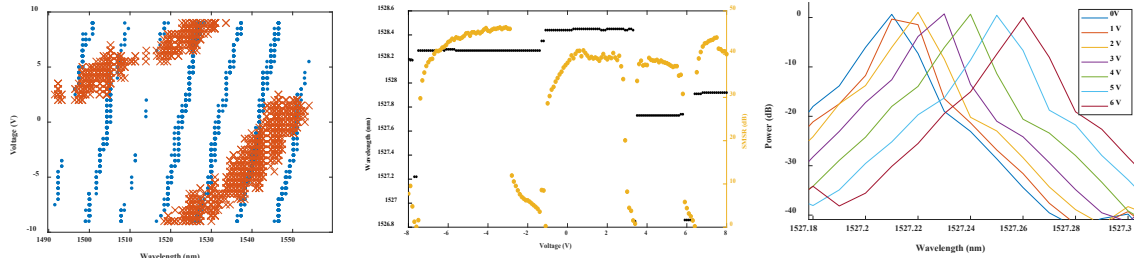


*Figure 2 a) Calibration of the coarse (red) and medium (blue) filters. b) Fine filter tuning. c) Laser spectra during the cavity mode tuning.*

## 3. Control strategy for OCT

The filters calibration is not stable over time due to temperature variations within the circuit during its operation time. Long time measurements on a packaged laser revealed a 10 pm shift every 4 hours of continuous operation. It is indeed important to develop a fast calibration of the laser before every use of this laser for OCT measurements. For this purpose, we developed a control strategy to obtain 10 GHz (90 pm) spaced wavelength points in a fast and reliable way. We split the output of the tunable laser with a 90/10 coupler. The smallest fraction of the power is sent to a grating filter and then to a power detector to optimize the wavelength, while the biggest fraction is sent to an OSA to check the laser spectra. The grating filter is set to the target wavelength and starting from a fixed setting for the coarse and the medium filters, we sweep the fine filter and the cavity modes until we find the maximum power read by the detector. The laser peak is then detected with an OSA and the control settings are recorded. In this way is possible to obtain 1000 different lasing wavelengths and save the corresponding control settings to achieve them. Figure 3a shows the 90pm wavelength points obtained in that way over a 5 nm window centered at 1543 nm, and figure 3b shows the deviation from the initial targeted wavelength with respect to the measured one. The error on the correct wavelength detection is very likely due to the grating filter inaccuracy because it presents a 3dB bandwidth of 1 nm. Currently every point search takes little less than a minute with this new technique, but it can be improved down to tens of μs per point with proper synchronization between the computer the voltage control inputs and the use of the power meter register to temporarily store the data.
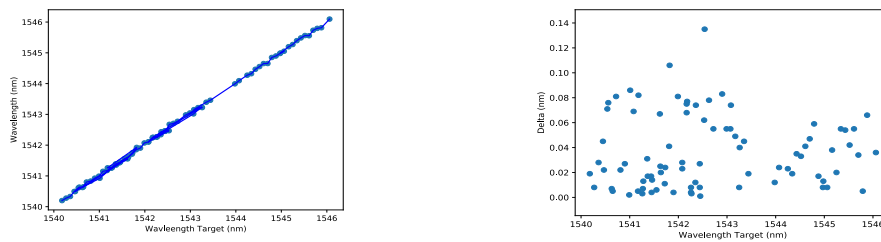


*Figure 3 a) Wavelength detected with the control strategy and b) deviation with respect to the target wavelength of the grating filter.*

## 4. Conclusions

After a proper analysis of the behavior of the three intra-cavity filters, a fast characterization technique to tune the laser system over 90 nm with 90 pm steps has been implemented to make this device suitable for a high accurate OCT system. The calibration can be further improved in terms of accuracy and speed with the use of better resolution equipment and the implementation of algorithms to look for the control settings.

## 5. References

[1] L. A. Coldren, G. A. Fish, Y. Akulova, J. S. Barton, L. Johansson, and C. W. Coldren, "Tunable Semiconductor Lasers: A Tutorial," *J. Light. Technol.*, vol. 22, no. 1, pp. 193–202, 2004, doi: 10.1109/JLT.2003.822207.

[2] R. Huber, "Fourier domain mode locking (FDML): A new laser operating regime and applications for biomedical imaging, profilometry, ranging and sensing," *Opt. InfoBase Conf. Pap.*, vol. 14, no. 8, pp. 1981–1983, 2009, doi: 10.1364/assp.2009.ma1.

[3] M. Wojtkowski *et al.*, "Three-dimensional retinal imaging with high-speed ultrahigh-resolution optical coherence tomography," *Ophthalmology*, vol. 112, no. 10, pp. 1734–1746, 2005, doi: 10.1016/j.ophtha.2005.05.023.

[4] S. Latkowski *et al.*, "Monolithically integrated widely tunable laser source operating at 2 μm," *Optica*, vol. 3, no. 12, p. 1412, 2016, doi: 10.1364/optica.3.001412.

[5] R. Pajković, Y. Tian, S. Latkowski, K. A. Williams, and E. A. J. M. Bente, "Tuning of a widely tunable monolithically integrated InP laser for optical coherence tomography," vol. 1093912, no. March 2019, p. 37, 2019, doi: 10.1117/12.2509572.

# A Technique for Extracting the Carrier Lifetime of a Reversely Biased Semiconductor Optical Amplifier with Two Free Running Lasers

**L. Nielsen,[1]\* M. Heck[1,2]**

[1]*Department of Electrical and Computer Engineering, Aarhus University*
[2]*Department of Electrical Engineering, Eindhoven University of Technology*
*\*ln@ece.au.dk*

**Abstract:** The carrier lifetime of a semiconductor optical amplifier (SOA) is an important parameter, for example, when simulating and designing mode-locked laser diodes. However, for reversely biased SOAs the carrier lifetime is short, and typically determined by the use of sophisticated measurement techniques such as pump-probe. In this paper we experimentally extract the carrier lifetime by utilizing two tunable lasers and a 50-GHz bandwidth electrical spectrum analyzer.

## 1    Introduction

Mode-locked laser diodes (MLLDs) have a great potential in several applications such as optical analog-to-digital converters [1] and low-noise microwave oscillators [2]. A crucial part of a passively MLLD is the semiconductor optical amplifier (SOA). Typically two SOA sections are included, one in forward bias to provide gain, and another in reverse bias to act as a saturable absorber (SA). The dependency between the carrier lifetime $\tau_c$ of the SOA and SA, and the cavity round-trip time, is essential to achieve stable passive mode-locking. Thus, it is desirable to determine these constants in order to enable MLLD simulation and design. Typically, since $\tau_c$ is very small for SAs, it is often measured with pump-probe experiments [3]. However, such setups are complex and typically not part of the default optical laboratory inventory. Alternatively, $\tau_c$ can be estimated from the opto-electronic bandwidth of an SA when used as a photodiode [4], however this method demands a very high bandwidth of the RF signal generator, in order to resolve very small values of $\tau_c$ and probe on-chip contact pads.

In this work we propose a simple method that utilizes all-optical RF generation by beating two free-running tunable lasers, and an electrical spectrum analyzer (ESA) for measuring the output RF signal.

## 2. Theory and experimental setup

Theoretically, an expression similar to what was found in [5], is found within the framework presented by Vladimirov and Turaev [6]. By doing a small signal analysis on the rate equations for the gain and the optical field an RF transfer function $H(\Omega)$ for the SOA can be found. This transfer function relates a small modulation at frequency $\Omega$ of the input optical power $\Delta P_{in}(\Omega)$ to the corresponding fluctuations in the output power $\Delta P_{out}(\Omega)$:

$$H(\Omega) = \frac{\Delta P_{out}(\Omega)}{\Delta P_{in}(\Omega)} = e^{G_{DC}} \frac{\Omega_{c2}}{\Omega_{c1}} \frac{i\Omega + \Omega_{c2}}{\Omega_{c2}} \frac{\Omega_{c1}}{i\Omega + \Omega_{c1}} \tag{1}$$

In this $\Omega_{c1} = \frac{e^{G_{DC} \cdot P_{in,DC}}}{E_{sat}} + \frac{1}{\tau_c}$ and $\Omega_{c2} = \frac{P_{in,DC}}{E_{sat}} + \frac{1}{\tau_c}$. The other parameters are the saturated gain $G_{DC}$, the DC input power $P_{in,DC}$, and the SOA/SA saturation energy $E_{sat}$. Note that the expression holds for both a forwardly biased SOA, i.e. $G_{DC} > 0$, and a reversely biased SA, i.e. $G_{DC} < 0$.

Moving on to the experiments, an InP PIC was produced through an MPW run at SMART Photonics [7]. On the PIC, a 200-μm long SOA was placed between two passive waveguides. This structure was probed with lensed fibers at the facets, as depicted in Fig. 1. The interference pattern of the two lasers, which are detuned by $\Omega$, were injected from the west facet through a polarization control (PC), and a voltage-controlled variable attenuator (VA). A 90:10 splitter was placed before the input to monitor the input power at the 10 % drop port.
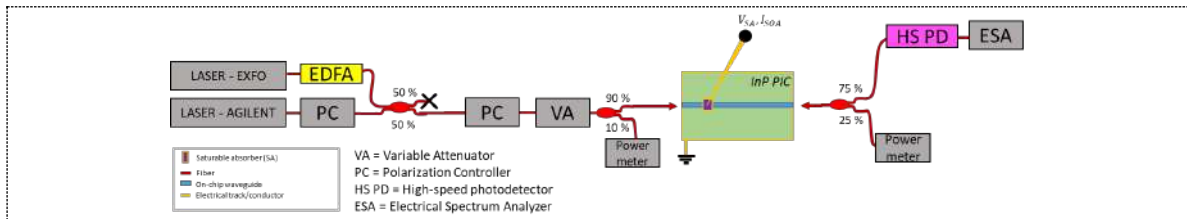


**Figure 1**: The experimental setup.

## 3. Results and discussion

Initially a normalized $H(\Omega)$ was found for a 10-mA forward bias of the SOA, and the results are shown in Fig. 2 for different $P_{in,DC}$. A low frequency resolution for this part was needed, and thus the laser beating was replaced by a single laser and an intensity modulator together with a 6-GHz signal generator. In Fig. 3, a normalized $H(\Omega)$ when a 2-V reverse bias was applied is seen. Here the laser beating setup was utilized. Due to the drift of the beating RF peak, which is a consequence of having two free running lasers, the maximum value and the corresponding frequency was picked from a set of 5 measurements at each data point.

Notice the opposite shapes when comparing Fig. 2 and 3. In the case of a forwardly biased SOA, the transfer function increases to a maximum gain value at high frequencies, whereas the gain decreases, or in other words, the absorption increases to a maximum absorption in the case of an SA. Fits of equation (1) are shown by the solid curves. By extrapolating the two obtained values for $\Omega_2$ to $P_{in,DC} = 0$, the carrier lifetime $\tau_c$ can be extracted. This yields $\tau_c \approx 560$ ps for the forward bias and $\tau_c \approx 26$ ps for the reverse bias. The SOA photocurrent in the case of the 1-V reverse bias voltage was 20 mA @ 33 mW and 25 mA @ 41 mW. This is important, since the extracted $\tau_c$ is an approximation around this point. The well-known space charge effects will induce a dependency between the photocurrent density, and thereby the input power, and $\tau_c$.
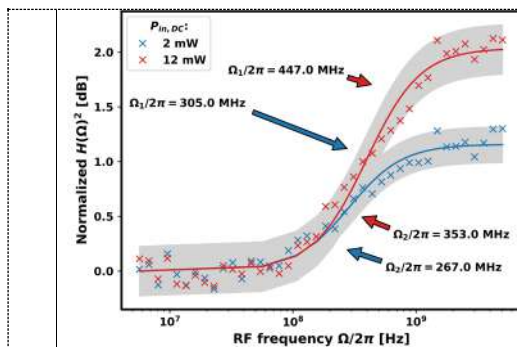


**Figure 2**: Normalized frequency response of the SOA in a 10-mA forward bias. The transfer function values are relative to the value at the lowest frequency.
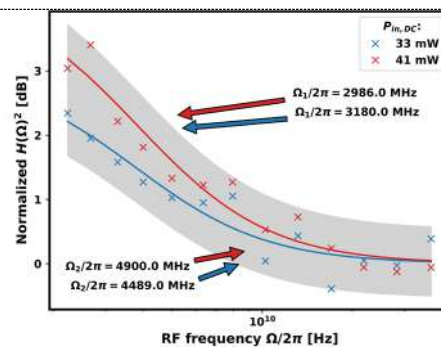
**Figure 3**: Normalized frequency response of the SOA with a 1-V reverse bias. The transfer function values are relative to the value at the highest frequency.

## 4. Conclusion

It has been shown that the carrier lifetime of both an SOA and an SA can be estimated by probing with RF modulated optical signals. In the case of the SA the RF signal was generated by beating two free running lasers, and this all-optical approach enables very high frequencies, above THz, to be generated. Currently an all-optical method with an optical spectrum analyzer on the receiving side is being investigated to overcome the bandwidth limitations that are inherent to an electronics based ESA. Nevertheless, the results of this work show the feasibility of using the beating of two free running lasers on the emitting side for extracting estimates of the carrier lifetime.

## 5. References

[1]  Z. Zhang, H. Li, S. Zhang, and Y. Liu, "Analog-to-digital converters using photonic technology," *Chinese science bulletin*, vol. 59, no. 22, pp. 2666–2671 (2014).

[2]  X. S. Yao, L. Davis, and L. Maleki, "Coupled optoelectronic oscillators for generating both rf signal and optical pulses," *Journal of Lightwave Technology*, vol. 18, no. 1, pp. 73–78 (2000).

[3]  J. Karin, R. Helkey, D. J. Derickson, R. Nagarajan, D. Allin, J. Bowers, and R. Thornton, "Ultrafast dynamics in field-enhanced saturable absorbers," *Applied Physics Letters*, vol. 64, no. 6, pp. 676–678 (1994).

[4]  M. Trajkovic, "High speed electro-absorption modulators in indium phosphide generic integration technologies," *PhD Thesis* (2019).

[5]  K. H. Lee, K. H. Park, and W. Y. Choi, "Measurement of the carrier lifetime and linewidth enhancement factor of semiconductor optical amplifiers using their optical modulation responses." *Optical Engineering* vol. 43, no. 11, pp. 2715-2718 (2004).

[6]  A. Vladimirov and D. Turaev, "A new model for a mode-locked semiconductor laser," *Radiophysics and quantum electronics*, vol. 47, no. 10, pp. 769–776 (2004).

[7]  L. M. Augustin, et al., "InP-based generic foundry platform for photonic integrated circuits," *IEEE Journal of Selected Topics in Quantum Electronics* vol. 24, no. 1, pp. 1-10 (2017).

# Free-space video broadcasting with a packaged, air-cooled, mid-infrared quantum cascade laser

**Pierre Didier,**[1,+] **Olivier Spitz,**[1] **Frédéric Grillot**[1,2]

[1]*LTCI Télécom Paris, Institut Polytechnique de Paris, 19 place Marguerite Perey, Palaiseau, 91120, France*
[2]*Center for High Technology Materials, University of New-Mexico, Albuquerque, NM 87106, USA*
[+]*pierre.didier@telecom-paris.fr*

**Abstract:** In this work, we describe a free-space transmission at mid-infrared wavelength using off-the-shelf quantum cascade laser. The high modulation speed we can achieve with our setup allows us broadcasting a live video with data rate of 270 Mbits/s over a few meters. We also briefly compare the performance of a free-space transmission in the case of a near-infrared laser and this is of paramount interest for our future real-field experiments. Our proof-of-concept, combined with the high output power of quantum cascade lasers, is promising for long-range free-space transmissions that require beam shaping to limit beam wandering.

## 1. Introduction

Free-space communication has long been considered and the mid-infrared domain drew attention in the early efforts, back in the 70ies [1]. The first experiments were based on $CO_2$ lasers but these optical systems remained bulky and expensive, thus hindering the development of such technology. With the development of optical fiber networks, free-space optical systems were long forsook but recent years have seen a renewed interest in domains as varied as LIDAR technology or communication in areas where fiber deployment is expensive or sometimes impossible. Among the optical sources of interest, quantum cascade lasers (QCLs) are highly desirable because on the one hand, QCLs are semiconductor lasers emitting in the mid-infrared domain where the atmosphere is highly transparent [2] and, on the other hand, QCLs are characterized by the absence of relaxation oscillation resonance which is promising for high-speed direct modulation [3]. This experimental work reports on a free-space live video broadcasting with a room-temperature packaged QCL emitting at 4 µm. The video file is encoded in uncompressed 576i format and this corresponds to a data rate of 270 Mbits/s with on-off keying scheme. The modulated optical signal from the QCL is retrieved with a mid-infrared detector three meters away and the resulting electrical signal is sent to a TV monitor where the video can be watched in live. This experimental demonstration paves the way for further free-space studies, such as comparison between near-infrared lasers and mid-infrared lasers when weather conditions degrade.
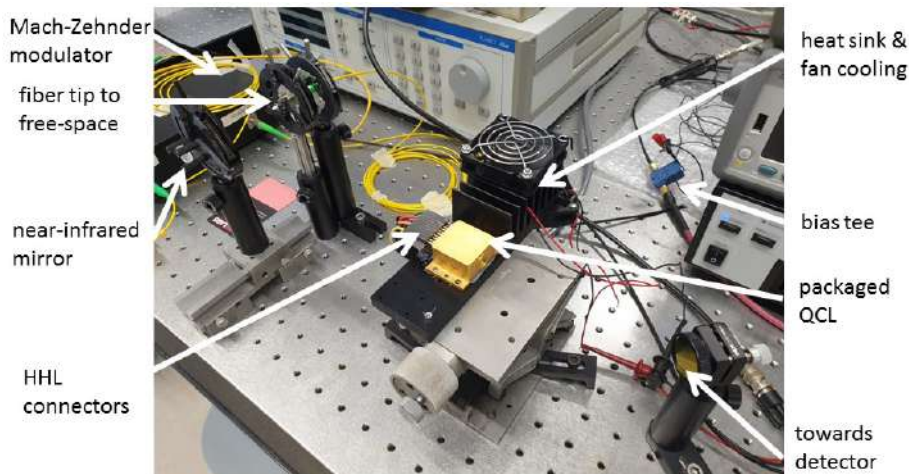
## 2. Experimental setup



Figure 1: Experimental setup for both the mid-infrared free-space communication with QCL and the near-infrared free-space communication with telecom fiber exposed to air. The detectors are not shown in this picture and are placed on another table, 3 meters away.

The Fabry-Perot QCL under study emits up to 125 mW at 20°C and this is suitable for long-range transmission. This condition corresponds to a bias current of 750 mA and a voltage of 16 V. Cooling is achieved with a large heat sink and air cooling, as shown in Fig. 1. The video signal is converted from a 720p HDMI input to a 576i SDI (which is 75 Ohm BNC connector) output with a MD-HX Decimator board. This signal, which is 800 mV peak-to-peak, is attenuated with a 10-dB electrical attenuator before being injected in the AC port of a Pasternack bias tee with 12-GHz bandwidth. The DC port of this bias tee is connected to a low-noise

current source and the combined electrical signal is sent to the HHL connector to bias the QCL. The mid-infrared beam is sent towards a Mecrury-Cadmium-Telluride (MCT) detector with 700 MHz bandwidth and this is suitable for analysis of the 576i signal at 270 Mbits/s. The MCT electrical signal is sent towards an oscilloscope with 500 MHz bandwidth and towards another MD-HX Decimator board to be converted back into HDMI and watched live on a TV screen. For comparison, we also study a free-space transmission at near-infrared wavelength. For this 1550 nm beam, we only have a free-space detector with 13 MHz bandwidth (Thorlabs PDA10CS2) so we cannot analyze an uncompressed video signal. We thus replace the MD-HX Decimator board by an arbitrary waveform generator (AWG) that produces a 15 Mbits/s on-off keying signal. This electrical signal is sent towards a Mach-Zehnder interferometer (MZI – modulation bandwidth of 5 GHz) for signal modulation. Our 1550 nm laser diode with 10 mW optical power is connected to the fiber input of MZI, while the fiber output of MZI is placed behind a free-space lens, as depicted in Fig. 1. In this configuration, the second output of the AWG is connected to the aforementioned bias tee so that we can display mid-infrared and near-infrared signals at 15 Mbits/s simultaneously on the oscilloscope.

## 3. Results and discussion

Figure 2 shows the eye diagrams for the two configurations we mentioned in the previous paragraph. The top left curve is the 576i signal coming from the MD-HX Decimator board at 270 Mbits/s. One can see that the signal is extremely well defined, with no jitter. The signal that is retrieved after transmission at mid-infrared wavelength is the bottom left curve. Because of the limited bandwidth of the packaged QCL [4], the electrical signal coming from the MD-HX Decimator board is degraded and a strong jitter can be seen. However, the transmission remains error-free, as assessed by the open eye, and the retrieved electrical signal can be converted back into a 576i video signal and displayed on a TV screen (not shown here). The right part of Fig. 2 shows the comparison between the mid-infrared transmission (top curve) and the near-infrared transmission (bottom curve), both at 15 Mbits/s. Eye diagrams are wide opened and the conclusion is that the transmission is error-free for both cases. It is relevant to note that the near-infrared signal is a more degraded than the mid-infrared signal, and this comes from the limited bandwidth of the free-space detector. High-speed near-infrared detector should allow us achieving multi-Gbits/s data speed in the future. This communication result is the first step towards the comparison of free-space mid- and near-infrared schemes for long-haul transmission, especially for various conditions of fog or precipitation where the size of the particles influences scattering and attenuation [5].
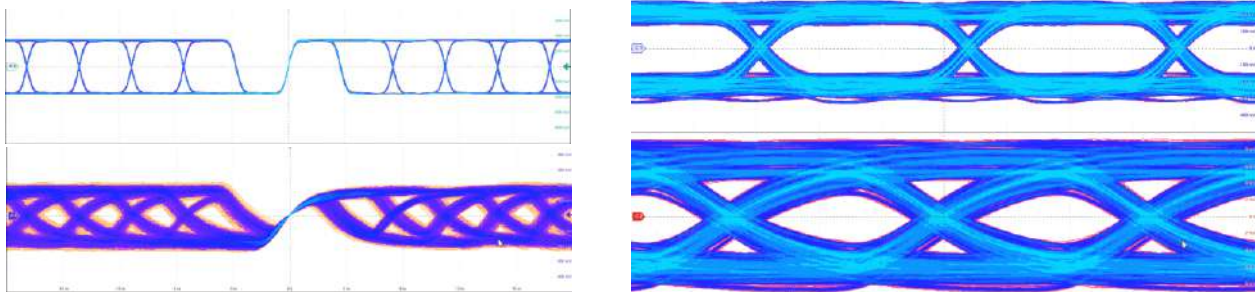


Figure 2: Experimental time traces for a video transmission (left), with the seed signal on top and the received signal on bottom; even if degraded, the received signal can be translated for live video broadcasting. The right traces are for the 15 Mbits/s transmissions at mid (top) and near (bottom) infrared wavelength.

## 5. References

[1] Nussmeier, T., et al., "A 10.6-µm terrestrial communication link," *IEEE Journal of Quantum Electronics* **10**, 230-235 (1974).
[2] Corrigan, P., et al., "Quantum cascade lasers and the Kruse model in free space optical communication," *Optics Express* **17**, 4355-4359 (2009).
[3] Wang, C., et al., "Rate equation analysis of injection-locked quantum cascade lasers," *Journal of Applied Physics* **113**, 063104 (2013).
[4] Spitz, O., et al., "Free-space communication with directly modulated mid-infrared quantum cascade devices," *IEEE Journal of Selected Topics in Quantum Electronics* **28**, 1-9 (2021).
[5] Montmerle-Bonnefois, A., et al., "Adaptive optics pre-compensation of a GEO feeder link: the FEEDELIO experiment," *in Laser Congress: LS&C*, LTh1B.3, Optical Society of America (2019).

## Acknowledgements

# Abstract

## Session IV: Nonlinear Dynamics

# Numerical training of a convolutional neural network for self-mixing interferometry displacement sensing

**Robin Matha[1,2], François Gustave[1] and Stéphane Barland[2]**

[1] *DOTA, ONERA, Université Paris-Saclay, F-91123, Palaiseau, France*

[2] *Université Côte d'Azur – CNRS, Institut de Physique de Nice, 1361 route des Lucioles, F-06560, Valbonne, France*

*robin.matha@onera.fr*

**Abstract:** Self-mixing interferometry is a well-known sensing technique based on optical feedback. Despite the apparent simplicity of the task, recovering the displacement of a target from the interferometric signal through conventional signal analysis is often surprisingly difficult. Recently, a neural network has been shown to provide an excellent trajectory reconstruction provided sufficient training data exists. Generating experimentally this training set is challenging, especially for very broadband displacement. Here we train a neural network with numerically generated data and show that it accurately reconstructs the displacement of a real target from the voltage experimentally measured at the electrodes of a semiconductor laser.

Self-mixing interferometry is based on the interference between the intra-cavity field inside the laser and photons reflected on a longitudinal moving target [1] which changes the internal working point of the laser. This technique has been used to measure small target displacement with sub-wavelength resolution, vibrometry [2-3] or velocimetry [2-3] for example. One can identify two distinct regimes depending on whether the target displacement is much smaller or much bigger than the laser wavelength. In the latter case, the displacement can be reconstructed by counting peaks corresponding to interference maxima, while in the latter phase unwrapping based on physical model fitting is in general used. Here, we place ourselves in the framework of a few wavelengths displacement amplitude, which means that every information in the signal is important to obtain a proper reconstruction of the displacement. Despite the simplicity of the concept, interpreting self-mixing signals can become a complex task considering the signal distortions, caused by fluctuations of the feedback level and/or laser pumping current (see for instance [4]). In the case of a diffusive target, the speckle phenomenon is the main reason for the change of the feedback level as the transverse spatial intensity is a pattern made of dark and bright spots following an exponential distribution. As semiconductor lasers are nonlinear media, any transverse motion or vibration of the target can cause strong fluctuations of the feedback level and modify the resulting interferometric signal shape.

Convolutional neural networks (CNN) are known in machine learning for their ability and efficiency in pattern recognition. The general method for a given CNN architecture, is first to train the network by fitting it with a training dataset, containing both the signal to process and the corresponding true information. During the training stage, the network builds associations between the signal and the truth on the training dataset. When the training is complete the network may be able to process unknown data based on what it learned earlier. Using CNN to reconstruct displacement from self-mixing signal has be done using training set composed by experimental data [5]. When experimental data is not available to build a training set (for instance, Megahertz bandwidth displacement is very hard to produce in a controlled way), numerical simulations [6] could be a good solution to provide a sufficient amount of data.

In this contribution, we will discuss the validity of this approach and present the method and some results obtained using different training sets. Figure 1 shows on top the original displacement (orange) of the target and the prediction of the CNN (blue) after having analysed the self-mixing signal obtained from the original displacement (bottom of the figure) to see how the prediction can be faithful. The self-mixing signal has been obtained experimentally with a laser diode and the prediction has been realised using a CNN trained from a numerical dataset.
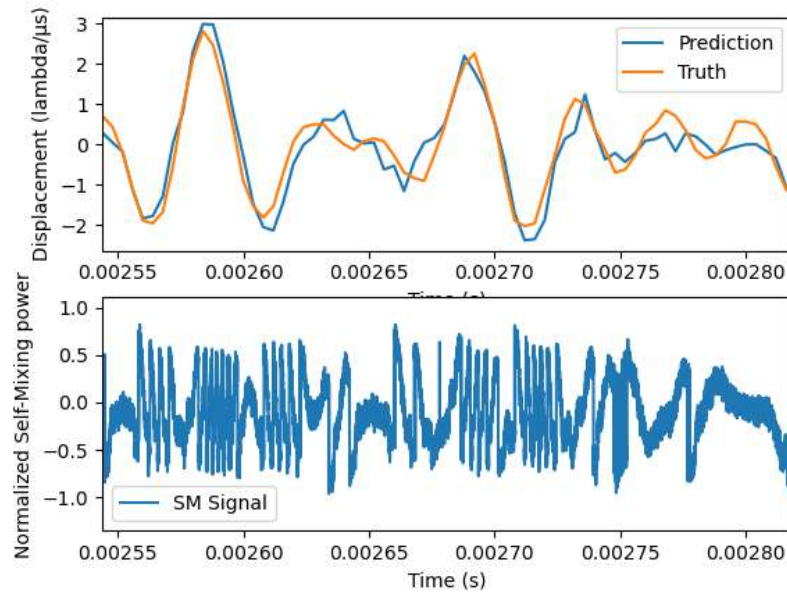
*Figure1: True displacement in orange and CNN prediction in blue (top). Corresponding experimental self-mixing signal measured at the electrodes of the laser diode (bottom).*

We can play on a certain number of parameters to construct these training sets, concerning the displacement traces (amplitudes, frequencies, and waveforms), the laser parameters (pumping ratio, Henry factor), the feedback parameters (feedback level, laser-target distance) and the (artificial) detection noise. We compare experimentally trained and numerically trained CNN predictions thanks to quantitative statistical estimators such as Pearson's correlation and absolute/RMS errors between truth and predicted displacement trajectories.

[1] R. Lang and K. Kobayashi, "External optical feedback effects on semiconductor injection laser properties," in *IEEE Journal of Quantum Electronics*, vol. 16, no. 3, pp. 347-355, March 1980, doi: 10.1109/JQE.1980.1070479.

[2] Jiyang Li, Haisha Niu, Yanxiong Niu, "Laser feedback interferometry and applications: a review", Opt. Eng.56 (5), 050901, 2017

[3] Guido Giuliani *et al, "*Laser diode self-mixing technique for sensing applications"*, J. Opt. A: Pure Appl. Opt.* 4 S283, 2002

[4] Bernal, Olivier D., Usman Zabit, Francis Jayat, and Thierry Bosch. "Toward an Estimation of the Optical Feedback Factor C on the Fly for Displacement Sensing" *Sensors* 21, no. 10: 3528. https://doi.org/10.3390/s21103528, 2021

[5] Stéphane Barland and François Gustave, "Convolutional neural network for self-mixing interferometric displacement sensing," Opt. Express 29, 11433-11444 (2021)

[6] Russell Kliese, Thomas Taimre, A. Ashrif A. Bakar, Yah Leng Lim, Karl Bertling, Milan Nikolić, Julien Perchoux, Thierry Bosch, and Aleksandar D. Rakić, "Solving self-mixing equations for arbitrary feedback levels: a concise algorithm," Appl. Opt. 53, 3723-3736 (2014)

# Dynamics and CW stability of a III-V/Si hybrid laser with a frequency selective mirror

**C. Rimoldi[1]\*, L. L. Columbo[1], J. Bovington[2], S. R. García[3], M. Gioannini[1]**

[1]*Department of Electronics and Telecommunications, Politecnico di Torino, Italy*
[2]*CISCO Systems, San José, CA, USA*
[3]*CISCO Systems, Nuremberg, Germany*
*\*cristina.rimoldi@polito.it*

**Abstract:** We study the dynamics of a tunable hybrid laser based on a III-V Reflective Semiconductor Optical Amplifier (RSOA) and a Silicon Photonic (SiPh) mirror through a model of time-delayed algebraic equations accounting for the mirror frequency selectivity. We address the physical processes that can give rise to instabilities and estimate a stable CW region in terms of reflectivity bandwidth, bias current, and laser detuning, where the system is more likely to maintain single mode emission also in the presence of spurious back-reflections.

## 1 Introduction

In recent years, interest in silicon photonics has grown at a fast pace due to the potential application of this technology towards the realization of low-cost mass-producible optical devices in the telecommunication field, especially optical transceivers. In this context, sensitivity of the developed devices to external optical feedback constitutes an important issue that hinders the realization of stable laser sources and cannot be efficiently resolved through the integration of optical isolators in silicon, as this solution presents a performance that is too low to be considered for the industrial market.
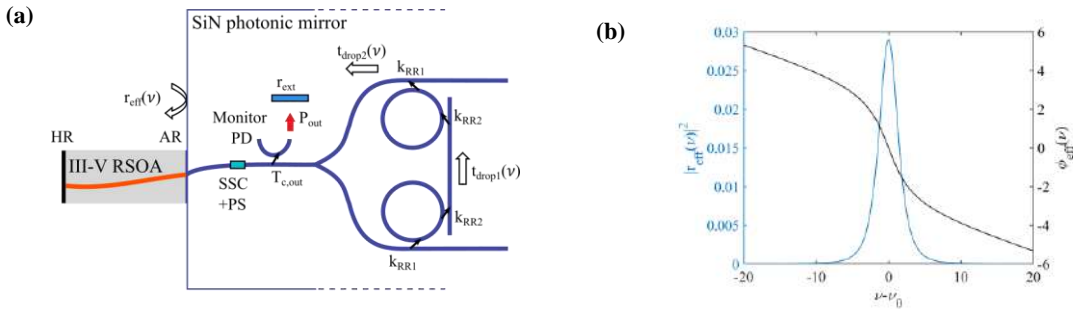


**Figure 1**: **(a)** Setup of the hybrid integrated laser. The output power is extracted through the coupler placed before the splitter. $T_{c,out}$ is the output coupler coefficient, *SSC* is a Spot Size Converter and *PS* is a Phase Section, allowing for the detuning of the lasing mode with respect to the SiPh mirror reflectivity peak. The power coupling coefficients of the two microrings are chosen as $k_{rr1}=k_{rr2}=k_{rr}$ to provide maximum mirror reflectivity in the critical coupling regime. The drop transmission coefficients of the two rings are $t_{drop1}(v)$, $t_{drop2}(v)$ and *Monitor PD* is a monitor photodiode. $r_{ext}$ is an external reflector that accounts for spurious optical feedback at the output port. **(b)** Frequency dependence of the effective reflectivity $r_{eff}(v)$; in this example the FWHM of the reflectivity bandwidth is 3.08 GHz.

In this contribution, we address the stability of a hybrid integrated laser, constituted by a commercial III-V MQW HR/AR RSOA that is edge-coupled to a SiN photonic circuit, as shown in Figure 1(a). Such circuit is based on a mirror loaded by two high-Q microrings, allowing for narrow-band reflectivity through Vernier effect. The ring radii are chosen ($\approx$100 μm) to optimize the tuning range and reduce the overlap between ring resonance peaks adjacent to the lasing one. The current configuration has been previously studied in [1] and has proved to be more robust towards perturbations from spurious back-reflections from the passive parts of the SiPh circuit. With respect to [1], which addressed the system tolerance to optical feedback in the framework of a Lang-Kobayashi model, we here consider a more realistic and rigorous approach accounting for the frequency dependent reflectivity of the SiPh mirror and the competition between longitudinal modes in the hybrid laser cavity, as both effects are relevant when considering a narrow-band reflection and a small FSR. The goal is studying the stability of the CW solution and finding stability regions defined by the detuning of the lasing frequency with respect to the reflectivity peak and the bias current in the RSOA.

## 2. Model description

The considered model consists in a set of time-delayed algebraic equations, combining coupled mode theory, describing the time domain response of the two rings [2], with an evolution equation for the field entering the SiPh circuit, derived from the roundtrip equation [3], and a standard rate equation for the carrier density. The considered form of effective reflectivity accounting for the two rings inside the SiPh circuit is the following

$$r_{eff}(\omega) = \frac{\gamma_{c1}\gamma_{c2}t_{ssc}^2(1 - T_{c,out})}{[\gamma_{t1} + i(\omega - \omega_0)][\gamma_{t2} + i(\omega - \omega_0)]} e^{-i\Delta\phi} e^{-i(\omega-\omega_0)\tau_{eff}}$$

where $\omega_0$ is the carrier reference angular frequency, coincident with a resonance of the active medium cavity, $\gamma_{c1}, \gamma_{c2}, \gamma_{t1}, \gamma_{t2}$ are functions of the ring radii, losses, group velocity, and coupling coefficients and derived from the drop transmission coefficients of the two rings, $\Delta\phi$ is the phase shift deriving from the PS in Figure 1(a), and $\tau_{eff}$ is the time delay introduced by the path within the SiPh circuit. In Figure 1(b) we show $r_{eff}(\nu)$. The effective reflectivity peak is designed to optimize the output power and wall-plug efficiency [1]. Solving the oscillation condition [4], we find the cavity longitudinal modes, each associated to a different threshold carrier density. We focus mainly on the lasing mode at minimal threshold, since it is the one favored for lasing, and we analyze its stability, which can be altered due to four wave mixing, mode hopping, or external optical feedback.

## 3. Results and discussion

The model allows to run efficient dynamical simulations as well as to perform a linear stability analysis (LSA) of the system in the frequency domain [3] for each mode that is solution of the oscillation condition. This analysis correctly predicts the frequency of the pole giving rise to instability and allows us to highlight the physical processes that can contribute to the destabilization of the CW solution. In Figure 2(a), we show a map of the integrated RIN for the free-running laser (i.e., when $r_{ext}$=0) as a function of bias current and detuning ($\Delta\nu$) for different values of effective reflectivity FWHM (designed by the choice of $k_{rr}$) and equal effective lengths of the SiPh mirror. Yellow regions correspond to multimode regimes where the CW solution has become unstable, while blue areas also encompassed by the white dashed line (indicating the border of mode instability according to the LSA) are regions of mode hopping. For a very narrow FWHM (3.08 GHz), the system becomes unstable when the laser relaxation oscillation frequency becomes resonant with the beating between adjacent modes (solutions of the oscillation condition). On the other hand, for larger FWHMs ($\geq$ 6.17 GHz), instability is due to competition between longitudinal modes, triggering photon-photon resonance. Further, the stable region is always asymmetric with respect to $\Delta\nu = 0$, with the larger stable area observed for negative detuning, which can be associated to a phenomenon of negative feedback [5]. We are therefore able to find a trade-off region between the two effects that optimizes the frequency range of stable CW operation in terms of bias current and effective reflectivity FWHM (see Figure 2(b)). The stability of these parametric regions has been tested also in presence of optical feedback ($r_{ext} \neq 0$), allowing to find an optimal value of detuning more robust against spurious back-reflections.
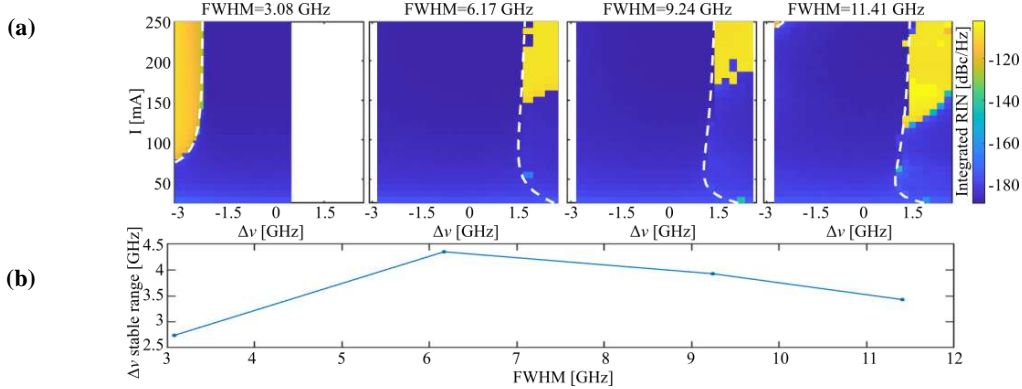


**Figure 2**: **(a)** Maps of integrated RIN versus $\Delta\nu$ and SOA bias current obtained from simulations of the solitary hybrid laser for 4 different FWHM of effective reflectivity $r_{eff}(\omega)$. When the integrated RIN is high (yellow regions) the CW emission is unstable. The blue region also encompassed by the white dashed line (resulting from the LSA) for FWHM $\geq$ 6.17 GHz is a region of mode hopping where the integrated RIN remains low but single mode emission has already shifted to another mode. Note that in order to make the maps comparable we needed to extend in (a) the range of the x-axis to frequencies beyond the detuning values that are solutions of the oscillation condition (white regions). **(b)** Maximum range of detuning $\Delta\nu$ where the system is stable for any bias current for lasers having different FWHM of $r_{eff}(\omega)$.

## 4. Conclusion

This study provides relevant information regarding the design of stable hybrid lasers, setting the basis for an easier integration of SiPh optical transceivers without the need for bulky and often low-performance optical isolators.

## 5. References

[1]     L. Columbo, et al., IEEE J. Sel. Top. Quantum Electron., vol. 26, no. 2, pp. 1–10, 2020.
[2]     L. Chrostowski and M. Hochberg, Silicon Photonics Design. Cambridge: Cambridge University Press, 2015.
[3]     E. Detoma, et al., IEEE J. Quantum Electron., vol. 41, no. 2, pp. 171–182, 2005.
[4]     B. Tromborg, et al., IEEE J. Quantum Electron., vol. 23, no. 11, pp. 1875–1889, 1987.
[5]      M. A. Tran, et al., APL Photonics, vol. 4, no. 11, p. 111101, 2019.

# Effect of the filtered feedback on the memory capacity in a photonic reservoir computer

**G. O. Danilenko,[1] A. V. Kovalev,[1*] A. Locquet,[2,3] D. Rontani,[4] and E. A. Viktorov[1]**

[1]*ITMO University, 199034 Saint Petersburg, Russia*
[2]*Georgia Tech-CNRS IRL 2958, Georgia Tech Lorraine, F-57070 Metz, France*
[3]*School of Electrical and Computer Engineering, Georgia Institute of Technology, Atlanta, Georgia 30332, USA*
[4] *Chair in Photonics, LMOPS EA 4423 Laboratory, CentraleSupélec & Université de Lorraine, F-57070 Metz, France*
*\*avkovalev@niuitmo.ru*

**Abstract:** We study the performance of a photonic reservoir computer based on a semiconductor laser with high- and low-pass filtered optoelectronic feedback. We find that the decrease of the low-pass filter cut-off frequency while limiting the system's bandwidth increases the system's memory capacity. We analyze the eigenvalue spectrum of the system and find the correlation between the distance from the imaginary axis to the nearest eigenvalue and the memory capacity of the reservoir computer.

## 1 Introduction

Reservoir computing (RC) is the data processing paradigm based on a complex response of the dynamical system (called the reservoir) to the input signal perturbation. This response depends on the input signal and the previous states of the reservoir. Thus the RC system possesses fading memory similar to classical recurrent neural networks. The advantage of RC is the simplicity of the system training performed by adjusting only the output layer of the system. In this work, we study the performance of a photonic RC system based on a semiconductor laser with high- and low-pass filtered optoelectronic feedback. The system's architecture and operation principle are similar to that reported previously [1], with an additional low-pass filter inserted in the feedback loop. Here we investigate the influence of this filter on the reservoir computer memory properties.

## 2. Model description

A coupled delay differential equation model describes the RC system:

$$\dot{I}(t) = 2N_g(t)I(t) \tag{1}$$

$$\dot{I}_{FH}(t) = -\tau_H{}^{-1}I_{FH}(t) + 2N_g(t)I(t) \tag{2}$$

$$\dot{I}_{FL}(t) = \tau_L{}^{-1}\big(I_{FH}(t) - I_{FL}(t)\big) \tag{3}$$

$$\varepsilon^{-1}\dot{N}_g(t) = P(t) + \eta I_{FL}(t-\tau) - N_g(t) - \big(1 - 2N_g(t)\big)I(t) \tag{4}$$

where $I(t)$ – the normalized intensity of the laser field; $N_g(t)$ – the carrier density; $I_{FH}(t)$ - the filtered intensity signal after the high pass filter; $I_{FL}(t)$ – the filtered intensity signal after the low pass filter; $P(t)$ – the pump parameter; $\varepsilon$ – the ratio of the photon and carrier lifetimes; $\eta$ – the feedback strength; $\tau_H$ – the inverse of the cut-off frequency of the high pass filter; $\tau_L$ - the inverse of the cut-off frequency of the low pass filter; $\tau$ – the feedback delay time. The input data is masked and entered by the pump current modulation (see [1] for the details) according to the function

$$P(t) = P(1 + \xi \cdot M(t)), \tag{5}$$

where $P$ – the constant value of the pump parameter, $\xi$ – the modulation strength, $M(t)$ – a modulation function formed according to the input data multiplied by mask.

The RC system based on feedback architecture relies on the time-delay RC (TDRC) approach: A single physical nonlinear node is used in conjunction with virtual nodes distributed in the delayed feedback loop. The laser intensity of virtual nodes is taken after each time period having the duration $dt$:

$$dt = \frac{\tau}{N}, \tag{6}$$

Therefore, the output layer reads the virtual nodes' signals at defined time points that differ by a time period $dt$. The number of mask elements in the considered system equals the virtual nodes' number to simplify numerical modeling.
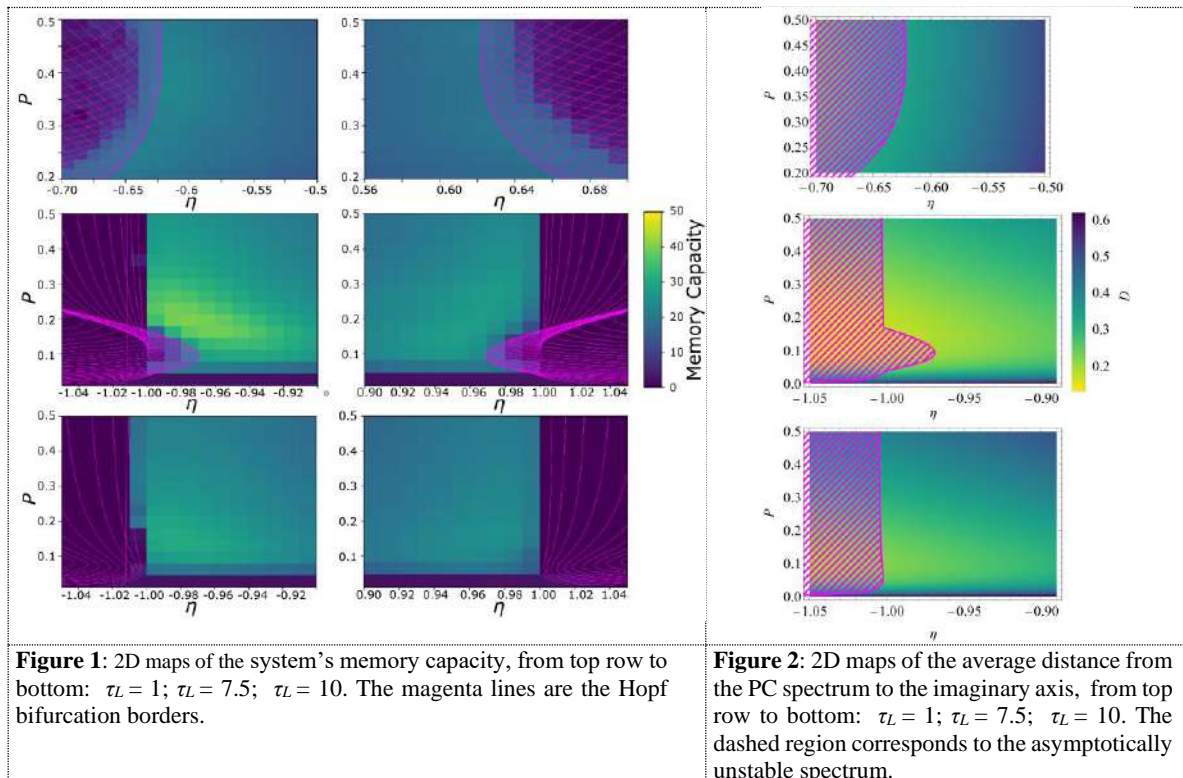
The reservoir's memory capacity is calculated as:

$$\text{MC} = \sum_{m=1}^{\infty} \frac{cov^2(O_i, S_{i-m})}{\sigma^2(O_i)\sigma^2(S_i)} \tag{7}$$

where $\sigma^2$ – the variance, cov – the covariance, $O_i$ -the output signal, $S_{i-m}$ – the input signal delayed by *m* time-steps.

We consider the following set of parameters for further numerical analysis: $\varepsilon = 0.1$; $\tau_H = 2000$; $\tau = 1000$; $N = 48$; $\xi = 0.1$. Time parameters are measured in the units of the photon lifetime $t_p = 100$ ps.

## 3. Results and discussion

Figure 1 shows the 2D maps of the system's memory capacity for the different values of the low-pass filter cut-off parameter along with the Hopf bifurcation borders. With the decrease of the cut-off frequency, we see that the memory capacity increases, with maximum values observed in the vicinity of the Hopf bifurcation border. The 2D maps are asymmetric with respect to the feedback sign (as in [1]). As noticed in [2], the memory capacity is maximized when many of the system's eigenvalues have real parts close to zero. To further investigate the correlation between the spectral properties of the reservoir and the memory capacity, we performed the pseudo-continuous (PC) approximation of the eigenvalue spectrum under the assumption of the long delay. While the PC spectrum is symmetric in relation to the feedback sign and cannot explain the asymmetry, we found that the mean distance between the PC spectrum and the imaginary axis is well-correlated to the memory capacity (see Fig. 2). This mean distance characterizes both proximity of the spectrum to the axis and its flatness, thus quantifying the reservoir's effective excursion in phase space.



**Figure 1**: 2D maps of the system's memory capacity, from top row to bottom: $\tau_L = 1$; $\tau_L = 7.5$; $\tau_L = 10$. The magenta lines are the Hopf bifurcation borders.

**Figure 2**: 2D maps of the average distance from the PC spectrum to the imaginary axis, from top row to bottom: $\tau_L = 1$; $\tau_L = 7.5$; $\tau_L = 10$. The dashed region corresponds to the asymptotically unstable spectrum.

## 4. Conclusion

We found that decreasing the low-pass filter cut-off frequency while limiting the bandwidth increases the memory capacity of an optoelectronic feedback RC. We suggest this results from a flatter eigenvalue spectrum increasing the transient excursion of the reservoir in phase space. Furthermore, the connection between the feedback filtering properties and the spectrum provides new insight for optimizing the reservoir's memory properties.

## 5. References

[1]     P. S. Dmitriev, A. V. Kovalev, A. Locquet, D. Rontani, and E. A. Viktorov, "Asymmetrical performance of a laser-based reservoir computer with optoelectronic feedback," *Optics Letters*, vol. 45, no. 22, pp. 6150-6153 (2020).

[2]     F. Köster, S. Yanchuk and K. Lüdge, "Insight into delay based reservoir computing via eigenvalue analysis," *Journal of Physics: Photonics*, vol. 3, no. 2, p. 024011 (2021).

# Dual-section passively mode-locked quantum-dot laser with continuous-wave optical injection

**A. F. Ribeiro\*, A. F. Forrest, and M. A. Cataluna**

*Institute of Photonics and Quantum Sciences, Heriot-Watt University, Edinburgh EH14 4AS, United Kingdom*
*\*afr3@hw.ac.uk*

**Abstract:** A study on continuous-wave optical injection of a dual-section passively mode-locked quantum-dot laser has revealed the existence of three distinct pulsing regimes: locked Q-switching, locked multiple pulsing, and locked mode-locking. A few results on the locked Q-switching regime are reported with pure Q-switching behaviour shown for the first time in an optically injected quantum-dot laser. The three pulsing regimes have been explored and compared with the free-running laser and more results will be presented in the conference.

## 1. Introduction

Optical injection of passively mode-locked quantum-dot (QD) lasers through external or self-feedback experiments has been shown to significantly improve the timing jitter of the laser pulses [1], as well as reduce the time-bandwidth product (TBP) and optical mode linewidth, and provide repetition rate tunability, in the case of dual-tone injection [2]. While most reports on optical injection focus on the characterization of the QD laser when locked and mode-locked, stating the benefits and intricacies of this method, previous studies of QD lasers under continuous-wave (CW) optical injection have theoretically predicted the possibility of obtaining additional and different locked regimes, such as Q-switching and double-pulsing, dependent on the operational conditions of the injected laser [3]. In this paper, we demonstrate experimentally a locked Q-switching regime with pure Q-switching behaviour, with a repetition rate (~1GHz) which could be tuned with injection power by up to tens of MHz.

## 2. Experimental setup

The device under study is a two-section QD laser, with an active region composed of 10 layers of InAs/GaAS QD, grown and fabricated by Innolume (GmbH). The total laser length is 8 mm, incorporating a 900-μm long saturable absorber. When passively mode-locked, under a range of gain current ($I_{gain}$) and absorber voltage ($V_{abs}$) values, the QD laser outputs 1260 nm light pulses with few picoseconds duration and at a repetition rate of approximately 5.06 GHz. To perform the optical injection, the output of a tunable narrow-linewidth commercial CW laser was injected into the gain section of the laser as seen in Fig.1.
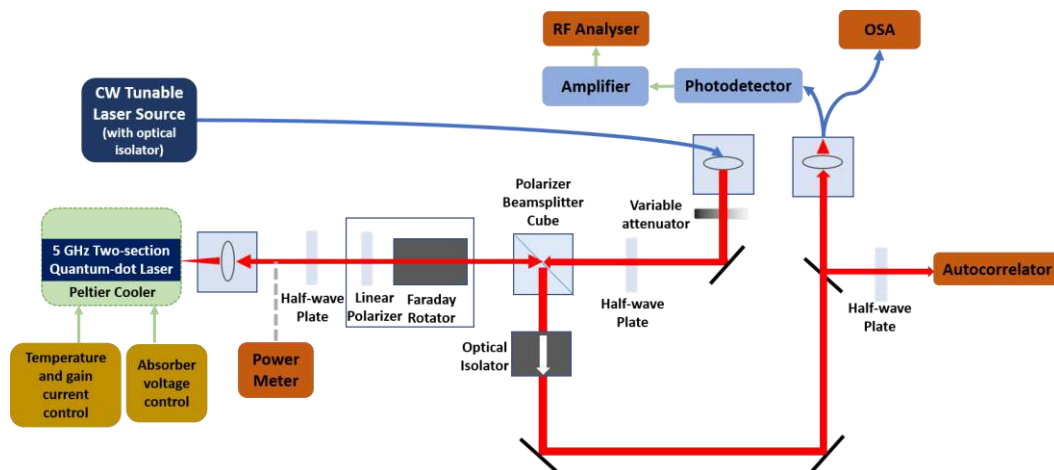


**Figure 1**: Schematic representation of the CW optical injection setup. (OSA: Optical Spectrum Analyser)

Injection locking was performed by tuning the CW laser in picometer wavelength steps to match one of the optical modes of the free-running QD laser, which are equally distanced at approximately 27 pm, considering a 5.06 GHz repetition rate. The QD laser was considered locked to the CW laser when there were no visible beating notes (between the CW laser and the adjacent QD laser optical modes) in the (radio-frequency) RF spectrum. The output of the QD laser, when free-running or injection-locked, was measured using an optical spectrum analyser, an electrical spectrum analyser, a commercial autocorrelator (A.P.E. pulseCheck NX), and a power meter.

## 3. Results and discussion

The free-running mode-locked QD laser ($I_{gain}$ = 190 mA, $V_{abs}$ = 6.8V), was injected at an injection wavelength ($\lambda_{inj}$) within the limits of the free-running optical spectrum at these bias conditions. Q-switching operation begins when the CW laser locks to one of the optical modes of the QD laser.

Fig. 2(a) shows the RF spectra of the free-running and injection-locked laser, revealing the appearance of a low-frequency (930 MHz) peak, characteristic of a Q-switching regime and the suppression of the 5 GHz mode-locking repetition rate. An evaluation of the RF spectrum of the injection locked laser over a 26 GHz span (not depicted here) shows no other significant RF peaks, which gives an indication of pure Q-switching behaviour. Fig. 2(b) shows the influence of the injection power on the Q-switching regime, while keeping the injection wavelength ($\lambda_{inj}$) constant.
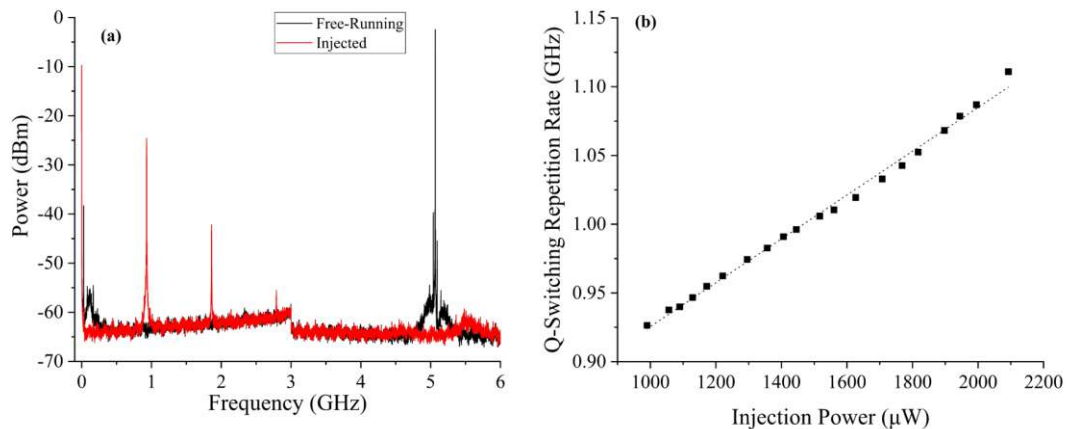


**Figure 2**: [$I_{gain}$ = 190 mA, $V_{abs}$ = 6.8V]: (a) RF spectrum of free-running (Black) and locked Q-switched QD laser (Red), (b) Q-switching repetition rate of locked Q-switched QD laser in terms of injection power ($P_{inj}$). The dashed black line corresponds to a linear fit of the Q-switching repetition rate vs injection power.

As shown in Fig. 2 the Q-switching repetition rate increases with injection power in a linear trend with a slope of approximately 0.16 GHz/mW, comparable to previous reports of increasing Q-switching repetition rate with gain current in free-running QD lasers [4]. These results suggest that there may be a connection between the effect of gain current in a free-running Q-switched QD laser and the effect of injection power in a locked Q-switched QD laser. In this locked Q-switching regime, it was also possible to tune the wavelength of the slave laser by around 7 nm (not shown here). The effect of gain current ($I_{gain}$) and absorber voltage ($V_{abs}$) on the Q-switching repetition rate of the locked Q-switching regime were also studied and will be presented at the conference.

Moreover, two additional regimes were also observed: locked mode-locking and locked multiple pulsing (exhibiting either double or triple pulsing) – further details will also be discussed during the presentation of this paper.

Overall, these findings suggest that optical injection increases the versatility and usability of the QD laser and could have implications on the understanding of the complex dynamics of the optical injection process of QD lasers.

## 5. References

[1]     L. Drzewietzki, S. Breuer, and W. Elsäßer, "Timing jitter reduction of passively mode-locked semiconductor lasers by self-and external-injection: Numerical description and experiments," Opt. Express **21**(13), 16142-16161 (2013).

[2]     T. Habruseva, G. Huyet, and S. P. Hegarty, "Dynamics of quantum-dot mode-locked lasers with optical injection," IEEE J. Sel. Top. Quant. **17**(5), 1272-1279 (2011).

[3]     N. Rebrova, G. Huyet, D. Rachinskii, and A. G. Vladimirov, "Optically injected mode-locked laser," Phys. Rev. E **83**(6), 066202 (2011).

[4]     A. G. Vladimirov, U. Bandelow, G. Fiol, D. Arsenijević, M. Kleinert, D. Bimberg, A. Pimenov, and D. Rachinskii, "Dynamical regimes in a monolithic passively mode-locked quantum dot laser," J. Opt. Soc. Am. B, **27**(10), 2102-2109 (2010).

# Bound Pulse States in a Multiple-Quantum-Well Laser Subject to Delayed Optoelectronic Feedback

**Md Shariful Islam[1, 2, *], A.V. Kovalev[3], E. A. Viktorov[3], A. Locquet[1, 2], and D. S. Citrin[1, 2]**

[1]*Georgia Tech-CNRS UMI 2958, Georgia Tech Lorraine, 2 Rue Marconi, 57070 Metz, France*
[2]*School of Electrical and Computer Engineering, Georgia Institute of Technology, Atlanta, Georgia 30332-0250, USA*
[3]*ITMO University, Birzhevaya Liniya 14, 199034 Saint Petersburg, Russia*
*\*Email: mdshariful.islam@gatech.edu*

**Abstract:** Positive time-delayed optoelectronic feedback in a multiple-quantum-well semiconductor laser diode is found to produce pulsing at loop-delay repetition rate for injection current slightly below threshold following a subcritical Hopf bifurcation. Double-pulsing, clustering, and intermittent states are reported to appear at higher injection currents confirming the presence of a bound state. In summary, the experimental observations confirm the existence of three distinct regimes in the laser dynamics with delayed optoelectronic feedback; two are dominated by either the external loop characteristics or by the field-matter coupling of the laser itself, while the third regime demonstrates various mixed-mode dynamics.

## 1. Introduction

Broadly speaking, the self-pulsing behavior of laser diodes (LD) with OEF has been widely investigated [1-4]. In particular, the pulse-train repetition (rep) rate has been observed to be a subharmonic of the relaxation-oscillation frequency $f_{RO}$ [2,3] or, under specific conditions, at frequency $f_\tau = \tau^{-1}$ with $\tau$ the loop delay [1] as well. The intermittent timescale of the erratic dynamics between the previous two regions is reported to originate from the high-pass filters in the electronic loop in [5]. Dynamical behaviors have been mainly studied for restricted ranges of injection current $J$, specifically $\sim 1.4 J_{th}$ to $\sim 1.6 J_{th}$, for which the rep rate depends primarily on the internal construction of the laser [2-4]. A chaotic spiking from an incomplete homoclinic scenario to a saddle-focus appears between a steady-state and a periodic self-oscillation with respect to the injection current, and it is further explored in terms of feedback strength and cutoff frequency in Ref. [5]. Nevertheless, the generation of pulsed structures in lasers usually results from a balance between nonlinear dispersion and diffraction effects, as has been multiply demonstrated for the variety of mode-locked pulses. In this work, we experimentally demonstrate the existence of pulse multiplets in a LD configuration formed by positive optoelectronic (OE) feedback (OEF).

## 2. Experiment

A single-mode DFB multi-quantum-well (MQW) InGaAsP LD (3SP Technologies-1953LCV1) with a threshold current ($J_{th}$) of 20 mA is used for this experiment (see Fig. 1). The feedback loop is composed of an optical and an electronic path, creating a total delay of 32.9 ns. The electronic path, consisting of a photodetector, amplifiers, and a bias tee, has an approximately flat transfer function from 10 MHz to 12 GHz. Pump current $J$ of the LD is self-modulated with a feedback signal injected through the bias tee



**Figure 1**: The experimental setup.

(BT). The optical isolator (OI) is inserted to prevent any back reflection to the LD. The feedback originates from the photodetector (PD), which is amplified in the amplifier cascade (Amps) and attenuators (Atten) before feeding it to the radio frequency input arm of the BT. An oscilloscope measures the optical intensity after the PD.
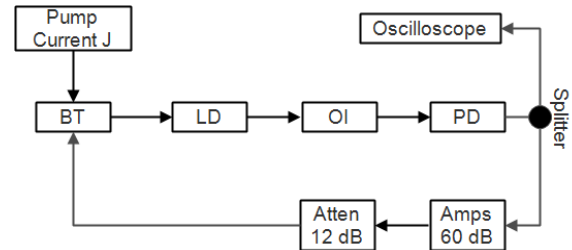
## 3. Results and discussion

A sparsely investigated region is found while operating in the range $J_{th} \pm 1.2 J_{th}$ and was reported to produce pulsing at rep rate $f_\tau$ [1]. Interestingly, this region with $f_\tau$ as pulse rep rate was discussed by merely presenting it as a bootstrap loop, and the more popular models for analyzing similar time-delayed systems, such as the rate equations model, fail to predict this state [1]. In revisiting a similar experimental setup, we have found that there is a gradual transition from $f_\tau$ to $f_{RO}$ pulsing, which is led by a steady formation of clustering around the delay time. This experimental observation confirms the existence of three distinct regimes in the LD dynamics with delayed optoelectronic feedback; two are dominated by either the external loop characteristics or by the

field-matter coupling of the laser itself, while the third regime demonstrates various mixed-mode dynamics (see Fig. 2).
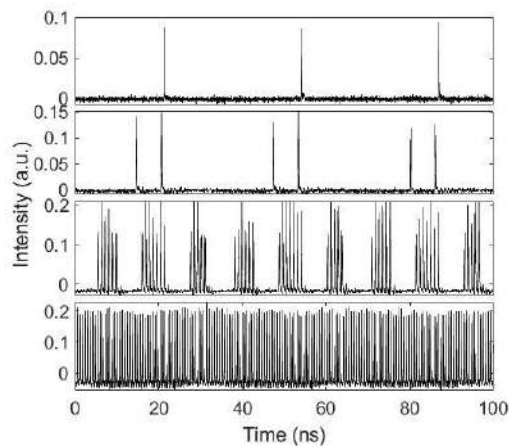


**Figure 2**: Experimental time series of the laser intensity in a range of pump currents. Loop delay $\tau$ = 32.9 ns. From top to bottom subfigure, $J$ = 18.50 mA, 18.80 mA, 23 mA, and 34 mA.
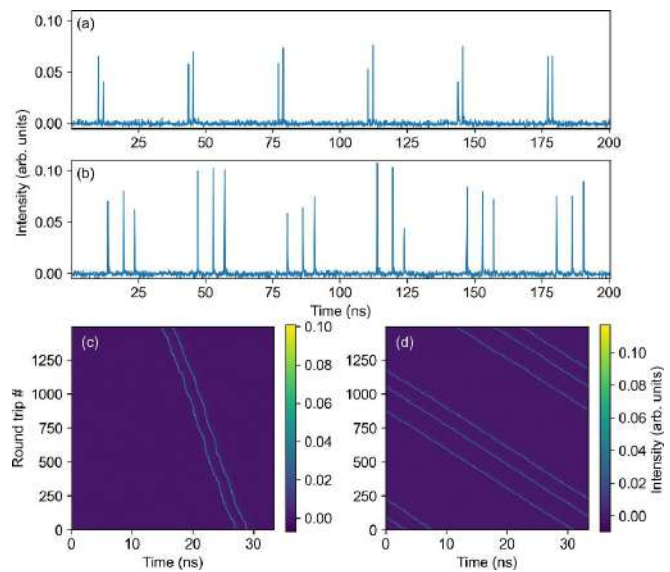


**Figure 3:** (a, b) Intensity time series of the doublets and triplets at 17.84 mA and 19.9 mA, respectively. (c, d) The corresponding two-dimensional representations of the time series evolution per feedback loop delay.

CW operation in OEF LD is usually destabilized by the Hopf bifurcation at either $f_\tau$ or $f_{RO}$. In the LD threshold's vicinity, the bifurcation becomes subcritical, making the folded bifurcation structure similar to the passively mode-locked laser configuration described in [6]. We experimentally demonstrate the folding phenomenon, which leads to the generation of various multiplets demonstrated in Fig. 3.

## 4. Conclusion

The near-threshold dynamics of a MQW LD is investigated, and various bound pulsing states are demonstrated. Under a positive OEF, the system displays several mixed-mode dynamics which are of interest to understand a sparsely explored area of the LD nonlinearity.

## 5. References

[1] T. C. Damen and M. A. Duguay, "Optoelectronic regenerative pulser," *Electron. Lett.* **16**(5), 166–167 (1980).

[2] S. Tang and J. M. Liu, "Chaotic pulsing and quasi-periodic route to chaos in a semiconductor laser with delayed opto-electronic feedback," *IEEE J. Quant. Elect.* **37**(3), 329–336 (2001).

[3] F. Y. Lin and J. M. Liu, "Nonlinear dynamics of a semiconductor laser with delayed negative optoelectronic feedback," *IEEE J. Quant. Elect.* **39**(4), 562–568 (2003).

[4] F. Y. Lin and J. M. Liu, "Harmonic frequency locking in a semiconductor laser with delayed negative optoelectronic feedback," *Appl. Phys. Lett.* **81**(17), 3128–3130 (2003).

[5] K. Al-Naimee, F. Marino, M. Ciszak, R. Meucci, and F. T. Arecchi, "Chaotic spiking and incomplete homoclinic scenarios in semiconductor lasers with optoelectronic feedback," *New J. Phys.* **11**, 073022 (2009).

[6] M. Marconi, J. Javaloyes, S. Balle, and M. Giudici, "How lasing localized structures evolve out of passive mode locking," *Phys. Rev. Lett.* **112**, 223901 (2014).

# Abstract

## Session V: Innovative Light Emitting Structures & Applications

# Narrow-linewidth semiconductor Fano laser

**Y. Yu,[1,2]\* A. Sakanas,[1,2] A. R. Zali,[1,2] E. Semenova,[1,2] K. Yvind,[1,2] and J. Mørk[1,2]\***

*[1]DTU Fotonik, Technical University of Denmark, Lyngby, Denmark*
*[2]NanoPhoton – Center for Nanophotonics, Technical University of Denmark, Lyngby, Denmark*
*[\*yiyu@fotonik.dtu.dk](), [jesm@fotonik.dtu.dk]()*

**Abstract:** We show that a bound-state-in-the-continuum induced by an optical Fano resonance can be used to improve the coherence of a laser, leading to an experimental demonstration of a microscopic laser with a linewidth more than 20 times smaller than existing microscopic lasers.

## 1. Introduction

Since Schawlow and Townes [1], it is known that the coherence of a laser is limited by quantum fluctuations, with the laser linewidth $\Delta v$ scaling inversely with the quality factor, $Q$, and the laser power, $P$, $\Delta v \propto 1/(PQ^2)$ [1]. This means that one can reduce the laser linewidth by increasing the power or by improving $Q$, e.g., by enlarging the laser system's size or engineering the spatial profile of the lasing mode, as exemplified by various macroscopic lasers [2]. However, as the laser shrinks into the microscopic regime [3]-[5], quantum fluctuations, and therefore the linewidth, increase substantially due to the reduction of photon number in the laser cavity. Thus, despite considerable progress in microscale and nanoscale lasers, their coherence length remains very limited.

## 2. Experiment

Here, we use a bound-state-in-the-continuum (BIC) to address this long-standing problem [6]. We consider a BIC induced by Fano interference [7] between the mode continuum of a terminated waveguide (WG) and the discrete mode of a side-coupled nanocavity (realized by an InP photonic crystal on a silicon platform) (Fig. 1(a)) [8]. If the nanocavity is intrinsically lossless, the Fano mirror reflectivity can reach unity, thus, a BIC is formed and localized in the nanocavity and a virtual cavity region between the left end of the WG and the right Fano mirror. In reality, the nanocavity always has a finite loss, turning the BIC into a quasi-BIC (Fano BIC). We can identify the BIC nature of the Fano mode by a sensitive dependence of the Q-factor on the structural parameters (purple curve in Fig. 1(b)). In comparison, ordinary laser modes can adjust their wavelength to fulfill the phase-matching condition, and the Q-factor only changes slowly with the parameter (black curve in Fig. 1(b)). At the BIC wavelength, the Fano BIC mode exhibits a highly non-uniform light distribution (Fig. 1(c)), leading to an optical field intensity much higher in the nanocavity than in the WG. Such a spatial asymmetry of the Fano BIC can be harnessed by incorporating active material only in the continuum region (embedding a buried heterostructure containing a single quantum well in the WG region). Photons generated in the active region thus get stored predominantly in the passive region, which features a much smaller loss. Therefore, compared to ordinary modes, the Q-factor of the Fano BIC can be much higher.
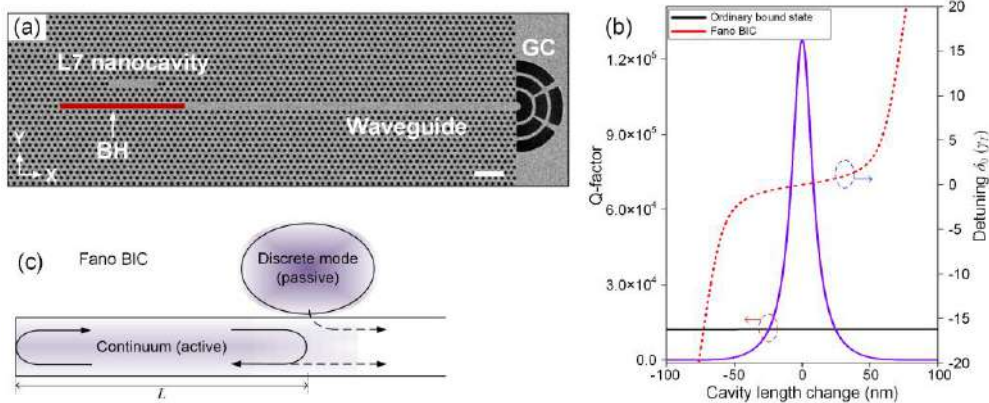


**Figure 1**: (a) Scanning electron microscope (SEM) image of a Fano BIC laser based on InP photonic crystal (PhC) with a buried heterostructure (BH, red rectangle) gain region and a grating coupler (GC). The scale bar corresponds to 2 μm. (b) Example of calculated Q-factor versus cavity length $L$ for the Fano BIC laser (solid purple line) and a conventional Fabry-Pérot laser (solid black line). The red dashed line depicts the calculated variation of the detuning $\delta_0$ of the Fano BIC laser frequency from the nanocavity resonance. (c) Optical BIC formed in the Fano laser where photons are generated in the active region, a continuum of modes, but are predominantly stored in the low-loss passive region [8].

We derive the linewidth of the Fano BIC laser above the threshold using a Langevin approach

$$\Delta v_{FL} = \frac{1}{2\pi} \frac{1+\alpha^2}{\left(1+\gamma_{in}/\gamma_T\right)^2} \frac{G_{s,FL}n_{sp}}{2I_{FL}} \; . \tag{1}$$

Here, $\alpha$ is the linewidth enhancement factor, $G_{s,FL}$ is the threshold modal gain, $n_{sp}$ is the population inversion factor, $I_{FL}$ is the number of photons in the Fano cavity, $\gamma_{in}$ and $\gamma_T$ are the inverse roundtrip time in the Fano cavity, and the total loss rate of the nanocavity, respectively. It can be seen how the linewidth of the laser can be decreased by increasing the lifetime of the discrete mode. In contrast to the spatial mode profile engineering approach, the optical confinement factor for the Fano BIC laser is fixed so the reduction of the linewidth does not compromise the laser threshold. Compared to external cavity lasers, which are macroscopic and suffering from multi-mode effects that require external filtering and careful alignment [2], the Fano BIC laser does not have these trade-offs and can be scaled into the microscopic regime.

### 3. Results and discussion
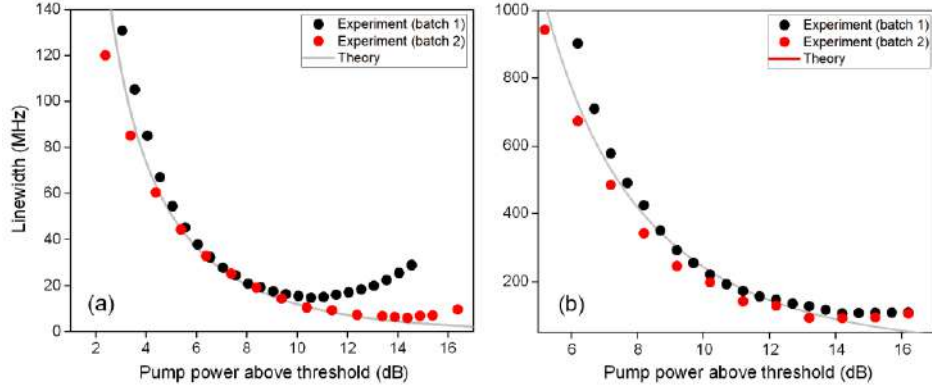


**Figure 2**: Measured linewidths of (a) the Fano BIC laser and (b) the Fabry-Pérot laser versus pump power, which has been normalized to the threshold pump power. The black and red dots are experimental results, and the solid gray lines are theoretical calculations.

We measured the laser linewidth using a self-homodyne technique. The measurements agree well with our theory (Eq. (2)). The linewidth first decreases with pump power and then saturates and increases for high pump powers, which is a general phenomenon seen for many lasers [3]. In all cases, the coherence for Fano BIC lasers is much higher than the Fabry-Pérot laser counterparts. The Fano laser shows the smallest linewidth of 5.8 MHz, more than 20 times smaller than previously reported for microscopic lasers [3]. In our current case, a relatively low $Q_c$ and large $L$ were chosen to relax fabrication constraints. However, as $L$ decreases and $Q_c$ increases, we found the linewidth improvement factor can reach $10^3$. This implies that the Fano BIC laser becomes increasingly advantageous as laser sizes shrink further into the nanoscale.

### 4. Conclusion

A new approach for reducing the linewidth of a laser was proposed and demonstrated, which relies on a bound state in the continuum induced by a Fano resonance and allows reducing the linewidth of a microscopic laser by several orders of magnitude. The findings are general for the class of Fabry-Pérot type BIC [6] and can be extended in heterogeneous or hybrid integration platforms and structures with smaller footprints.

### 5. References

[1]   A. L. Schawlow and C. H. Townes, "Infrared and optical masers," Physical Review 112, 1940 (1985).
[2]   J. Mørk, et al., "Chaos in semiconductor lasers with optical feedback: theory and experiment," IEEE Journal of Quantum Electronics 28, 93–108 (1992).
[3]   J. Kim, et al., "Narrow linewidth operation of buried-heterostructure photonic crystal nanolaser," Optics Express 20, 11643–11651 (2012).
[4]   M. Khajavikhan, et al., "Thresholdless nanoscale coaxial lasers," Nature 482, 204–207 (2012).
[5]   R. F. Oulton, et al., "Plasmon lasers at deep subwavelength scale," Nature 461, 629–632 (2009).
[6]   C. W. Hsu, et al., "Bound states in the continuum," Nature Reviews Materials 1, 16048 (2016).
[7]   Y. Yu, et al., "Demonstration of a self-pulsing photonic crystal Fano laser," Nature Photonics 11, 81–84 (2017).
[8]   Y. Yu, et al., "Ultra-coherent Fano laser based on a bound state in the continuum," Nature Photonics, (2021).

# InP based quantum dot laser at 1.3 μm

**V. Joshi,** [*] **S. Bauer, V. Sichkovskyi, and J. P. Reithmaier**

*Technical Physics, Institute of Nanostructure Technologies and Analytics (INA), CINSaT, University of Kassel, Heinrich-Plett-Str. 40, 34132 Kassel, Germany*
*\*joshi@ina.uni-kassel.de*

**Abstract:** An InP based QD laser with InAs quantum dots (QDs) emitting at 1.3 μm wavelength was realized. A high modal gain of 15.23 cm$^{-1}$ per QD layer, low internal absorption value of 11.2 cm$^{-1}$ and high internal quantum efficiency of 0.82 were obtained. BA laser resulted in characteristic temperatures of 74 K and 370 K for $T_0$ and $T_1$, respectively.

## 1. Introduction

The future of photonics chips is known to require the integration of optoelectronic components. Over the past decade many theoretical studies have shown significant improvements in semiconductor device performance by using quasi zero-dimensional systems or QDs [1]. Advantages of using QDs as an active material over other conventional laser systems include, but are not limited to, low threshold current density or temperature insensitive performance [2]. The properties of optically active III-V semiconductor material integrated onto Si electronics might degrade, due to their fundamental material differences. The thus created lattice defects are detrimental to laser performance and reliability and hence QDs have been seen as a solution as they offer a higher tolerance towards temperature and material defects [3]. When considering the silica fiber attenuation spectrum, three different wavelength regimes are usable depending on the desired transmission distance. The long and medium distance transmission bands for data communication are centered at 1.55 μm and 1.3 μm, respectively. The InAs/GaAs material system is widely researched at an emission wavelength of 1.3 μm [1]. However, an emission at 1.55 μm is hard to accomplish. Contrary to GaAs substrates, InP has a smaller lattice mismatch of 3.2 % to InAs, which enables the formation of QDs, which emit at the desired telecommunication wavelength of 1.55 μm. The InAs/InP material system has been widely researched for this purpose and is playing a dominant role in the long wavelength laser application driven by optical fiber communications. In this paper, the InAs/InP material system is researched and deployed for an emission wavelength of 1.3 μm, which broadens the usable spectral window of the InAs/InP material system and allow to utilize the much higher modal gain in InP-based QD lasers in comparison to GaAs based QD lasers.

## 2. Epitaxial structure

All the layers included in the laser growth except for the QD layers are lattice-matched to the InP substrate. The analyzed laser structure was grown on an n-type InP (0 0 1) wafer. The structure consists of a 200 nm thick InP:Si buffer layer, followed by 300 nm of In$_{0.523}$Al$_{0.477}$As:Si and 100 nm of In$_{0.528}$Al$_{0.371}$Ga$_{0.101}$As, whereas the first 20 nm are also Si-doped. The subsequent active region is a stack of 6 InAs QD layers separated by 20 nm of In$_{0.528}$Al$_{0.371}$Ga$_{0.101}$As. This is capped by another 100 nm of In$_{0.528}$Al$_{0.371}$Ga$_{0.101}$As. Similarly, the last 20 nm are p-type doped by Be. These layers are followed by 1.8 μm of InP:Be and a highly doped 200 nm thick In$_{0.532}$Ga$_{0.468}$As:Be layer used for contacting. In order to achieve lasing at 1.3 μm, a special growth technique was implemented based on a sub-monolayer nucleation layer. More details will be shown during the presentation. The laser structure was processed into broad area (BA) lasers of varying length with a stripe width of 100 μm. A short-cavity ridge waveguide (RWG) laser was also fabricated from the same laser structure with a cavity length of approximately 900 μm and a ridge width of about 2 μm.

## 3. Results and discussion

The emission spectra and temperature dependent P-I characteristics of the fabricated BA lasers are plotted in Fig. 1 and Fig. 2, respectively. The emission wavelengths plotted in Fig. 1 were close to the desired wavelength of 1.3 μm and will be compensated by decreasing the InAs QD layer thickness for subsequent growth processes. Furthermore, the 1018 μm long BA laser in Fig 2. showed a general decrease of the slope efficiency from low to higher temperatures. An analysis of the length dependent P-I characteristics resulted in the static parameters presented in Tab. 1. When compared to a similar state-of-the-art QD laser emitting at 1.55 μm [4, 5], the threshold current density at infinite cavity length, as well as the transparency current density, are relatively low. Furthermore, the internal quantum efficiency is very high with 0.82. Typical values of 1.55 μm InP devices are in the range of 0.4 - 0.6 [6, 7]. The internal absorption with about 11.2 cm$^{-1}$ is comparable to the values reported in the literature for InP based lasers [5, 6]. A further reduction might be possible by optimizing the RTA temperature and optical waveguide design. The modal gain of 15.2 cm$^{-1}$ per QD layer is similar to the values reported in the literature as they lie in the range of 12 cm$^{-1}$ to 15 cm$^{-1}$ for similar devices [4-7]. Additionally, a temperature dependent evaluation of the lasing properties of the fabricated BA laser resulted in characteristic temperatures of

74 K and 370 K in the range of 20 °C to 100 °C for $T_0$ and $T_1$, respectively. RWG lasers from the same sample will be processed and the results will be reported at the conference. A temperature dependent analysis of the RWG would provide a better understanding of the device characteristics such as ground state transitions.
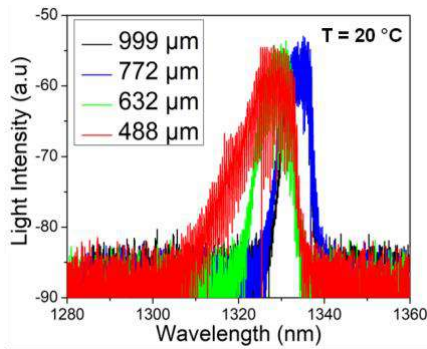


**Figure 1**: Emission spectra of BA lasers with different cavity lengths, measured at 20 °C
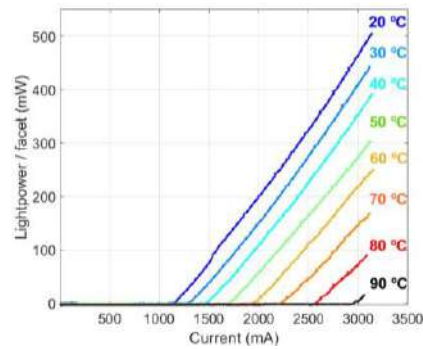


**Figure 2**: P-I characteristics of BA lasers with 1018 µm length show operation up to 90 ℃ in pulsed mode.

**Table 1:** Static parameters evaluated from the P-I characteristics of BA lasers of varying length, measured at 20 °C.

| Evaluated internal parameters | InAs/InP 1.3 µm |
|---|---|
| Threshold current density at infinite cavity length $J_{inf}$ [A/cm$^2$] | 669.6 |
| Internal quantum efficiency $\eta_i$ | 0.82 |
| Internal absorption $\alpha_i$ [1/cm] | 11.3 |
| Transparency current density $J_{tr}$ [A/cm$^2$] | 468.5 |
| Modal gain $\Gamma g_0$ [1/cm] | 91.4 |

## 4. Conclusions

In summary, the presented laser structure shows the realization of an InAs/InP QD laser emitting at approximately 1.3 µm at room temperature. The evaluated static parameters showed a high modal gain as expected for InP based QD lasers, which will allow the realization of short devices. The first evaluation results of the temperature dependent characteristics based on BA laser characteristics show moderately high characteristic temperatures in comparison to 1.55 µm QD lasers [4]. These might be improved by increasing the carrier confinement by structural optimization, by reducing the size distribution during the QD nucleation process and by increasing the recombination efficiency by p-doping of the active layer. In general, due to the reduced average QD size for 1.3 µm lasers in comparison to 1.55 µm lasers and related larger level splitting between the quantized QD states, we expect in future even a significantly improved temperature insensitivity in 1.3 µm QD lasers.

## 5. References

[1] R. Soref, "The past, present, and future of silicon photonics," *IEEE. J. Quantum Elelctron.* vol. 12, no. 6, pp. 1678-1687 (2006).
[2] O.B. Shchekin and D.G. Deppe, "1.3 µm InAs quantum dot laser with $T_0$=161 K from 0 to 80 ℃," *Appl. Phys. Lett.* vol. 80, 3277 (2002).
[3] A.Y. Liu, S. Srinivasan, J. Norman, A. Gossard, and J. Bowers, "Quantum dot lasers for silicon photonics," *Photon. Res.* vol. 3, no. 5, pp. B1-B9 (2015).
[4] A. Abdollahinia, S. Banyoudeh, A. Rippien, F. Schnabel, O. Eyal, I. Cestier, I. Kalifa, E. Mentovich, G. Eisenstein, and J.P. Reithmaier, " Temperature stability of static and dynamic properties of 1.55 µm quantum dot lasers," *Opt. Express* vol. 26, no. 5, pp. 6056-6066 (2018).
[5] S. Banyoudeh, A. Abdollahinia, F. Schnabel, O. Eyal, V. Sichkovskyi, G. Eisenstein, and J.P. Reithmaier, "Temperature-insensitive high-speed directly modulated 1.55 µm quantum dot lasers," *IEEE Phot. Technol. Lett.* vol. 28, no. 21 pp. 2451-2454 (2016).
[6] S. Bhowmick, M. Z. Baten, T. Frost, B. S. Ooi, and P. Bhattacharya, "High Performance InAs/In0.53Ga0.23Al0.24As/InP Quantum Dot 1.55 µm Tunnel Injection Laser," *IEEE J. Quantum Electronics*, vol. 50, no. 1, pp. 7–14 (2014).
[7] K. Akahane, T. Umezawa, A. Matsumoto, N. Yamamoto, and T. Kawanishi, "Characteristics of highly stacked InAs quantum-dot laser grown on vicinal (001)InP substrate," *Jpn. J. Appl. Phys.* 55, 04EJ16 (2016).

# Time-symmetric and symmetry-broken pulse sequences in a spiking micropillar laser with optical delayed feedback

**V. A. Pammi[1], S. Terrien[2], N. G. R. Broderick[2], R. Braive[1], G. Beaudoin[1], I. Sagnes[1], B. Krauskopf[2] , S Barbay[1,*]**

*1 Université Paris-Saclay, CNRS, Centre de Nanosciences et de Nanotechnologies, UMR9001, Palaiseau, France*
*2The Dodd-Walls Centre for Photonic and Quantum Technologies, The University of Auckland, New Zealand*

*\*sylvain.barbay@c2n.upsaclay.fr*

**Abstract:** Spiking micropillar lasers can sustain regenerative temporal dissipative solitons when subjected to delayed optical feedback. While presenting features of an optical buffer in the short term, these systems can converge from a variety of initial conditions to a handful of equidistant and symmetry-broken self-pulsing patterns in the long term; the convergence depends on the laser parameters and feedback parameters. They are thus attractive systems for several applications such as non-harmonic and controllable pulsed sources and analog photonic computing.

## 1 Introduction

Limit-cycle oscillations and pulses in lasers can originate from a variety of physical processes such as self-pulsing, mode-locking and frequency combs. A well known physical system, the laser with saturable absorber can produce self-pulsing regimes. However, these regimes are difficult to stabilize and give rise to a lot of pulse-to-pulse jitter. A convenient way to stabilize self-pulsing in these systems is to introduce a delayed optical feedback. This is done simply by forming an external cavity by adding a distant mirror. When the solitary laser is pumped below the laser threshold, the laser-off state is stable. In a specific regime just below the laser threshold, the so-called excitable regime, a sufficiently strong optical or electrical perturbation can perturb the stable off-state and induce an optical pulse (spike), which has a calibrated amplitude, independent of the strength of the perturbation which caused it. In the presence of an external cavity, this pulse can then be regenerated resulting in a train of calibrated pulses with a timing fixed approximately by the external cavity round-trip time: this is called regenerative self-pulsing [1–3]. Regenerative pulses are temporal dissipative solitons in time-delay systems and share some properties with dissipative solitons found in spatially extended systems [4]. We report here recent experimental and theoretical results on the dynamics of a micropillar semiconductor laser with integrated saturable absorber and delayed optical feedback working in this regime. Despite the apparent simplicity of the system, we show that it can give rise to a wealth of unexpected and intriguing dynamical regimes.
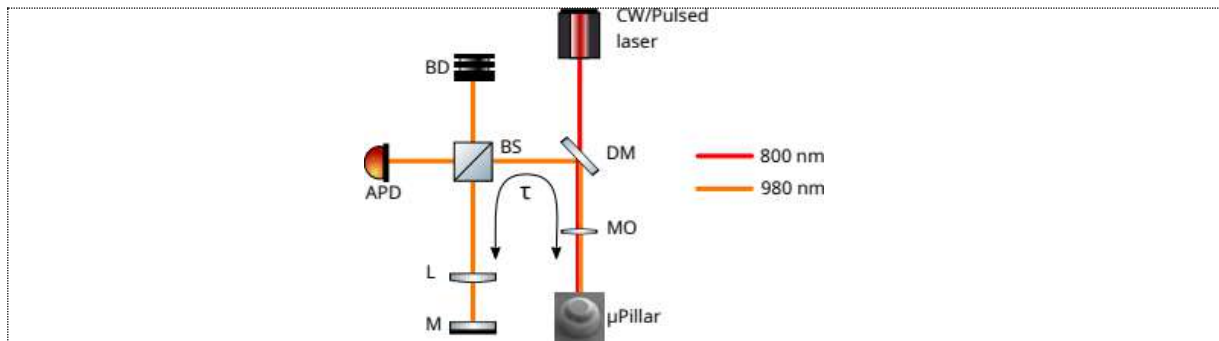
## 2. Experimental setup



**Figure** 1: Schematics of the experimental setup. M: high reflectivity feedback mirror, L: lens f = 5cm, BS: beamsplitter R/T=70/30, DM: dichroic mirror, MO: microscope objective, BD: beam dump, APD: avalanche photodiode. The micropillar laser emits at 980nm, is pumped cw and perturbed by short (80ps) optical perturbations at 800nm.

The experimental setup is depicted in Fig. 1. An excitable micropillar laser (5 µm in diameter), consisting of a microcavity laser with an embedded gain and saturable absorber section [5], is optically pumped using a CW laser at 800 nm . Its emission is centered around 980 nm. The output of the micropillar laser is reinjected after a delay t after after reflection on a distant mirror. The reinjected intensity is less than 50% due to two passes through the beam splitter. The delayed feedback time is of the order of 10 ns. Part of the non-reinjected intensity is detected using a fast avalanche photodetector (5GHz bandwidth) and amplified by a high-bandwidth, low-noise RF amplifier. A mode-locked Ti:Sa laser provides perturbation pulses of 80 ps duration at around 800 nm.

## 3. Results and discussion

We demonstrate that the asymptotic dynamics of this system consists of multistable periodic orbits, with different and coexisting harmonic pulsing regimes [5,6]. While in the short term, long lived transients in the form of almost arbitrary temporal patterns of pulses can be excited, these must necessarily converge towards one of the possible asymptotic attractors. The final state of the system depends on the initial conditions, or can be controlled by a single external control optical pulse.

At last, in the unusual situation where the saturable absorber has a slower recombination time than the gain, we observe a singular physical phenomenon unseen in other systems: irregular pulse-timing sequences can be stable in the cavity. We explain how this follows from a symmetry-breaking of the regular and equidistant (harmonic) pulsing regimes (cf. Fig. 2) [7]. The resulting stable pulse timing sequence can then be controlled by the feedback delay. All the regimes with equidistant and non-equidistant pulse-timings can coexist and can be selected with appropriate initial conditions or controlled by applying well-defined perturbations. Our observations are well supported by theoretical models.
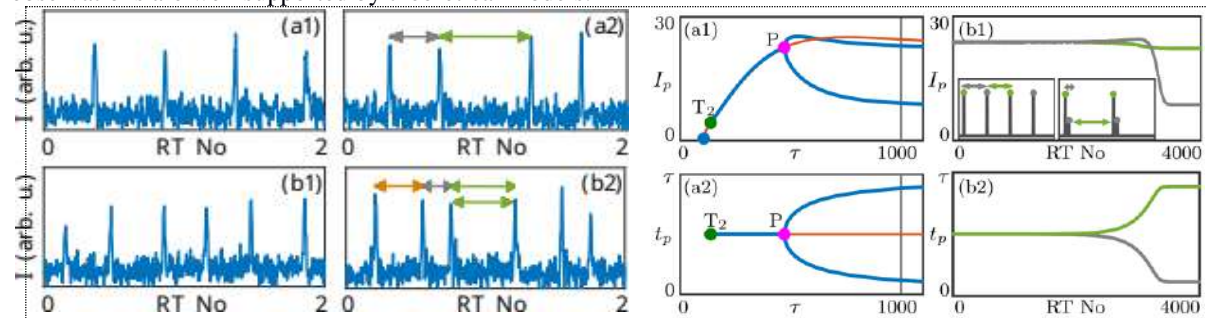


**Figure** 2: Left: Experimental time traces recorded for a delay time of 8ns and for two external cavity round trips. (a1) stable regular two-pulse per round trip regime. (a2) symmetry-broken stable regime with two- pulses per round trip. (b1) transient three-pulse per round trip regime. (b2) symmetry-broken stable regime with three-pulses per round trip. Right: numerical simulations of the system showing the symmetry breaking bifurcation with two pulses per round trip in the (a1) maximum pulse amplitude and (a2) pulse timings within the external cavity. The dynamical evolution towards the bifurcated states starting from a harmonic regime are shown in (b1,b2) versus the number of external cavity round trips RT.

## 4. Conclusion

In conclusion we show the wealth of unusual dynamical regimes occurring in an excitable microlaser with delayed optical feedback. These regimes can find applications in novel types of lasers, or in neuromimetic photonics applications.

## 5. References

[1]     B. Garbin, J. Javaloyes, G. Tissoni, and S. Barland, "Topological solitons as addressable phase bits in a driven laser," *Nat. Commun.* vol. 6, p. 5915 (2015).
[2]     B. Romeira, R. Avó, J. M. L. Figueiredo, S. Barland, and J. Javaloyes, "Regenerative memory in time-delayed neuromorphic photonic resonators," *Sci. Rep.* vol. 6, p. 19510 (2016).
[3]     S. Terrien, B. Krauskopf, N. G. Broderick, R. Braive, G. Beaudoin, I. Sagnes, and S. Barbay, "Pulse train interaction and control in a microcavity laser with delayed optical feedback," *Opt. Lett.* vol. 43, pp. 3013–3016 (2018).
[4]     S. Yanchuk, S. Ruschel, J. Sieber, and M. Wolfrum, "Temporal dissipative solitons in time-delay feedback systems," *Phys. Rev. Lett.* vol. 123, p. 053901 (2019).
[5]     F. Selmi, R. Braive, G. Beaudoin, I. Sagnes, R. Kuszelewicz, and S. Barbay, "Relative refractory period in an excitable semiconductor laser," *Phys. Rev. Lett.* vol. 112, p. 183902 (2014).
[6]     S. Terrien, V. A. Pammi, N. G. R. Broderick, R. Braive, G. Beaudoin, I. Sagnes, B. Krauskopf, and S. Barbay, "Equalization of pulse timings in an excitable microlaser system with delay," *Phys. Rev. Res.* vol. 2, p. 023012 (2020).
[7]     S. Terrien, V. A. Pammi, B. Krauskopf, N. G. R. Broderick, and S. Barbay, "Pulse-timing symmetry breaking in an excitable optical system with delay," *Phys. Rev. E* vol. 103, p. 012201 (2020).

# Ultra-Short Optical Pulse Generation in a Micro OLED

**Daan Lenstra[1], Alexis Fischer[2,3], Amani Ouirimi[2,3], Alex Chamberlain Chime[2,3,4], Nixson Loganathan[2,3], Mahmoud Chakaroun[2,3]**

[1] Institute of Photonics Integration, Eindhoven University of Technology, P.O. Box 513, 5600MB Eindhoven, The Netherlands; dlenstra@tue.nl
[2] Universite Sorbonne Paris Nord, Laboratoire de Physique des Lasers, UMR CNRS 7538, 99 avenue JB Clement, 93430 Villetaneuse-F
[3] Universite Sorbonne Paris Nord, Centrale de Proximite en Nanotechnologies de Paris Nord, 99 avenue JB Clement, 93430 Villetaneuse-F
[4] Universite de Dschang, IUT-FV de Bandjoun, Cameroon

In order to confirm that a future of organic optoelectronics could be "far beyond display and lighting" applications, we present results of a study of μ-OLED devices under nanosecond and sub-nanosecond electrical pulse excitation.

We report preliminary investigations with high-speed μ-OLEDs and demonstrate very promising optical pulse responses as short as 800ps using Alq3, see Figure 1. These sub-ns optical responses give strong indication that a scientific and technological revolution is at hand with ultrafast dynamics in organic optoelectronics. The measurements are for in-house fabricated μ-OLEDs both with cavity and without cavity. Two types of device are considered, namely small molecule OLED (smOLED) and polymer OLED (pOLED), with different sizes from 25μm x100μm and 100μm x 100μm.

With a laser model based on seven rate equations for an electrically pumped OLED [1], we simulate the generation of ultra-short optical pulses. The model applies to a host-guest system and includes Stoke-shifted reabsorption and field-dependent Langevin recombination. For the Alq3 and F8:F8BT systems we compare the results with the above-mentioned measurements. The good agreement between the measurements and simulations is the basis for further study of the prospects for ultra-short dynamics on the ps time scale.

The results strongly indicate that a scientific and technological revolution is emergent with ultra-fast dynamics of organic optoelectronics, exceeding state-of-the-art results for GaN μ-LEDs and OLEDs [2,3].

[1] Ouirimi, A., Chime, A. C., Loganathan, N., Chakaroun, M., Fischer, A. P. A., Lenstra, D. Threshold estimation of an Organic Laser Diode using a rate-equation model validated experimentally with a microcavity OLED submitted to nanosecond electrical pulses. *Organic Electronics* **2021**, https://doi.org/10.1016/j.orgel.2021.106190.
[2] M. S. Islim et al., "Towards 10Gb/s orthogonal frequency division multiplexing based visible light communication using a GaN violet micro-LED," Photon. Res., PRJ, vol. 5, no. 2, pp. A35–A43, Apr. 2017, doi: 10.1364/PRJ.5.000A35.
[3] K. Yoshida et al., "245 MHz bandwidth organic light-emitting diodes used in a gigabit optical wireless data link," Nat Commun, vol. 11, no. 1, Art. no. 1, Mar. 2020, doi: 10.1038/s41467-020-14880-2.
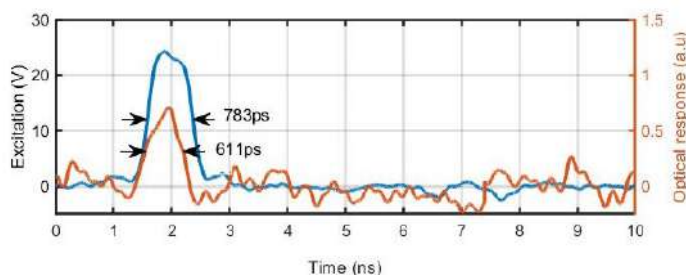
Figure 1. Preliminary measurement showing an 800 ps optical response emitted by an Alq3 based μ-OLED. The blue curve is the excitation voltage (left scale) and the orange curve is the emitted light (arbitrary units).

# Thermal Crosstalk Effects in Monolithically Integrated DBR Lasers.

**Jessica César Cuello,[1]\* Alberto Zarzuelo,[2] Robinson C. Guzmán,[1] Luis G. Guerrero,[1] Guillermo Carpintero[1]**

[1] *Universidad Carlos III de Madrid, Av. de la Universidad 30, 28911 Leganés, Madrid. Spain*
[2] *SENER Aeroespacial, 28760 Tres Cantos, Madrid, Spain*
*\*jecesarc@img.uc3m.es*

**Abstract:** In this work we present the study of the wavelength shift of two Distributed Bragg Reflector (DBR) lasers induced by thermal crosstalk. The system is part of a Photonic Integrated Circuit (PIC) fabricated in a generic foundry approach on a passive/active Indium Phosphide (InP) Multi-Project Wafer (MPW) run by SMART Photonics. Analysis of a deep-etch waveguide as trench for thermal crosstalk reduction was also carried out.

## 1. Introduction

Photonic Integrated Circuits (PIC) are becoming more essentials in today's systems as they are able to reduce weight, volume and power consumption while gaining scalability [1]. From wavelength division multiplexing (WDM) receivers [2] to programmable photonic processors [3] and RF signal generation systems [4], the complexity of the structures integrated in a PIC has been increasing. However, as complexity increases, so does the number of components included in a chip. Due to the standardized chip area sizes of the generic foundry platforms, this results in a reduction of the distance between component, increasing the density. The main drawback of this result is the interaction between components that begins to affect the system performance, usually known as crosstalk, which represents a limitation of the component density that can be doable within a PIC. Several types of crosstalk have been observed and study in a Photonic Integrated Circuit like, optical crosstalk between nearby waveguides [5], radio-frequency (RF) crosstalk [6] and thermal crosstalk [7].

Thermal crosstalk appears when the dissipated heat from an active device, like a Semiconductor Optical Amplifier (SOA), affects the behavior of others components in the same PIC. So, in practice, the simplest solution to decrease thermal crosstalk is to define some limits regarding the minimum space between elements. However, although it helps prevent the appearance of thermal crosstalk, the PIC density resulting from miniaturization is compromised. Different solutions, like the insertion of thermal shunts for heat dissipation [8] and liquid crystals aiming to improve temperature stabilization [9], are used to reduce the unwanted effects of thermal crosstalk.

This paper focuses on the characterization of the wavelength shift produced by thermal crosstalk between active devices, inserting an SOA between two DBR lasers forming an integrated optical heterodyne source. The analysis of a deep-etch waveguide as trench for thermal crosstalk reduction is also presented.

## 2. Model description, experimental setup

The PIC under test is observed in Figure 1. The system consists of an optical heterodyne source, formed by two DBR lasers optically combined by a 2x1 Multi Mode Interference (MMI) coupler, a third DBR laser used as heat source and a deep-etch waveguide as trench between the heat source and the bottom DBR. Each DBR laser is formed by a 100 µm front Bragg grating, a SOA of 370 µm, and a 600 µm rear Bragg reflector. The gratings are designed to establish the laser emission wavelength around 1550 nm. The length of the trench is 1320 µm, and its width and etching deep are around 1.5 µm and 2.15 µm, respectively. The distance between each DBR is approximately 75 µm. The PIC is mounted on an Aluminium Nitride sub-carrier placed on a temperature stabilized copper chuck with the temperature set to 16°C. The light is collected from the output of the 2x1 MMI coupler.



**Figure 1**: Picture of the Photonic Integrated Circuit.

## 3. Results and discussion

The P-I curve of the Top and Bottom DBRs is presented in Figure 2. Although both lasers are identical, differences given by the fabrication process are observed. The measurements were organized as follows.

First, we set the Top DBR current to 80 mA, setting a 1549.907 nm initial wavelength, and then we start to increase the current injected to the heater SOA from 0 mA to 100 mA while keeping the Bottom DBR off. After recording all the results from this first test, the same process was performed again but this time we turn off the Top DBR and set the Bottom DBR current to 80 mA, resulting in a 1549.79 nm initial wavelength. Then we proceed to increase again the heater current.
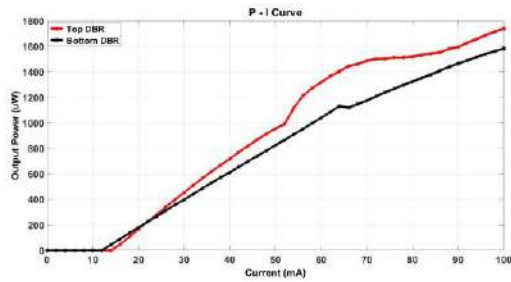


**Figure 2**: P-I curve of Top and Bottom DBR.
**Figure 3**: DBR Wavelength shift vs Heater Current.
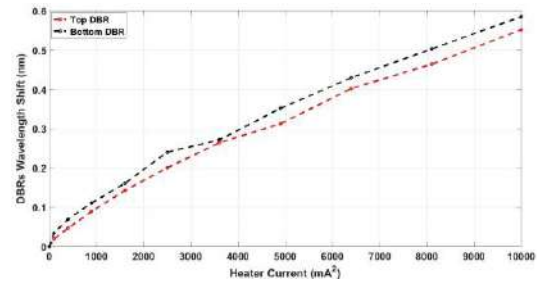
Figure 3 shown the DBR Wavelength Shift vs Heater Current curve for the Top and Bottom DBR. The heater current is expressed quadratically as we are in presence of thermal effects. The shift represented in Figure 3 is with respect to the initial wavelength of the respective DBR. The resulting final wavelength can be expressed as equation (1) and (2).

$$\lambda_{TOP} = \lambda_{Initial} + C_T * I_{Heater}^2 \qquad (1)$$
$$\lambda_{BOT} = \lambda_{Initial} + C_B * I_{Heater}^2 \qquad (2)$$

where $C_T = 5.43\ e^{-5}\ nm/mA^2$ and $C_B = 5.66\ e^{-5}\ nm/mA^2$ are the coefficients resulting from the wavelength increment in Top and Bottom DBR, respectively. As it can be seen from Figure 3, both lasers suffer similar wavelength shift from thermal crosstalk when injecting current to the SOA of the heater.

## 4. Conclusion

With this work we were able to confirm that thermal crosstalk effects are present in components close to the SOA when biased. Also, the deep-etch waveguide inserted as trench between the heater and the Bottom DBR does not help to reduce thermal crosstalk as both lasers, Top and Bottom, experience similar wavelength shift when the heater is ON. However, some others strategies for thermal crosstalk reduction, like the use of metallization as heat sink, can also be studied.

## 5. References

[1] D. Marpaung, J. P. Yao, et al., "Integrated microwave photonics," *Nature Photonics*, vol. 13, pp. 80-90 (2019).

[2] M. R. Amersfoort, C. R. De Boer, et al., "High performance 4-channel PHASAR wavelength demultiplexer integrated with photodetectors," in Proc. *19th Eur. Conf. Opt. Commun.*, vol. 3, pp. 49-52 (1993).

[3] L Zhuang, C. G. H. Roeloffzen, M. Hoekman, K. J. Boller, A. J. Lowery "Programmable photonic signal processor chip for radiofrequency applications" *Optica*, vol. 2, no.10, pp. 854-859 (2015).

[4] G. Carpintero, K. Balakier, et al., "Microwave Photonic Integrated Circuits for Millimeter-Wave Wireless Communications" *Journal of Lightwave Technology*, vol. 32, no. 20, pp. 3495-3501 (2014).

[5] D. Melati, F. Morichetti, G. G. Gentili and A. Melloni, "Optical radiative crosstalk in integrated photonic waveguides", *Opt. Lett.*, vol. 39, no. 13, pp. 3982-3985 (2014).

[6] W. Yao, G. Gilardi, M. Smit and M. J. Wale, "Performance degradation of integrated modulator arrays due to electrical crosstalk", *Advanced Photonics Communications*, (2014).

[7] S. Pandey, H, Neto, et al, "Laser Thermal Crosstalk Modelling in InP based Photonic Integrated Chips", *International Microwave and Optoelectronics Conference*, (2019).

[8] M. N. Sysak, D. Liang, R. Beausoleil, R. Jones, and J. E.Bowers, "Thermal management in hybrid silicon lasers," in *Proc. Opt. Fiber Commun. Conf.*, (2013).

[9] J. Ptasinski, I.-C. Khoo, and Y. Fainman, "Nematic liquid crystals for temperature stabilization of silicon photonics," in *Proc. Photon. Switching*, (2014).

# Abstract

## Session VI: Mid-infrared Quantum Devices

# Mid-Infrared saturable absorbers with ultra-low saturation intensities in the 10-kWcm⁻² range

**M. Jeannin,[1]\* J.-M. Manceau,[1] M. Soubigou,[1] S. Pirotta,[1] M. Malerba,[1] L. Li,[2] A. G. Davies,[2] E. Linfield,[2] G. Biasiol,[3] and R. Colombelli[1]**

*[1]Centre de Nanosciences et de Nanotechnologies (C2N), CNRS UMR 9001, Université Paris-Saclay, 91120 Palaiseau, France*
*[2]School of Electronic and Electrical Engineering, University of Leeds, Woodhouse Lane, Leeds LS2 9JT, United Kingdom*
*[3]Laboratorio TASC, CNR-IOM, Area Science Park, S.S. 14 km 163.5, Basovizza, I-34149 Trieste, Italy*

*\*mathieu.jeannin@universite-paris-saclay.fr*

**Abstract:** We report on an ultra-low threshold saturable absorber operating in the mid-infrared spectral region ($\lambda = 9$ μm). The device relies on intersubband transitions in semiconductor quantum wells, that are embedded in microcavities. It operates in the strong light-matter coupling regime and exploits the collapse of the polaritons upon bleaching of the transition to produce a large absorption change. We have developed an analytical formalism based on coupled mode theory to describe the device non-linear behavior. Using a simple TEC-cooled quantum cascade laser as source, we experimentally demonstrate saturation with a peak pumping power of 750 mW (corresponding to a pump intensity of 20 kW.cm⁻²)

## 1. Introduction

The mid-infrared (MIR) spectral region ($\lambda = 3\text{-}30$ μm) enjoys a rise of interest due to increasingly advanced spectroscopic techniques for metrology, space science, environmental and industrial monitoring, along with the perspective of free space optical telecommunication in the atmospheric transparency windows. The continuing improvement of MIR light sources and detectors might however reach a technological bottleneck. In other spectral regions, efficient optoelectronic devices and signal chains have been realized by using external optical or optoelectronic devices, like modulators or saturable absorbers.

Such devices are missing from the MIR optoelectronic devices toolbox. As a matter of fact, there is no single, well defined technology to create saturable absorbers in the MIR spectral region. In the vis-NIR region, interband transitions in semiconductors exhibit energies and lifetimes that are naturally favorable to reach non-linear behavior with reasonable light intensities, enabling a vast body of applications.[1] On the contrary, semiconductor devices operating in the MIR are mostly based on intersubband (ISB) transitions between quantum-confined electronic states in doped semiconductor quantum wells (QWs). Their extremely short lifetimes impose prohibitively large intensities to be driven out of the linear regime. As a reference, saturation intensities for ISB transitions in bare QWs are around 1 MW/cm² which can only be generated by extremely intense OPO pulses or free electron lasers.

We rely on the strong light-matter coupling to fundamentally alter the saturation properties of ISB transitions embedded in microcavities. In this regime the polaritonic splitting of the two resonances produces well resolved spectral features, that we have for instance successfully used to demonstrate ultra-fast free-space amplitude modulation of MIR beams [2]. In this contribution we show how to leverage the collapse of the light-matter coupling upon absorption saturation to obtain a MIR saturable absorber with a saturation intensity as low as 20 kW.cm⁻² which, remarkably, is attained using a simple quantum cascade laser (QCL).

## 2. Temporal coupled mode theory model

We develop a unified description of the saturation behavior of ISB transitions in cavities based on temporal coupled mode theory (CMT), covering both the weak and strong light matter coupling regimes (WCR and SCR) [3]. In the CMT framework, the ISB transition and the microcavity mode are modelled as oscillators with characteristic parameters ($\omega_{isb}$, $\gamma_{isb}$, $\Gamma_{isb} = 0$) and ($\omega_{cav}$, $\gamma_{nr}$, $\Gamma_r$) representing their natural oscillation frequency, non-radiative and radiative dampings. The coupling between the oscillators is governed by the vacuum Rabi frequency $\Omega_R \propto \sqrt{\Delta n}$ with $\Delta n$ being the population difference between the two subbands of the transition. Upon saturation of the ISB transition, the light-matter coupling vanishes as $\Delta n$ tends towards zero, and the two polaritons collapse on the bare cavity resonance (Fig. 1(a)).

The set of CMT equations and a rate equation approach allow to write analytical asymptotic expressions for the saturation intensity in the WCR and SCR (respectively $I_{sat}^{WC}$ and $I_{sat}^{SC}$) assuming that the ISB transition and the cavity are in resonance ($\omega_{isb} = \omega_{cav} = \omega_0$):

$$I_{sat}^{WC} = \hbar\omega_0 L_{AR} K \times \frac{\gamma_{isb}(\gamma_{nr} + \Gamma_r)^2}{\Gamma_r} \quad (1), \qquad I_{sat}^{SC} = \hbar\omega_{\pm} K' n_s N_{QW} \times \frac{(\gamma_{isb} + \gamma_{nr} + \Gamma_r)^2}{\gamma_{isb}\Gamma_r} \quad (2)$$

where $K, K'$ gather fundamental constants and material parameters (permittivity etc.). $L_{AR}$ is the semiconductor active region thickness, $n_s$ is the introduced doping density, $N_{QW}$ the number of QWs in the active region, and $\omega_\pm$ represent the polariton frequencies.

Interestingly, in the WCR the saturation intensity is still completely independent of the doping and of the number of QWs. In stark contrast, in the SCR $I_{sat}^{SC}$ is proportional to both the number of QWs and the introduced doping. The model further allows to calculate analytical expressions for the reflectivity of the coupled system as a function of frequency or pump intensity, as well as absorption in the sole cavity or ISB mode [3]. We extract design rules to demonstrate a MIR saturable absorber with record-low saturation intensity. Following (1) and (2), the device should possess as few QWs as possible, with a low doping density that is still sufficient to operate at the onset of the SCR to produce a large spectral change upon absorption saturation.

## 3. Experimental results
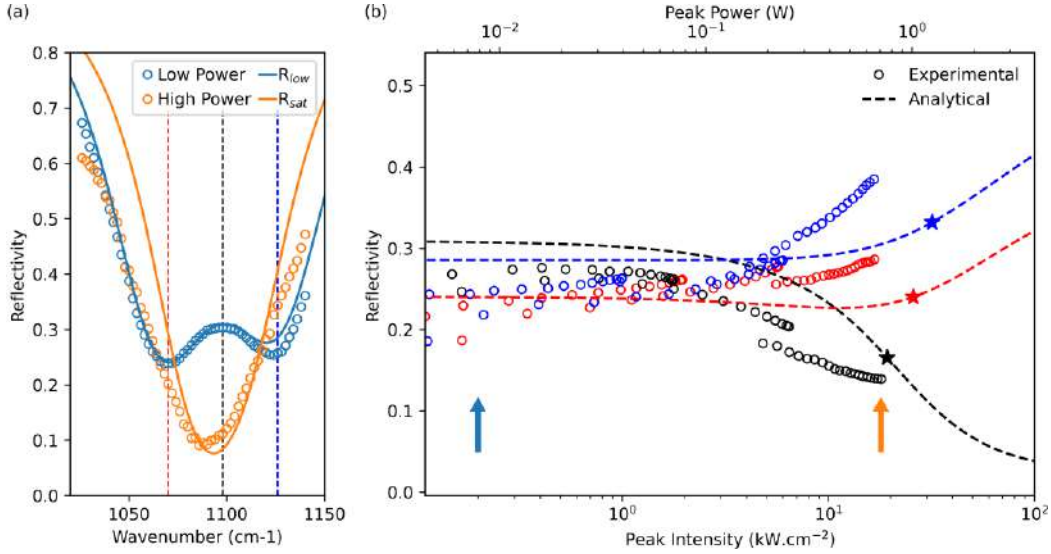


**Figure 1**: (a) Reflectivity spectra of the polaritonic saturable absorber under low (blue) or high (orange) intensity pumping conditions. Corresponding pump intensities are indicated by the arrows in (b). (b) Reflectivity as a function of pump intensity at three different frequencies (resp. 1070 cm$^{-1}$, 1098 cm$^{-1}$ and 1126 cm$^{-1}$ indicated by the dashed lines in (a)). In both panels, open circles represent experimental data, continuous or dashed lines the CMT analytical calculations. Stars indicate the saturation condition, where the ISB absorption is reduced by half its maximum value.

We experimentally test this theory on an eight QWs structure with a doping density $n_s \approx 2 \ 10^{11}$ cm$^{-2}$. The active region is inserted in a metal-metal ribbon microcavity array using standard wafer-bonding and III-V processing techniques. The cavity length is around 4 µm, and the array footprint is 100 x 100 µm². The sample is pumped using an electrically modulated (100ns pulse width – 100kHz repetition rate), commercial tunable external cavity QCL through a ZnSe microscope objective at normal incidence, and the reflected beam is synchronously detected using a HgCdTe detector. The QCL frequency and power are swept to obtain low and high intensity reflectivity spectra (Fig. 1(a)) as well as power-dependent reflectivity curves at the fixed frequencies (Fig. 1(b)) of the lower (resp. upper) polariton (resp. in red and blue) or in the polariton gap (black). A pronounced change in reflectivity occurs around 10 kW.cm$^{-2}$ (~400mW peak power). A CMT analysis of the data reveal that we should reach saturation around a record-low value of 20-30 kW.cm$^{-2}$ (750 mW peak power, stars in Fig. 1(b)). This corresponds to only less than 10mW of average power.

## 4. Conclusion

In conclusion, we demonstrate a very low saturation intensity saturable absorber operating in the MIR and pumped by a simple, commercial QCL. The design is guided by a newly developed analytical theory describing ISB absorption saturation both in the WCR and SCR. These preliminary results on an un-optimized sample open the way towards ultrafast MIR saturable absorbers based on well established, III-V semiconductor platforms.

## 5. References

[1]     U. Keller "Ultrafast solid-state lasers" *Progress in Optics*, 46, 1-115 (2004).
[2]     S. Pirotta *et al.*, "Fast amplitude modulation up to 1.5 GHz of mid-IR free-space beams at room-temperature", *Nature Commun.*, 12, 799 (2021)
[3]     M. Jeannin, JM Manceau, R. Colombelli, "Absorption saturation is tailorable in the strong light-matter coupling regime", arXiv:2012.15633

# Optical injection of mid-infrared extreme events in unilaterally coupled quantum cascade lasers

**Olivier Spitz,**[1] **Andreas Herdt,**[2] **Wolfgang Elsässer,**[2] **Frédéric Grillot**[1,3]
[1]*LTCI Télécom Paris, Institut Polytechnique de Paris, 19 place Marguerite Perey, Palaiseau, 91120, France*
[2]*Technische Universität Darmstadt, Schlossgartenstrasse 7, D-64289 Darmstadt, Germany*
[3]*Center for High Technology Materials, University of New-Mexico, Albuquerque, NM 87106, USA*
[+]*olivier.spitz@telecom-paris.fr*

**Abstract:** This experimental work reports on the unilateral injection of extreme events, those being non-linear phenomena which can be observed in mid-infrared quantum cascade lasers with tilted feedback. Contrary to chaos dynamics leading to synchronization when a master quantum cascade laser is unilaterally injected in a slave quantum cascade laser, the optical injection of these extreme events triggers a peculiar spiking dynamics in the injected slave quantum cascade laser. The slave's dynamics share similarities with the time derivative of the extreme events waveform generated by the master quantum cascade laser.

## 1. Introduction

Quantum cascade lasers (QCLs) are semiconductor lasers relying on intra-band transitions to achieve emission in the mid-infrared and the terahertz domain. Mid-infrared wavelengths around 10 µm are characterized by low atmosphere attenuation [1] and this, in combination with recent progress in room-temperature modulators [2] and detectors [3], has opened the way towards high-speed free-space communication. Another recent experimental efforts showed free-space private transmission based on chaos synchronization in QCLs [4]. This method relies on a master QCL driven chaotic by optical feedback and unilaterally injected into a slave QCL. The peculiarity of chaos synchronization is that the slave QCL reproduces the chaos output of the master QCL if the two lasers are similar. If the output of the master QCL is forced, the synchronization does not occur. For instance, if one biases the master QCL with an electrical sine wave, the master QCL emits a sine wave but the optical output of the slave QCL is not a sine wave. Apart from chaos, QCLs under external optical feedback can generate various types of non-linear dynamics [5, 6] and one can legitimately wonder if these dynamics are also compatible with synchronization. In this work, we experimentally study the injection process of mid-infrared extreme events [5]. Intriguingly, the optical response of the slave QCL can be compared with the time derivative of the master's signal. Thus, the observed phenomenon is not synchronization but accounts for a new non-linear process at mid-infrared wavelength.
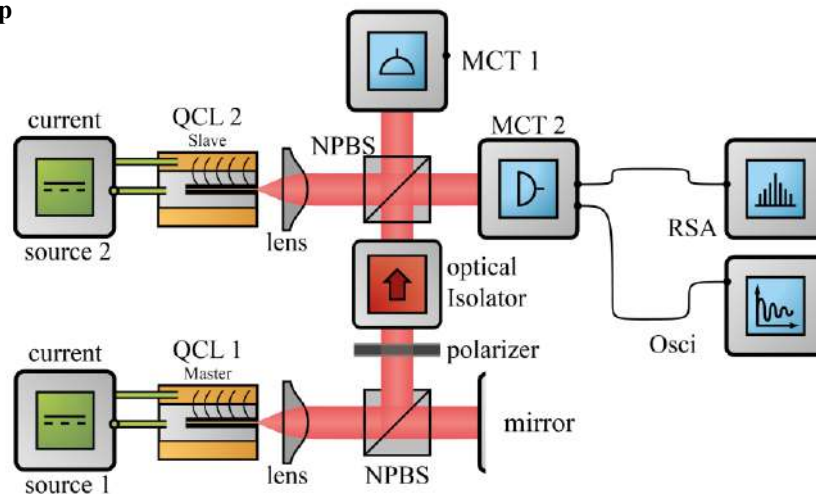
## 2. Experimental setup



Figure 1: Experimental setup for optical injection in unilaterally coupled QCLs. The master laser is in an external-cavity configuration and drives the slave laser that emits the same single wavelength (zero detuning). The analysis of the optical signals is performed with mid-infrared detectors (MCT 1 and MCT 2), a real-time oscilloscope (Osci) and an electrical spectrum analyzer (RSA); NPBS: non-polarizing beam splitter.

The room-temperature master QCL emits single wavelength at 5.7 µm and is placed in an external-cavity configuration. A gold-plated mirror is used to reinject the light back into the master laser's cavity and, in our case, this leads to extreme events in the output of the master QCL because the mirror is tilted [5]. The master light beam is sent towards the room-temperature slave QCL. In order to avoid cross-interaction between the slave QCL and the master QCL, an optical isolator is placed between the two lasers. This corresponds to

unilateral optical injection. The light intensity that is injected into the slave QCL is controlled with polarizer before the optical isolator. The slave QCL is not in an external-cavity configuration, which means that only the injection process can trigger non-linear dynamics in the slave output. Signal from master QCL is retrieved with Mercury-Cadmium-Telluride detector 1 (MCT 1) and the timetrace is recorded with a fast oscilloscope. MCT 2 plays the same role for the slave signal and the oscilloscope allows real-time comparison of the two waveforms.

## 3. Results and discussion

Figure 2 shows the spiking master signal, the slave response signal and the numerical time derivative of the master's signal. For the master's signal (in dark blue), light blue arrows indicate low-amplitude electrical forcing which does not disturb the main spiking dynamics. The electrical amplitude of this forcing is 4 mV and one can compare the magnitude of the non-linear spiking with that of the low-amplitude forcing. The global picture is that the slave laser displays a response every time the master laser triggers a spike. A closer look at the slave's signal shows that the response (in red) is similar to the calculated time derivative (in black) and more specifically when the master's signal has a positive slope. In that specific case, the response of the slave displays a main pulse followed by weaker oscillations which are also found in the numerical calculation. When the master signal shows a decreasing slope, the slave laser outputs a magnified response compared to the numerical calculation but the shape of the response is still consistent. We thus experimentally demonstrated an all-optical differentiator with a unilaterally injected QCL. These findings complement the recent experimental efforts about basic optical neurons in QCLs [5]. The explanation for the slave's behavior is the object of ongoing work but to the best of our knowledge, this differentiator feature has not yet been explored theoretically and experimentally in other semiconductor lasers such as laser diodes and VCSELs. This is worth noting because usually, the dynamics observed in QCLs have previously been thoroughly reported in near-infrared semiconductor lasers.
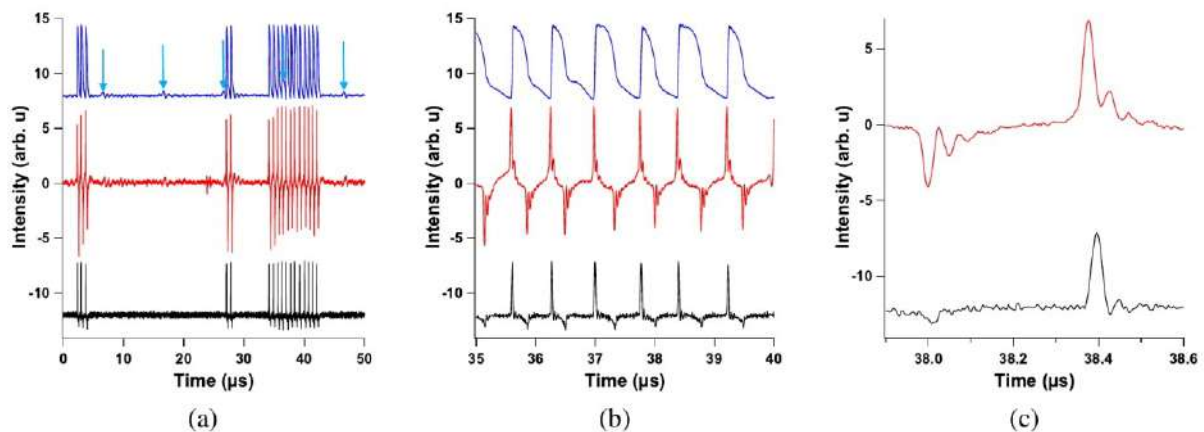


Figure 2: Experimental time traces of the output of the master QCL (blue), the injected slave QCL (red) and the calculated derivative of the master signal (black) when the master laser exhibits spiking dynamics; (a) global picture showing trains of pulses; (b) zoom on the behavior of the slave QCL when the master QCL fires a spike; (c) focus on the similarities between the slave's signal and the calculated derivative of the master's signal, the pulse-down occurs simultaneously in both cases but their amplitude is different while the pulse-up occurs also simultaneously but with a comparable intensity.

## 5. References

[1] El Naboulsi, M., et al., "Fog attenuation prediction for optical and infrared waves," *Optical Engineering* **43**, 319-329 (2004).
[2] Pirotta, S., et al., "Fast amplitude modulation up to 1.5 GHz of mid-IR free-space beams at room-temperature," *Nature Communications* **12**, 1-6 (2021).
[3] Hakl, M., et al., "Ultrafast quantum-well photodetectors operating at 10 μm with a flat frequency response up to 70 GHz at room temperature," *ACS Photonics* **8**, 464-471 (2021).
[4] Spitz, O., et al., "Private communication with quantum cascade laser photonic chaos," *Nature Communications* **12**, 1-8 (2021).
[5] Spitz, O., et al., "Extreme events in quantum cascade lasers," *Advanced Photonics* **2**, 066001 (2020).
[6] Spitz, O., et al., "Stimulating polarization switching dynamics in mid-infrared quantum cascade lasers," *Journal of the Optical Society of America B* **38**, 35 (2021).

## Acknowledgements

# Improving the performance of interband cascade lasers: the influence of intersubband transitions in the valence band

**H. Knötig,[1]\* R. Weih,[2] N. Opacak,[1] J. Koeth,[2] G. Strasser,[1] B. Schwarz[1]**

*[1]Institute of Solid State Electronics and Center for Micro- and Nanostructures, TU Wien, Vienna, Austria*
*[2]nanoplus Nanosystems and Technologies GmbH, Gerbrunn. Germany*
*\*hedwig.knoetig@tuwien.ac.at*

**Abstract:** We present our recent findings on the impact of intersubband transitions in the valence band on the performance of interband cascade lasers (ICLs). We observe a clear dependence of performance indicators, specifically the characteristic temperature $T_0$ and the threshold current density $J_{th}$, on the thickness and composition of the $Ga_{1-x}In_xSb$ hole-quantum well (QW). By meticulously adjusting the design of the active W-QW the intersubband absorption in the valence band can be modified and even effectively avoided, allowing us to enhance ICL performance beyond the sweet spot 3-4 μm region, paving the way towards higher output powers and cw operating temperatures.

## 1. Introduction

Interband cascade lasers (ICLs) [1] are attracting more and more attention as reliable mid-infrared laser sources. Especially their low threshold current densities and low power consumption qualifies them for numerous applications that aim for portable, miniaturized sensing systems. ICLs show a performance sweet spot around 3-4 μm and continuous-wave (cw) operation at room temperature has been demonstrated at wavelengths from 2.8-5.6 μm in the GaSb material system [2,3]. However, difficulties are encountered when trying to extend this range towards longer wavelengths, that can partly be traced back to a still incomplete understanding of the internal device physics.

Here, we report on our latest findings showing the impact of intersubband transitions in the valence band on the performance of ICLs.

## 2. Model description, experimental setup

Using a numerical model employing the eight-band k·p method, we calculate the electronic band structure of the active W-quantum well (QW) in an ICL. This is shown in Figure 1 for an exemplary W-QW. We then use a generalized momentum matrix element model to determine the wavelength-dependent absorption between subbands in the valence band. This model can explain all contributions to the absorption in the W-QW, regardless of the nature of the transition, whether it is interband or intersubband.
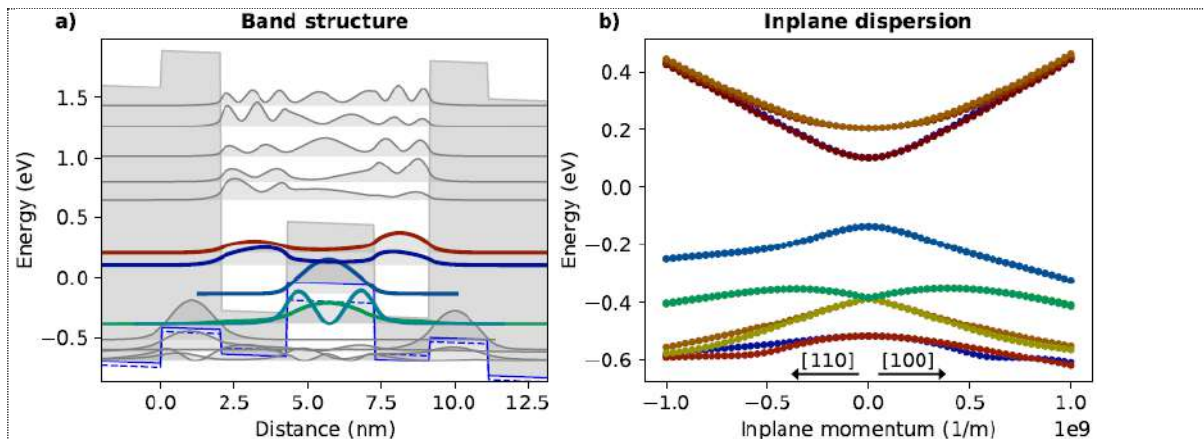


**Figure 1**: a) Calculated band structure at the Γ-point of an exemplary W-QW consisting of AlSb/InAs/Ga₀.₆₅In₀.₃₅Sb/InAs/AlSb layers. b) Inplane dispersion of the calculated bands perpendicular to the growth axis.

### 3. Results and discussion

We experimentally observe a clear dependence of performance indicators, specifically the characteristic temperature $T_0$ and the threshold current density $J_{th}$, on the thickness and composition of the $Ga_{1-x}In_xSb$ hole-QW, which is in good agreement with our model. By meticulously adjusting the design of the active W-QW the intersubband absorption in the valence band can be modified and even effectively avoided, allowing us to enhance ICL performance beyond the sweet spot 3-4 μm region.

### 4. Conclusion

In conclusion, we shed light on a so far almost disregarded effect in ICLs, presenting experimental results connecting the design of the active W-QW with the laser performance. As we see a clear improvement of $J_{th}$ and $T_0$ when changing the width of the h-QW correlating with less intersubband absorption, our results pave the way towards higher cw operating temperatures and output powers for longer wavelengths.

### 5. References

[1]     J.R. Meyer et al., "The Interband Cascade Laser", *Photonics 7*, 75 (2020).
[2]     J. Scheuermann et al., "Single-mode interband cascade lasers emitting below 2.8 μm", *Applied Physics Letters* 106, 161103 (2015).
[3]     W.W. Bewley et al., "Continuous-wave interband cascade lasers operating above room temperature at λ = 4.7-5.6 μm", Optics Express 20, 3235 (2012).

# Efficient double-side detection in the mid-IR, with a QWIP MIM architecture on a transparent substrate

**Mario Malerba[1,\*], Mathieu Jeannin[1], Stefano Pirotta[1], Lianhe Li[2], Alexander Giles Davies[2], Edmund Linfield[2], Adel Bousseksou[1], Jean-Michel Manceau[1] and Raffaele Colombelli[2,+]**

[1] *Centre de Nanosciences et de Nanotechnologies (C2N), CNRS UMR 9001, Université Paris-Saclay, 91120 Palaiseau, France*
[2] *School of Electronic and Electrical Engineering, University of Leeds, Woodhouse Lane, Leeds LS2 9JT, United Kingdom*
**\*** *mario.malerba@c2n.upsaclay.fr*
[+] *raffaele.colombelli@c2n.upsaclay.fr*

**Abstract:** We present a mid-IR ($\lambda \sim 8.3$ μm) quantum well infrared photodetector (QWIP) fabricated on a transparent substrate, allowing photodetection with illumination from either the front surface or through the substrate.

The device is based on a 400 nm-thick GaAs/AlGaAs semiconductor QWIP heterostructure enclosed in a metal-insulator-metal (MIM) optical cavity. For two different excitation configurations - backside illumination through the substrate and frontside direct illumination - we present passive optical characterizations (reflectivity and transmissivity), electric transport measurements and photocurrent generation, showing similar broadband spectral response for the two detector ports and an experimental T_blip of ~200K.

## 1. Introduction

Quantum well infrared photodetectors (QWIPs) are amongst the most suitable detectors for imaging, high speed and/or heterodyne detection in the mid-infrared spectral range (mid-IR, $\lambda = 3 - 30$ µm). The operating mechanism is based on the photo-induced transition of electrons between quantized energy levels of the quantum well conduction bands. When driven by an external bias, electrons promoted in the continuum are transported toward an electrode and detected. Overall the efficiency and detection capability of this mechanism, which is temperature-dependent, can be high, as long as the « dark current » arising from thermal effects is kept low. This is obtained by either cooling down the detector at cryogenic temperatures or by inserting the active region in a metal-insulator-metal (MIM) layout and exploiting the field enhancement and optical confinement capabilities of metallic antennas in optical nanocavities.

To date, this is achieved by enclosing the semiconductor active region between a continuous metallic backplane and the patterned metallic nanostructures, which act at the same time as resonant nanoantennas and as cavity confinement walls, defining the structure. The continuous bottom plane is almost an unnecessary technological requirement, connected to the fabrication procedure of the device, which is waferbonded through thermocompression. A continuous bottom plane presents two main drawbacks: (i) it introduces unwanted parasitic capacitances which limit the operation bandwidth of the detector [1] and (ii) it blocks the optical access from the backside, precluding the possibility of performing more complex optical experiments. Also, patterning the backside enables the integration with chip-level, high-speed multiplexed electronic readout circuits towards compact high resolution, ultrasensitive and ultrafast mid-IR thermal imaging cameras.

In this contribution, we present a mid-IR QWIP based on metallic micro-stripe nanocavity arrays, symmetrically patterned on both sides of the semiconductor active region and fabricated on a mid-IR transparent ZnSe host substrate. We optically characterize the device from a passive point of view, studying the reflection and transmission for light impinging through the two boundaries (air-device, top illumination, and ZnSe-device, bottom illumination through the substrate), and we show that the absorption exhibits the same characteristics and very similar magnitude. We then measure the device spectral photo-response, studying the photocurrent response and current voltage (I-V) characteristics for (i) different cavity resonators with different resonance wavelength and (ii) different temperatures and different impinging directions (front and backside illumination).

## 2. Device Fabrication and experimental setup

The QWIP active region heterostructure is composed of 8 periods of AlGaAs/GaAs quantum wells, designed to operate at around $\lambda = 8.4$ microns. It is placed in a MIM layout, between two patterned metallic nanostripes [2]. The cavity resonances of the system are designed to overlap the QWIP absorption. The principal technological steps involved to implement the device are: (i) EBL patterning and metal evaporation, (ii) transfer of the active region on the ZnSe new host, epoxy bonding and substrate removal, (iii) careful alignment and second patterning / metal evaporation of the active region, (iv) dry etching to obtain optical cavity nano-resonators, confining the electromagnetic field within the semiconductor sidewalls.

Reflectivity and transmission measurements are performed using a mid-IR microscope with a 32x cassegrain objective, coupled to a Fourier Transform Infrared spectrometer (FTIR) Nicolet Nexus 870. Transport measurements (I = f(V), curves collected with a Keitley 2461 source-meter) are carried out in either dark

conditions, with the sample surrounded by a cryo-shield kept at the same temperature as the device, or with an opening from the front *or* the backside, to allow IR radiation of a 300K blackbody to impinge on the detector. Photodetection at last is measured by focusing light from the internal source of a FTIR spectrometer (Bruker Vertex 70v) onto the detector, using a parabolic mirror. A low-noise amplifier (Standford Research Systems SR570) is used to apply an external bias and polarize the detector, and a lock-in amplifier is used to precisely position the characterized nanocavity MIM array in the mid-IR spotsize. Photocurrent spectra are collected in "rapid scan" mode in the region between 650 cm-1 and 6500 cm-1.

## 3. Results and discussion

Reflectivity and transmission measurements show similar characteristics. Absorption spectra, inferred as A=1-R-T, short of a constant connected to multiple reflections in the transparent substrate, show the same characteristics and magnitude dip (see figure, panel (b) for light impinging from the top, air/device boundary, and panel (c) for light impinging from below, ZnSe/device boundary). Different curves in the Figure are for different cavity geometries, spanning stripe widths between L=1.14 microns and L=1.32 microns. Overall, at the cavity resonance, we measure an absorbance of around 45% once corrected for the background. Considering that the maximum absorption value for a thinner-than-$\lambda$ two-port system illuminated from only one side is 50%, the developed detector proves very efficient in energy harvesting [3].

Panel (d) shows photocurrent spectra for three different geometries, on resonance (black line), slightly off resonance (red line) and heavily detuned (green line), both for direct frontside illumination (solid lines) and for backside through-substrate illumination (dotted lines). Panel (e) at last shows, for different device temperatures, the difference between background current (detector illuminated by a 300 K blackbody) and dark current (detector surrounded by a cryo-shield). The data, extrapolated by raw I(V) curves, provide an approximate estimate of the BLIP region, defined as I_bkg/I_dark > 2. We obtain for our detector an experimental $T_{blip}$ of 200K, in both illumination configurations.
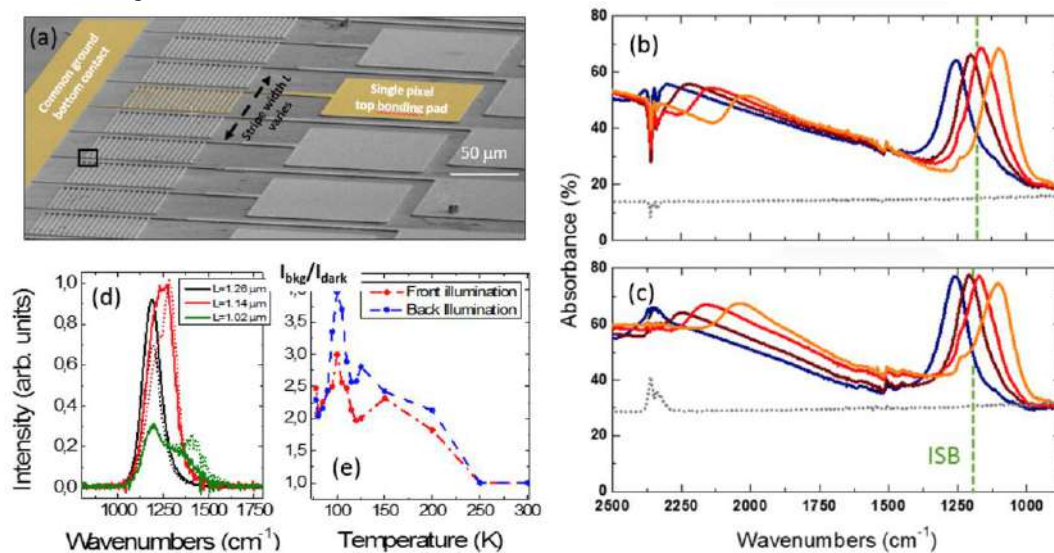


## 4. Conclusions

We demonstrate the operation of a metal-insulator-metal cavity-enhanced QWIP on a mid-IR transparent substrate, that shows very similar performances in both direct and backside illumination. This innovation allows for a vast number of perspective applications that were up to now essentially not available due to the use of Au-Au thermocompression wafer bonding techniques. It is in principle now possible to process the detector in a matrix architecture with flip-chip soldering solutions that permit the use of fast electronic read-out-circuits to develop cavity-enhanced QWIP cameras. Simultaneous two-side illumination is also a desirable feature in experiments involving e.g. heterodyne detection where a precise alignment and overlap between two beams is necessary.

## 5. References

[1] D. Palaferri *et al.*, "Room-temperature nine-µm-wavelength photodetectors and GHz-frequency heterodyne receivers," *Nature*, vol. 556, no. 7699, pp. 85–88, Mar. 2018

[2] N.-L. Tran *et al.*, "III-V on CaF₂: a possible waveguiding platform for mid-IR photonic devices," *Optics Express*, vol. 27, no. 2, p. 1672, Jan. 2019.

[3] S. Zanotto *et al.*, "Perfect energy-feeding into strongly coupled systems and interferometric control of polariton absorption," *Nature Physics*, vol. 10, no. 11, pp. 830–834, Nov. 2014

# InAs-based quantum cascade lasers for spectroscopy of methane

**K. Kinjalk,[1]\* D. Andres Diaz-Thomas[1], Z. Loghmari[2], A. Meguekam[1],**
**M. Bahriz[1], R. Teissier[2], and A.N. Baranov[1]**
*[1]IES, University of Montpellier, CNRS, 34095 Montpellier, France*
*[2]Mirsense, 91120 Palaiseau, France*
*\*kumar.kinjalk@umontpellier.fr*

**Abstract:** We present InAs-based quantum cascade lasers (QCLs) suitable for spectroscopy of methane around 7.6 µm. Distributed feedback (DFB) lasers with a top metal grating were fabricated from a QCL material with a gain centered at 7.7 µm. The grating was formed in the top InAs cladding layer of the structure using E-beam lithography and dry etching. The grating position in the upper cladding and the grating period were varied to find the optimal set of the parameters. DFB QCLs demonstrating single frequency emission between 7.58 and 7.78 µm and operating in the continuous wave regime up to 280K were fabricated.

## 1. Introduction

Molecular spectroscopy is a very important application field of semiconductor lasers. Quantum cascade lasers (QCLs) is the most versatile laser technology offering high performance sources of coherent radiation in the vast spectral range from the mid-infrared to THz frequencies [1]. In recent years, InAs/AlSb QCLs grown on InAs substrates showed a great progress demonstrating pulsed operation close to room temperature (RT) and beyond at wavelengths up to 25 µm [2]. Single frequency distributed feedback (DFB) lasers emitting in continuous wave at RT up to $\lambda = 18$ µm have also been demonstrated [3]. At wavelengths shorter than 12 µm InP-based QCLs are currently mainly employed in spectroscopic applications [4]. In this work we report InAs-based quantum cascade lasers suitable for spectroscopy of methane around 7.6 µm.

## 2. Device fabrication

To fabricate devices for this study we used a QCL material corresponding to the reference wafer EQ746 described in [5]. The structure was grown on a n-InAs substrate in a RIBER 412 solid-source molecular-beam epitaxy (MBE) reactor equipped with As and Sb valved cracker cells. Ridge lasers with Fabry-Perot resonators fabricated from this wafer exhibited threshold current densities about 0.8 kA/cm$^2$ at 300 K and operated in pulsed mode up to 410 K. The QCL emission spectra were centered around 7.7 µm at RT.

DFB lasers were fabricated with a metal-semiconductor grating formed on the top of the laser ridge [3]. The grating defined by E-beam lithography was etched in the upper InAs cladding layer, and was then covered by the top metal contact. The grating period ranged from 1110 to 1160 nm providing emission wavelengths within the absorption spectrum of methane and close to the peak of the QCL gain curve. The main advantage of this technology is the efficient mode selection due the asymmetry of the losses for the two band edge DFB modes and a relatively simple fabrication process. The mode selection is achieved through a proper choice of the grating depth [6]. In this work we used a grating with a duty cycle of about 50% and a fixed depth of 0.55 µm, whereas the thickness of the upper cladding was varied between 1 and 1.4 µm using ICP dry etching. The distance of the grating from the QCL active zone defined the loss of the DFB modes and the coupling coefficient. Such approach ensures better reproducibility compared with the method based on the variation of the grating depth.

## 3. Results and discussion

Finite-element numerical simulations have been performed using the COMSOL software to define the optimal DFB configuration for reliable single frequency operation. The loss and the coupling coefficient for different DFB modes was calculated for different positions of the grating inside the upper cladding layer. In the first series of the devices the upper cladding layer of the structure was etched to a thickness of 1.0 µm and the ridge width was 7 µm. Typical pulsed voltage-current and light-current characteristics of these lasers are shown in Figure 1. Threshold currents were in the range 300-450 mA at RT, corresponding to the threshold current densities 1.2-1.7 kA/ cm$^2$. The maximum output power was low, not exceeding 3 mW. Some devices emitted in the single frequency regime whereas the most of them exhibited two modes located between 7.6 and 7.9 µm. We explain the insufficient mode selectivity in the fabricated DFB lasers by the proximity of the grating to the QCL active region that was probably also responsible for the low optical power of the lasers. The relatively high threshold is partially due to the absorption of the DFB modes in the insulating layer around the narrow laser ridges. This additional absorption also provided a smaller loss contrast for the DFB modes and hence the poorer mode selectivity. Considering these results, the remaining cladding thickness and the ridge width were increased in the

next series of the devices. The grating periods were shifted to smaller values to compensate the increase in the effective refractive index in larger lasers.

The new devices exhibited better performances. The threshold current density of the lasers emitting close to the gain peak of the QCL material was as low as 0.9 kA/cm$^2$ and the optical power exceeded 10 mW (Figure 1).
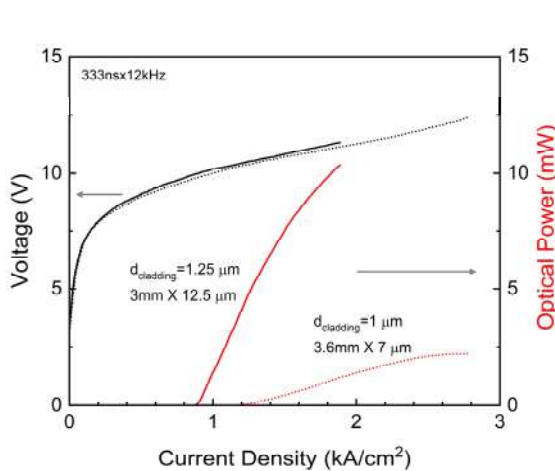


**Figure 1**: Voltage-current and light-current characteristics of DFB QCLs with a grating period of 1140 nm measured in pulsed mode.
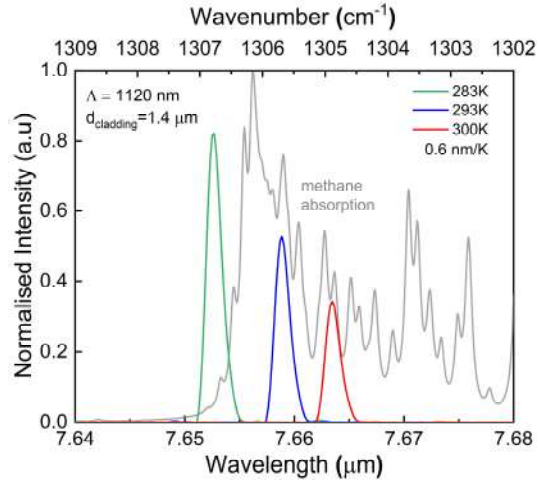
**Figure 2**: Emission spectra of a DFB QCL measured at different temperatures and absorption spectrum of methane.

The single frequency regime was obtained at wavelengths between 7.58 and 7.78 µm for the lasers with grating periods 1010-1040 nm. Figure 2 displays emission spectra of a typical device of this series measured at different temperatures. The emission line exhibited a temperature tuning of 0.6 nm/K corresponding to the temperature shift of the refractive index. To favour continuous wave operation some lasers were mounted epi-side down on copper heatsinks. The best devices operated in the continuous wave regime up to 280K.

## 4. Conclusion

We report InAs-based DFB QCLs with a top metal-semiconductor grating suitable for spectroscopy of methane. The lasers emit in the single frequency regime around 7.6 µm at RT and operate in the continuous wave regime at temperatures accessible with a Peltier cooler.

## 5. References

[1]  J.Faist *et al*., "Quantum cascade laser", *Science,* vol. 264, pp. 553-556 (1994).
[2]  Z. Loghmari, M. Bahriz, A. Meguekam, R. Teissier and A. N. Baranov, "InAs-based quantum cascade lasers emitting close to 25 µm," *Electron. Lett.*, vol. 53, no. 3, pp. 144-146 (2019).
[3]  Nguyen Van Hoang, Z. Loghmari, H. Philip, M. Bahriz, A. N. Baranov, and R. Teissier, "Long Wavelength (λ > 17 µm) Distributed Feedback Quantum Cascade Lasers Operating in a Continuous Wave at Room Temperature", *Photonics*, vol.6, no. 1, p. 31 (2019).
[4]  https://alpeslasers.ch/lasers-on-stock/lasersSTANcw-rt.html.
[5]  Z. Loghmari, J.B. Rodriguez, A.N. Baranov*, M. Rio-Calvo, L. Cerutti, A. Meguekam, M. Bahriz, R. Teissier, E. Tournié "InAs-based quantum cascade lasers grown on on-axis (001) silicon substrate", *APL Photonics,* vol. 5, 041302 (2020).
[6]  M. Carras, M. Garcia, X. Marcadet, O. Parillaud, A. De Rossi and S. Bansropun, "Top grating index-coupled distributed feedback quantum cascade lasers", *Appl. Phys. Lett.,* vol.93, no.1, 011109 (2008). *Photonics*, vol.6, no. 1, p. 31 (2019).

# Spatial Guidance

## To Join Spatial:

1. Open the link https://spatial.chat/s/eslw2021 in your browser.

2. When prompted, type in your full name and a short bio. Although the bio is optional. It is a good place to include information such as what institution or company you are from, or what your area of research is.

3. Click "Continue" to enter the space.

4. You will be prompted to turn on your camera and microphone. Do this by clicking the red camera and microphone icons. These should turn green.

*Having difficulty connecting your audio and/or microphone*? If you are not able to connect to video or audio, you might need to change the camera or microphone input by using the dropdown menus. Ensure that you have enabled your browser to access your camera and microphone in your security settings. In chrome, this is located by clicking on the padlock icon in the address bar.

5. Once you have connected your audio and microphone, click "Join Space" to enter Spatial.

6. In Spatial:

- Navigate by clicking and dragging your icon around,
- Zoom with your mouse scroll wheel, or using your laptop trackpad (alternatively you can also use the zoom options in the bottom right),
- Change rooms by clicking on the room name on the right,
- Turn off your microphone or camera by clicking on the options at the bottom,
- Access help with the help button in the top right,
- Leave the space with the "leave space" button in the top right.

These instructions are also available as a video:

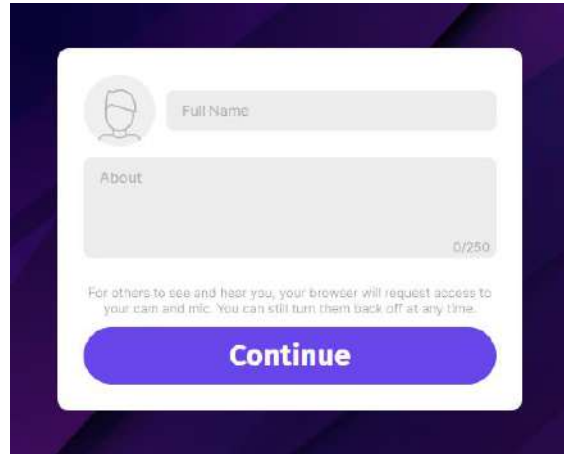https://help.spatial.chat/hc/en-us/articles/360019120259

If you are still having difficulties after following these instructions, email the events team: eslw2021@telecom-paris.fr
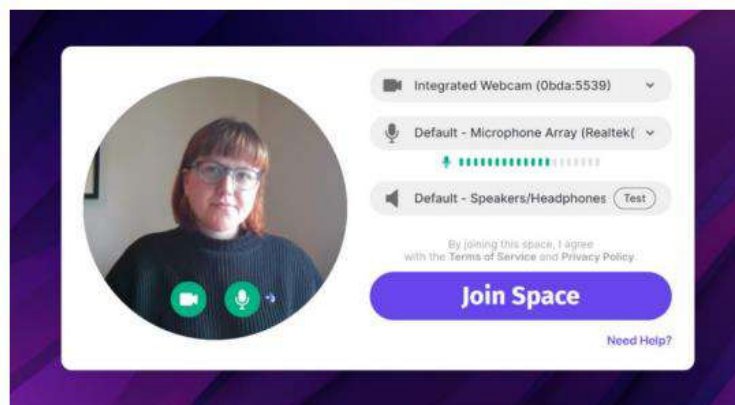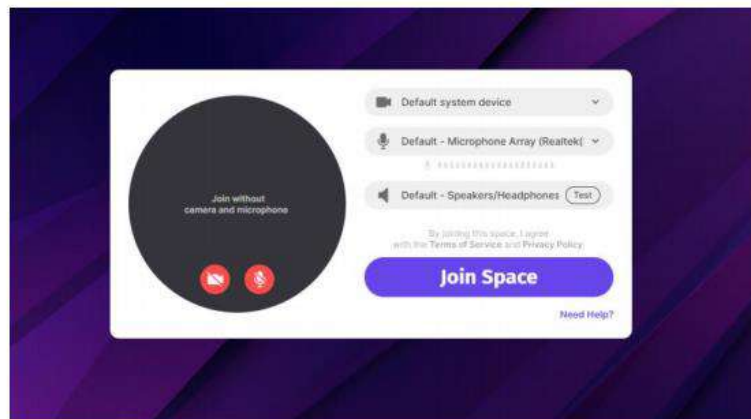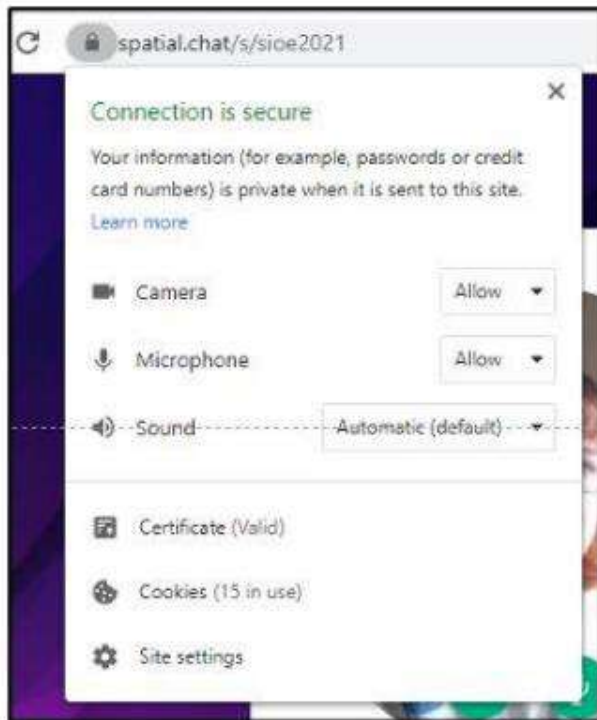
# Spatial Guidance (with images)

## To Join Spatial:

1.  Open the link https://spatial.chat/s/eslw2021 in your browser.
2. When prompted, type in your name and a short bio.



3. Click "Continue" to enter the space
4. You will be prompted to turn on your camera and microphone. Do this by clicking the red camera and microphone icons. These should turn green.

*Having difficulty connecting your audio and/or microphone?* If you are not able to connect to video or audio, you might need to change the camera or microphone input by using the drop-down menu. Ensure that you have enabled your browser to access your camera and microphone in your security settings. In Firefox and chrome, this is located by clicking on the padlock icon in the address bar.

5. Once you have connected your audio and microphone, click "Join Space" to enter Spatial.

6. In Spatial:

**Navigate** by clicking and dragging your icon around,

**Zoom** with your mouse scroll wheel,

**Change rooms** by clicking on the room name on the right,

Turn off your **microphone** or **camera** by clicking on the options at the bottom,

Access **help** with the help button in the top right,

**Leave** the space with the "leave space" button in the top right.

These instructions are also available as a video, watch here